NOVEL AUTOMOTIVE ANTENNA DESIGNS UTILIZING CHARACTERISTIC MODE ANALYSIS

by

EHAB MAHMOUD ABDUL-RAHMAN

A thesis submitted in partial fulfillment of the
requirements for the degree of

DOCTOR OF PHILOSOPHY IN ELECTRICAL AND COMPUTER ENGINEERING

2023

Oakland University
Rochester, Michigan

Doctoral Advisory Committee:

Daniel N. Aloi, Ph.D, Chair
Jia Li, Ph.D.
Sayed Nassar, Ph.D.
Darrell Schmidt, Ph.D.

© Copyright by Ehab Abdul-Rahman, 2023
All rights reserved

To my lovely family

ACKNOWLEDGMENTS

I want to express my deepest appreciation to my committee chair, Professor *Daniel Aloi*, for his invaluable support and guidance. Without his counsel, this work would not have been possible. I would also like to express my gratitude to Professor *Jia Li*, Professor *Darrell Schmidt*, and Professor *Sayed Nassar* for generously dedicating their time to serve on my doctoral advisory committee and providing the necessary support in reviewing my work and providing valuable insights.

I wish to extend my heartfelt appreciation to my family for their continued love and support. This includes my parents, *Mahmoud and Hyam*, and my siblings. I want to offer a special acknowledgment to my wife *Raja'*, who stood by my side, shouldering additional responsibilities while I was occupied. Lastly, I want to express my gratitude to my children, *Wisam, Masa, Bassel, and Sara*, for bringing sweetness and purpose to my life and endeavors.

Ehab Mahmoud Abdul-Rahman

PREFACE

In recent years, there has been a growing emphasis on improving wireless service applications by focusing on antenna technology and antenna systems, which encompasses various aspects, such as broader band antennas, Multiple Input and Multiple Output (MIMO) technologies, antenna arrays, and beam steering techniques to utilize the resources available best. The radiation pattern is the most important parameter for the antennas, as the more the radiation pattern is concentrated in the direction of the communication channel, the better the gain and power budget to the channel, which can be used to improve the capacity and throughput.

In the automotive industry, where vehicles maintain a consistent orientation with respect to terrestrial, satellite, and infrastructure communication sources, achieving a specific radiation pattern is crucial for achieving optimal wireless performance. Recent advancements in automotive antenna systems have introduced some design challenges. These challenges include offering a broad frequency range in cellular function and accommodating multiple antennas within a compact package while maintaining good performance across the entire frequency band.

The techniques of Characteristic Mode Analysis offer an exciting and simplified view of the antenna operation; therefore, it was interesting to me to seek to solve challenges for automotive associated with wide bandwidth for 5G sub-6 GHz and the coexistence with GNSS function using the CMA tools.

Ehab Mahmoud Abdul-Rahman

ABSTRACT

NOVEL AUTOMOTIVE ANTENNA DESIGNS UTILIZING CHARACTERISTIC MODE ANALYSIS

by

Ehab Mahmoud AbdulRahman

Adviser: Daniel N. Aloi, Ph.D.

The Theory of Characteristic Modes (TCM) provides a valuable method for antenna analysis. It helps decompose the total radiation into a set of orthogonal radiation modes. Each mode exhibits a unique reaction in terms of its current distribution and radiation pattern. TCM has proven helpful in numerous antenna design applications, such as enhancing radiation patterns, decoupling antennas, increasing bandwidth, and achieving input impedance match.

This study aims to apply characteristic mode analysis (CMA) to address automotive antenna design challenges. The work involves synthesizing and controlling the desired radiation characteristic mode (CM) at the intended frequency range to achieve an excellent radiation pattern for automotive applications. The study focuses on practical antenna design for the newly defined 5G-sub 6GHz cellular bands in the 0.617-5 GHz range and its cooperation with other coexisting wireless antennas for other wireless functions.

The first application in this research is utilizing the CMA for resolving the radiation pattern defects for a wide-band monopole 5G cellular antenna design. The new wide frequency range of 0.617 - 5 GHz introduces design challenges in maintaining acceptable performance and consistency in the radiation pattern across the band, mainly

due to excited higher-order radiation modes, which affect the elevation pattern, or asymmetrical designs, which affect the azimuth pattern. The study proposes a characteristic mode approach to combine two planer monopole structures, each covering a portion of the frequency range with a first-order mode as a desired radiation pattern mode and avoiding higher-order characteristic modes (CM) from the operational frequency bands to provide optimal and consistent performance.

The second application of the study is utilizing TCM to combine basic antenna geometry in a single antenna structure that simultaneously satisfies the antenna requirement for 5G cellular and global navigation satellite systems (GNSS), where the antenna has a linearly polarized omnidirectional radiation for the newly defined 5G sub-6 GHz cellular bands in the 617 - 5000 MHz frequency range, and a right-hand circular polarization (RHCP) with hemispherical radiation pattern at the GNSS L1 frequency range 1559-1606 MHz. This multi-function antenna would provide a simplified product design and better space utilization, particularly suitable for flat antenna modules for automotive.

The CMA approach and parameters were the key to tuning the antenna structure for best radiation performance. Next, the reflection coefficient was improved with the matching circuit. The proposed designs were simulated, a prototype was measured in an antenna anechoic chamber, and the performance was evaluated on a 1-meter ground plane. Results and radiation patterns were ideal for automotive applications.

TABLE OF CONTENTS

TABLE OF CONTENTS—Continued

TABLE OF CONTENTS—Continued

LIST OF TABLES

LIST OF FIGURES

LIST OF ABBREVIATIONS

5G	Fifth Generation
AM	Amplitude Modulation
AUT	Antenna Ander test
BT	Bluetooth
CM	Characteristic Mode
CMA	Characteristic Mode Analysis
CST	Computer Simulation Technology
DAB	Digital Audio Broadcast
DCS	Digital Communication System
DSRC	Dedicated Short-Range Communication [Explanation]
EM	Electromagnetic
fc	Center Frequency
BW	Bandwidth
FM	Frequency Modulation
FR4	Flame Retardant 4
GHz	Giga Hertz
GNSS	Global Navigation Satellite System
GND	Ground Plane
GSM	Global System for Mobile Communication
H_pol	Horizontal Polarization
IoT	Internet of Things

LAG	Linear Average Gain
LTE	Long-Term Evolution
LHCP	Left Hand Circular Polarization
MIMO	Multiple Input Multiple Output
OTA	Over the Air
OEM	Original Equipment Manufacturer
PCB	Printed Circuit Board
PCS	Personal Communications Services[Explanation]
PIFA	Planar Inverted-F Antenna
RHCP	Right Hand Circular Polarization
RKE	Remote Keyless Entry
RF	Radio Frequency
RWG	Rao-Wilton-Glisson
SADRS	Satellite Digital Audio Receiver System
STD	Standard Deviation
SUV	Sport Utility Vehicle
TCM	Theory of characteristic mode
VBS	Vehicle broadcast services
V2X	Vehicle-to-Everything
VSWR	Voltage Standing Wave Ratio
UWB	Ultra Wideband
XPR	Cross Polarization Ratio

CHAPTER ONE

INTRODUCTION TO ANTENNA DESIGN

The increasing demand for wireless services has led to higher antenna requirements and design complexity, thereby highlighting the necessity for improved design and optimization methods to meet these requirements. The primary performance metrics for antennas typically include higher gain, greater efficiency, broader bandwidth, and antenna decoupling to prevent interference when coexisting in the same package. In addition, some desirable mechanical features for antennas include smaller size, lightweight, compact structure, low profile, and robustness or flexibility. While these characteristics can be beneficial, they can also result in a more complex antenna geometry, which presents additional challenges in the antenna design process.

1.1 Antenna Parameter and design methods

1.1.1 Modern antenna design methods

Designing an antenna commences with a specified collection of system performance requirements, which varies according to the wireless communication application. These requirements include the frequency range of operation bandwidth, minimum VSWR or Return loss necessary to align with the system impedance, and the polarization of the antenna electric field, which must match between transmitter and receiver for optimal performance. Finally, and most important, is the definition of the radiation pattern and antenna gain, which depends on the communication system channel, as shown in Figure 1.1. For example, a high-gain directional antenna is necessary for point-to-point communication, while a wider beam antenna can allow for multiple-point communication. In addition, an omnidirectional radiation pattern is required when communicating in the horizon zone, like in an automobile. On the other hand, randomly mounted applications such as cellular and handheld devices typically limit maximum gain while maintaining adequate efficacy.

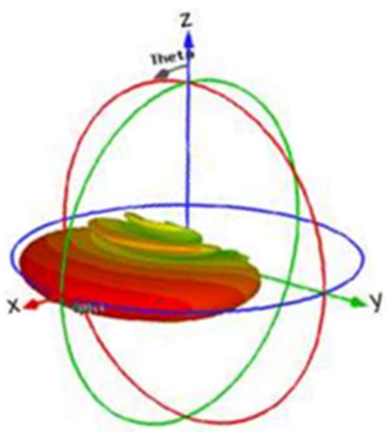

(a) Point to multipoint communication

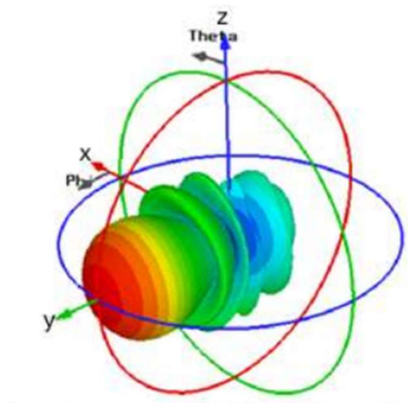

(b) Point-to-point communication

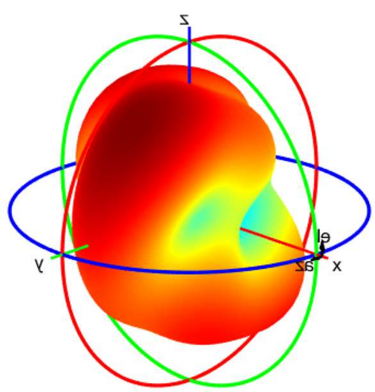

(c) Hand-held devices

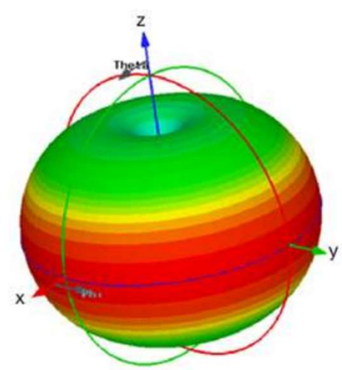

(d) Omnidirectional radiation pattern

Figure. 1.1: Antenna radiation pattern for different applications

The design of modern antennas heavily relies on numerical codes developed in-house or commercial electromagnetic simulators to assess antenna performance prior to the physical fabrication of a prototype. The use of simulation tools significantly helps antenna designers in their work. Nevertheless, the ultimate success of a design often depends on empirical methods and optimization trials. This process calls upon the designer's intuition and previous experience. Therefore, in contemporary times, the designer's expertise plays a vital role in the outcome of antenna design.

On the other hand, some electromagnetic solvers have been paired with optimization algorithms, such as genetic algorithms, bees algorithms, and Firefly, which aim to minimize workload but often result in complex and difficult-to-understand structures. as well as search-based algorithms for optimization that use random trial-and-error to achieve a desired outcome. Additionally, researchers are exploring using artificial intelligence and neural networks as a new method to generate useful and new antenna structures [1].

The characteristic mode theory forms the basis of modal analysis, which utilizes an understanding of radiation mechanisms to offer a more systematic approach to antenna design. Applying CMA in the design can improve the antenna development cycle, help resolve many challenges associated with antenna design, and create optimized antenna structures.

1.1.2 General Antenna Parameters

An antenna is defined as a device that radiates and receives electromagnetic waves. From a functionality point of view, it can be described as a transitional structure between free space and a guiding device. The guiding device could be a transmission, coaxial, or hollow pipe (waveguide) [2]. In the radiation mode, electromagnetic energy is carried over a transmission line in the form of voltage and current that flows over the antenna structure to allow the energy to propagate in free space effectively.

Different antennas with different performance parameters are available to cover the requirements of various wireless applications. Below list is the of the most critical properties to describe an Antenna :

- **Input Impedance:** is the impedance presented at the antenna terminals [3], which should be a conjugate match with the system output impedance to achieve maximum energy transfer between the RF system and the antenna. The voltage standing wave ratio (VSWR) or return loss (RL) is used to identify the matching efficiency at a specific frequency range.
- **Frequency Bandwidth:** is the range of frequencies where the performance of the antenna with respect to some characteristic (such as input impedance, pattern, beam width, polarization, side lobe level, gain, beam direction, and radiation efficiency), according to a specified standard [3].
- **Radiation Pattern:** is a display of the radiation properties of the antenna as a function of the spherical coordinates (θ, φ). The radiation pattern is usually determined in the far field region for a constant radial distance and frequency. [3], The typical radiation patterns are:
    - Omni Directional: no-directional pattern in a given plane and a directional pattern in the other orthogonal plane.
    - Directional Radiator: an antenna that has the property of radiating or receiving more effectively in some directions rather than others.

- **Antenna efficiency** is the ratio between the total radiated powers to the power at the antenna input terminal. It takes into consideration all the power losses before radiation. The losses may be due to mismatch at the input terminals, conduction losses, dielectric losses, and environmental losses.
- **Polarization:** is the electric field vector property that defines the variation in direction and magnitude with respect to time. The electric field is a linearly polarized antenna if it does not change direction over time and propagation distance. If the electric field direction changes in spiral form (circular or elliptical), the antenna is either circularly polarized or elliptically polarized. The sense of rotation for circular and elliptic polarization could be either Left Hand or Right Hand. In order to receive incoming waves efficiently by the antenna, the antenna should match the wave polarization and sense of rotation.

1.2 Automotive Antenna

1.2.1 Automotive Antenna Systems

The concept of a connected vehicle, where vehicles communicate directly with infrastructure or through a wireless cellular network, is becoming necessary [4]. The connectivity to a wide area network (WAN) enabling internet access allows extra functional services for end users, such as software over-the-air (OTA) upgrades, supports geographical services, exchanging traffic information, and other entertainment services such as audio and video streaming. High data rate and low latency communication channels became available with long-term cellular evolution (LTE) technologies and enhancements of 5G wireless networks mainly due to higher and broader frequency spectrum classified into the sub-6GHz band and mm-Wave band [5]. Automotive original equipment manufacturers (OEMs) mainly implement the 5G bands in three frequency ranges: 617- 960 MHz, 1.710 -2.7 GHz, and 3.3 - 5.0 GHz, usually referred to as low band, high band, and Ultra high band.

The Global Positioning System (GPS) has become necessary for automobiles, providing essential support for navigation and finding the most optimal routes. Moreover, it enables remote vehicle tracking, and with the advent of autonomous driving, the accuracy of GPS positioning is increasingly critical for ensuring safety. Therefore, multiple global positioning systems are used to increase accuracy and provide backup functionality. The primary frequency bands used for this purpose are L1, and the systems operating within this range include Beidou (1559.04–1563.16 MHz), GPS and Gallilio (1574.42–1576.42 MHz), and Glonass (1597–1606 MHz). In addition, precise versions operate in the L2 and L5 bands, with frequency ranges of 1215-1254 MHz and 1164-1214 MHz, respectively. Furthermore, the coexistence of GNSS and cellular services allows vehicle tracking in fleet management and helps provide safety and security services.

Vehicle wireless technology V2X (Vehicle to Everything) enables communication between vehicles and their surroundings, including other vehicles, pedestrians, infrastructure, and the cloud. The second generation of V2X technology, V2X-2, includes two primary technologies: C-V2X and DSRC. Both operate in the same frequency range of 5.85-5.925 GHz. However, C-v2x is used in cellular networks with a special protocol (PC5), while DSRC stands for dedicated short-range communication and its mature technology. It enables low-latency communication, which is critical for safety-critical applications like collision avoidance.

Vehicle broadcast services (VBS) include short wave broadcast AM, FM, DAB, and satellite radio services, such as SiriusXM, that provide a variety of entertainment and news content to vehicles equipped with compatible receivers.

Other OEM-specific wireless services include wireless sensor networking, Bluetooth communication, Wi-Fi, ultra-wideband UWB, and remote keyless entry (RKE).

All automotive antennas must achieve particular electrical performance and maintain a long life duration over different conditions. Therefore, Antennas must undergo numerous tests, including vibration testing, thermal shock, high-temperature exposure, thermal cycling, and stress validations to ensure the antennas' stability and durability over the vehicle's lifespan.

1.2.2 Automotive Antenna Location

The large metallic structure of vehicles leaves limited choices for possible Antenna locations. At the same time, a body-hidden antenna may be preferred for aesthetic reasons. Its performance is often compromised due to additional losses from materials and metal blockage. The best location for an antenna in terms of gain and directionality is typically on the roof, as it has no blockage and a relatively large ground plane. Rooftop antennas are often requested to be in a shark fin style or contemporary flat antenna model, which combines various antenna technologies and services into one package, such as 4/2×Cell MIMO, GNSS, SXM, and v2x.

Car manufacturers often utilize other vehicle exterior parts, such as the windshield, rear screen, and windows, to package the antennas. These areas are preferred as they are non-conductive and do not obstruct radiation. Additionally, they provide a broad surface area to implement short-wave antennas, which is an attractive hidden antenna solution at a low cost. More recently, higher frequency antennas such as Cellular and v2x have also been included in these areas.

Spoilers, side mirrors, fenders, and bumpers are additional external body parts that have recently been used to package the antennas. These parts are made of plastic, which makes them suitable for antenna operation. However, they may have radiation pattern nulls, which can be solved by using multiple antennas and a MIMO technologies.

In below figure 1.2 shows multiple antenna locations on the car and possible wireless services based on packaging possibility while maintaining good performance.

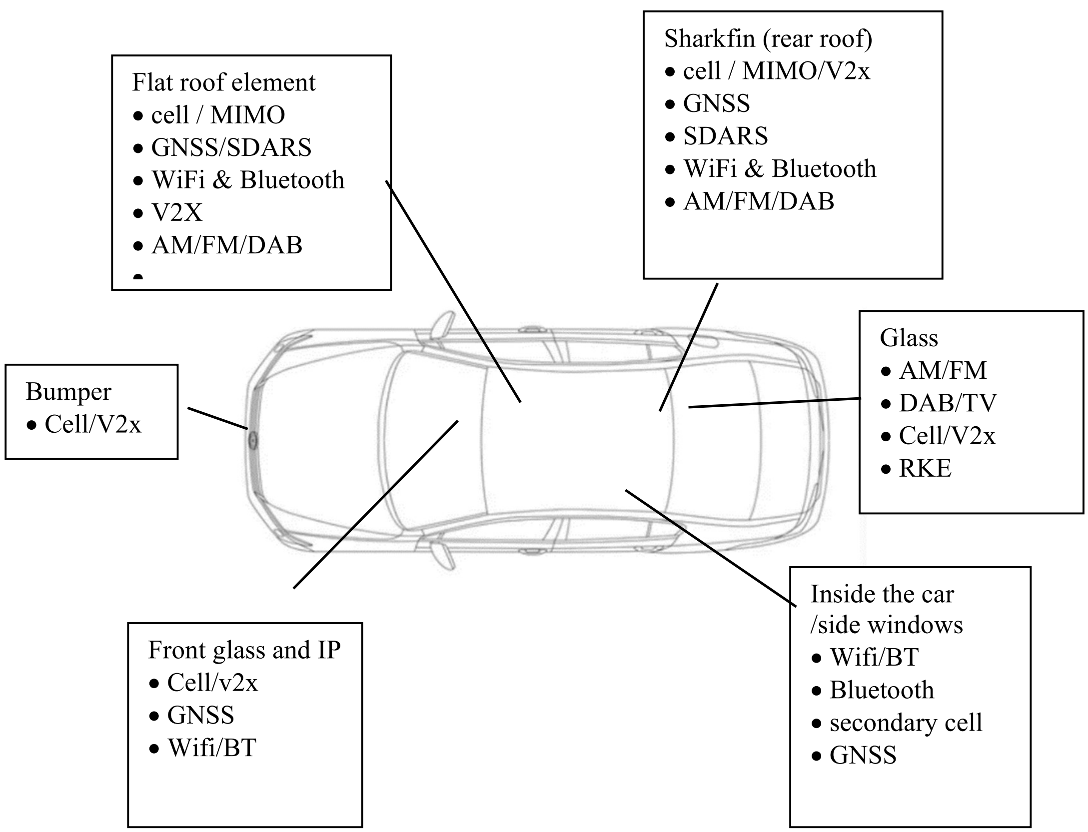

Figure 1.2: Vehicle Antenna packaging per technologiy

1.2.3 Automotive Antenna Radiation Pattern Requirement

Vehicle terrestrial communication requires an antenna with linear polarization and an omnidirectional radiation pattern for cellular communication. The gain must be maximized close to the horizon at theta angles ranging from 60 to 90 degrees to maintain a good communication range when the vehicle is farther away from the cell towers, as shown in Figure 1.3

For Satellite communication, like for GNSS and satellite broadcast services, optimal performance requires circular polarization with a hemispherical radiation pattern with a boresight toward the zenith to allow receiving satellite signals, as shown in the radiation pattern in Figure 1.3. The GNSS requires right-hand circular polarization (RHCP), while SiriusXM is Left-hand circular polarization (LHCP).

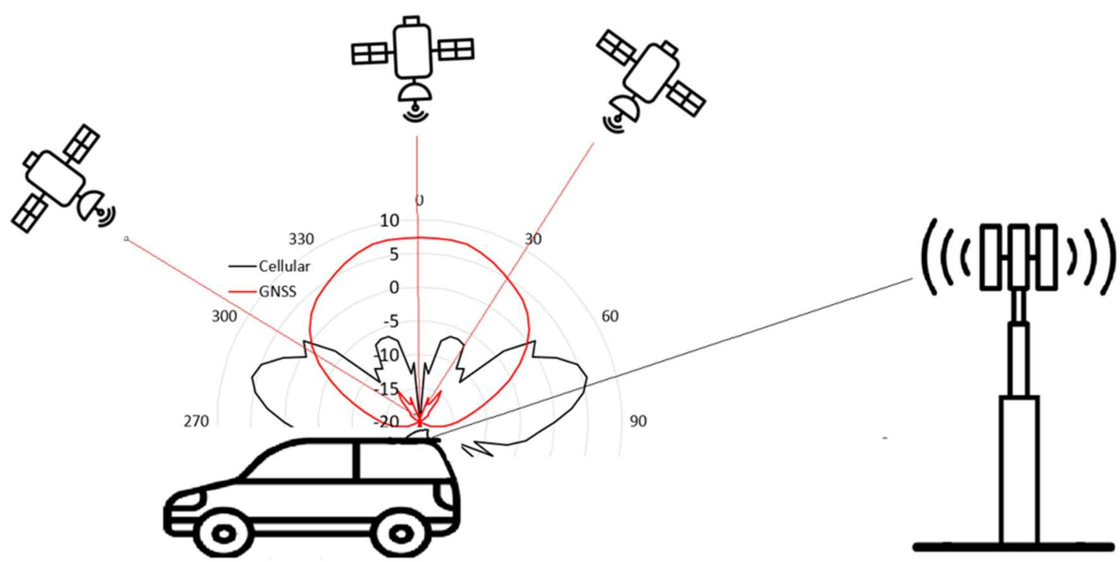

Figure. 1.3: Terrestrial and Satellite Radiation Pattern Requirements for Automotive Antenna

Automotive antenna performance is primarily characterized in terms of Azimuth linear average gain (LAG) for each frequency and elevation calculated as equation (1.1) to ensure enough gain toward the intended elevation angles across the frequency bandwidth and for omnidirectionally and to guarantee adequate coverage over 360 degrees around the vehicle standard deviation calculated equation (1.2) is mainly used.

$$LAG(f,\theta)_{dB} = 10\log_{10}\frac{\sum_{1}^{N\emptyset} G_{lin}(f,\theta,\emptyset)\cos(\theta)}{N\emptyset} \tag{1.1}$$

$$STD(f,\theta)_{dB} = \sqrt[2]{\frac{\sum_{1}^{N\emptyset}(G_{dB}(f,\theta,\emptyset) - \overline{G_{dB}(f,\theta)})^2}{N\emptyset}} \tag{1.2}$$

Where $N_{\o}$ is the number gain measurement point over the 360-degree azimuth ($\emptyset$) for fixed frequency (f) and elevation (θ), G_{lin} gain in linear. G_{dB} gain in dB, and (G_{dB} is the average gain in dB.

1.3 Motivation and Challenges

As wireless technologies advance and people become increasingly dependent on wireless services, the demand for faster and more reliable wireless connectivity constantly increases. This brings several design challenges to the antenna design that must be addressed to meet the growing demand for wireless services.

Automotive antenna systems present a unique set of challenges due to the metallic body of the vehicle, packaging difficulties, and the need for specific radiation patterns. In addition, new challenges arise with the introduction of 5G cellular technology, the need for multiple coexisting cellular antennas to support MIMO, and various antenna services such as V2x, L5 GNSS, Wi-Fi, and Bluetooth into a single package. These coexistence antennas can cause coupling between the elements, leading to a loss in performance and efficiency of the antennas and changes in radiation directionality.

The latest 5G wideband spectrum offers the essential bandwidth for faster speeds and reduced latency in advanced technologies. Nevertheless, it also poses difficulties for antenna design. The new 5G spectrum is divided into the sub-6GHz and mmWave bands. Automotive OEMs primarily employ the 5G sub-6GHz bands, which stretch the frequency as low as 617MHz and introduce additional higher frequency bands up to 5.0GHz, as illustrated in the frequency band summary in Table 1.1.

The 5G cellular antenna element needs to cover three ranges of frequencies, including the low band (617-960 MHz), the high band (1710-2690 MHz), and ultra-high band (3300-5000 MHz), it also requires to provide a decent level of rejection for coexisting GNSS services such as L1 (1559-1606 MHz), L5 (1164-1188 MHz), and L2 (1215-1154 MHz).

Frequency range(MHz)	Bands
617 – 960	n71,B12,B29,B28, B13,B14,B20,B5,B8
1710 – 2200	B4,B66,B3,B2,B39,B1,B34
2350 – 2360	B30
2500 – 2690	B40,B7,B38,B41
3300 – 4200	n77,n78
4400 – 5000	n79

Table 1.1: Cellular sub6 GHz frequency Bandes

When designing an antenna element for 5G, the initial obstacle is to cover the lower frequency band while working within a confined packaging size. Typically, a rooftop antenna with a shark fin design is preferred, with a height of approximately 70mm. However, the plastic cover dome and clearance thickness is roughly 4mm, and the mounting base is 8mm, which limits the available space for the designer to a maximum height of 58mm and a width of up to 30 to 40 mm, as illustrated in Figure 1.4. while a normal quarter wave monopole for 617 MHz is 120 mm in height.

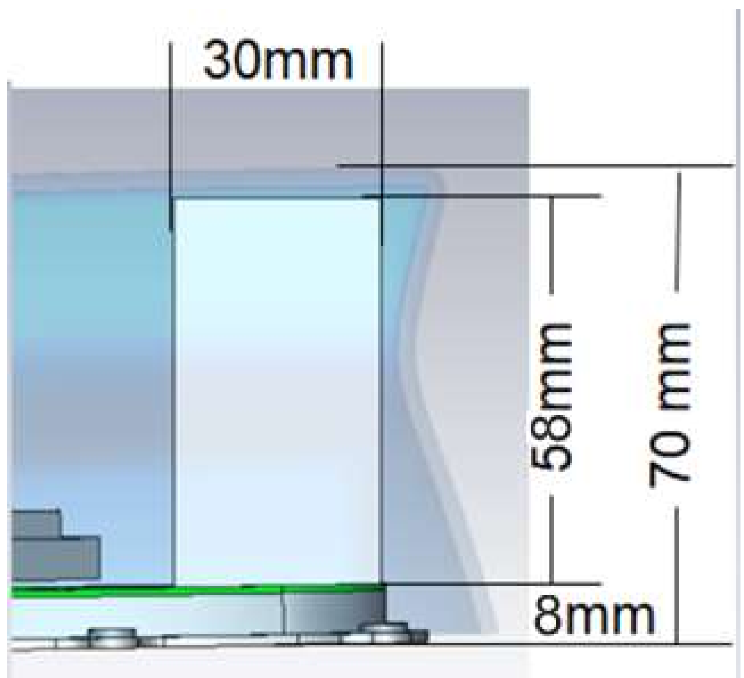

Figure 1.4: Cellular Element size in Vehicle roof top shark-fin Antenna

The second design challenge is ensuring consistent performance across a wide range of frequencies, as mentioned in section 1.2.3. Achieving the necessary performance requirements depends on the radiation pattern and having sufficient gain at specific elevations. However, when the required fractional bandwidth exceeds 100%, the likelihood of unintentionally exciting higher-order radiation modes with undesirable directionality increases. In the case of 5G Sub-6, which has a fractional bandwidth of 150%, most standard structures are unlikely to have the optimal elevation radiation pattern with basic antenna structures.

The third challenge comes with increased antennas that must coexist within a single package. These services encompass various technologies, including AM, FM, DAB, 5G MIMO, GNSS, SiriusXM, Wi-Fi, Bluetooth, and more. Packaging all service antennas into a single unit offers vehicle manufacturers several advantages, such as easier implementation, a simplified assembly process, and reduced costs. However, coupling increases as the antennas are closer, leading to decreased efficiency and performance. In order to achieve simultaneous operation of all antennas in the same package, adequate isolation and filtration between the antennas becomes crucial. In some cases, sensitive services such as GNSS may experience a total loss if adjacent transmitters jam it. So careful arrangement and adequate antenna spacing lead to larger package sizes.

An alternative method that can aid in packaging multiple antennas into a limited space while operating at different frequencies involves consolidating them into a single antenna structure. This task is easier if the antennas share similar polarization and radiation pattern requirements as in a multi-band antenna Like 5G cellular, Bluetooth, Wi-Fi, … etc. Still, it becomes more difficult if each antenna has distinct requirements, such as with GNSS and 5G cellular antenna elements. The design concept using CMA that combines both functionalities of GNSS and 5G cellular is illustrated in Chapter 4.

1.4 Literature Survey

1.4.1 Wideband monopole for Automotive 5G sub-6GHz

The wideband antenna structures with one consistent radiation pattern for all frequencies are known as frequency-independent structures [6]. Conical antennas are one of those structures that would provide an omnidirectional radiation pattern that meets automotive requirements as in [7]; however, the size and shape of this structure are difficult to implement on vehicles due to styling constraints. Other wideband solutions include the planar wideband structure in [8,9]; in addition to the large size, the elevation pattern has low gain at low elevation angles in frequencies around 2.5 GHz and 4 GHz, respectively, due to the interruption of the higher-order modes. Multi-branch design concepts, as in [10,11], would improve the gain at lower elevations gain. However, the azimuth pattern loses omnidirectionality at higher frequencies due to its non-symmetrical design and blockage from longer branches. Automotive antenna designs [12-14] only consider LTE 4G bands covering only 700-960 MHz and 1700-2700 MHz .

Recent antennas designed for 5G sub-6GHz bands would fit the shark-fin style [15-18]. Still, none of those have discussed optimal radiation patterns for both the azimuth plane (H-plane) and the elevation plane (E-plane). In [15], directionality is degraded for frequencies higher than 2.1 GHz. In [16], the antenna exhibits good omnidirectionally; however, it has low gain at lower elevations, as shown from the plots for 2.64 GHz and 3.42 GHz. In [17], the linear average gain (LAG) has a gain drop in the frequency range between 2.4 - 3.8 GHz and degradation in omnidirectionality for frequencies beyond 3.9 GHz. Similarly, for the antenna design in [18], the radiation pattern loses directionality at 3.3 - 5 GHz, and its LAG decreases in the frequency range between 4.2 - 5 GHz.

According to the literature cited above, while some antenna designs would cover the intended frequency range for 5G-sub6 GHz with good efficiency. However, issues with the radiation pattern still negatively impact the performance. Specifically, there is a reduction in gain for a portion of the frequency range and/or loss of the antenna's omnidirectionality. Therefore, the study of using CMA to design and address the deficiency in radiation pattern and provide an optimized solution is discussed in Chapter 3, where two wide-band monopoles cover a portion of the frequency range with first-order mode and provide a continuity radiation pattern for all bands of 5G cellular.

1.4.2 Multi-function GNSS and 5G cell Antenna Structure

Cellular and GNSS services are the most fundamental wireless functionalities for automobiles. GNSS provides navigation services, cellular offering high-speed data access and facilitating information exchange for various purposes. Furthermore, the coexistence of GNSS and cellular technologies would provide additional services like vehicle tracking, fleet management, and enhanced safety and security features.

Typical system implementation for the coexistence of GNSS and Cellular antennas is to use separate antenna for each function. GNSS usually uses a ceramic patch antenna packaged with the cellular element in a shark fin, as in [20,21]. Lower-profile cellular antenna such as a PIFA allow GNSS elements to be stacked on top as in [22] or lined side by side as in [23]; other lower-profile integration solutions are discussed in [24,25] but only cover narrow ranges for the cellular bands. Limited literature discusses single-structure antenna solutions for both GNSS and cellular functionality. A broadband monopole 5G sub-6GHz monopole that covers the GNSS frequency range is presented in [18]. However, the GNSS radiation pattern continues to be omnidirectional and linear polarized, which is not optimal for GNSS system performance.

The solution discussed in Chapter 4 illustrates using CMA to combine two basic antenna geometries in a single structure by superimposing their modes to generate the required radiation characteristics for cellular and GNSS functions. The design concepts achieve the required performance while minimizing size, complexity, and cost.

1.5 Research Objective and Methodology

This research aims to utilize the characteristic mode method theory to improve automotive antenna radiation patterns and overcome the latest challenges associated with merging the new 5G frequency bands and the coexistence of GNSS services. It extends the cellular coverage to a new low frequency of 617 MHz while maintaining high performance across the entire band up to 5GHz. The characteristic mode analysis was mainly used to integrate multiple structures into a single antenna structure with the combined modes that achieve the target requirement.

In the first portion of this study discussed in Chapter 3, the design concept combines two wide-band monopoles to have a continuity in the radiation pattern to cover the new frequency range for 5G cellular optimized for automotive. And provide high rejection at the GNSS frequency range to allow easy integration. The second potion in Chapter 4 merges a PIFA structure known for omnidirectional and linear polarization, suitable for 5G cellular sub-6 GHz with a flat plate with a U-slot for GNSS with circular polarization and hemispherical radiation pattern. This allows the antenna to operate for both GNSS and cellular functions simultaneously.

Characteristic mode analysis gives direct insight into the antenna's working mechanism. It mainly decomposes the complex electromagnetic fields of an antenna into a more straightforward orthogonal radiation mode. Each mode is associated with a particular structure geometry, size and shape despite the excitation applied. The research methodology utilizes this understanding of antenna structures' characteristic modes to merge geometries and synthesize the desired radiation pattern. It can be used to extend the same radiation pattern or diverse radiation patterns, thereby enabling multiple functionalities.

CHAPTER TWO
THEORY OF CHARACTERISTIC MODE

2.1 Introduction to the theory of characteristic modes

Characteristic mode analysis is a powerful technique used in antenna design to identify and analyze the Antenna structure resonances and radiation modes supported by an antenna. CMA provides insights into the antenna radiation mechanism, which helps antenna engineers optimize antenna design radiation modes at specific frequency ranges to achieve the performance requirements, including antenna bandwidth, radiation patterns optimization, input matching, antenna miniaturization, efficiency enhancement, and decoupling between multiple antenna elements[57,58].

In 1965, Garbacz and Turpin [28,29] proposed the theory of characteristic modes (TCM), which established that every perfectly conducting obstacle at a given frequency possesses a particular set of surface currents and corresponding radiated fields that are characteristic of the obstacle's shape and are independent of any specific excitation. However, calculating these characteristic modes was challenging to implement, making it difficult to apply to various object geometries. Consequently, this research topic remained dormant until the 1970s when Harrington and Mautz [30,31] developed a solution based on a weighted eigenvalue equation for the metal body's current and tangential electric field. This solution was later expanded to include lossy dielectric and magnetic materials [32,33].

The theory of characteristic modes has evolved over the years, it was not intensively used until computers and numerical computation became more potent for analyzing different geometries. One significant development is the application of Characteristic mode analysis (CMA) to practical antenna design problems. However, it continues to be an active area of research in electromagnetics[27].

CMA is widely utilized for miniaturizing antennas. In scenarios where the packaging or the structure attached to the antenna is comparable in size to the radiating wavelength, a small antenna may not function as the primary radiator. Instead, it is utilized as a probe to excite currents on the supporting structure, making this application highly appealing [34]. This approach was first utilized in automobile UHV land vehicles as in [35-37] and gained popularity after the 2000s with the emergence of the mobile industry and handheld applications[38-41], as the chassis of these devices are proportional to the lower operating frequency. The optimal locations for such small antennas were determined using CMs of the supporting structure.

CMA is also used for improving the isolation between antenna elements. In scenarios where multiple antennas are situated in close proximity to each other, coupling between the antennas can lead to a decline in system performance. In MIMO systems, ensuring good decoupling is vital for optimal cellular system performance. As such, CMA can be utilized to identify the modes responsible for the coupling between the antennas and design a decoupling network that minimizes this effect. This is particularly important for handheld applications, as demonstrated in [42-44].

CMA is widely used for synthesizing antenna radiation patterns, as each CM exhibits a unique radiation pattern. Numerous studies have explored the use of this method for enhancing radiation patterns [45-50]. Also, in a large structure with multi-element radiators, CMA can be used for radiation pattern steering as in [51-53].

2.2 Mathematics of Electromagnetic scattering and radiation

The relationship between the Electromagnetic field and the source of charges and current in a homogenous medium is described using Maxwell's equations, which can be expressed in Derivative form in the frequency domain and dropping the time-dependent factor ($e^{j\omega t}$).

$$\nabla \times \mathbf{E} = -\mathbf{M} - j\omega\mu\, \mathbf{H} \tag{2.1}$$

$$\nabla \times \mathbf{H} = \mathbf{J} + j\omega\varepsilon\, \mathbf{E} \tag{2.2}$$

$$\nabla \cdot \mathbf{D} = \rho_e \tag{2.3}$$

$$\nabla \cdot \mathbf{B} = \rho_m \tag{2.4}$$

Where **E** is defined as the electric field intensity (volts per meter)

H is defined as the magnetic field intensity (amperes per meter)

D is defined as the electric flux density (coulombs per square meter)

B is defined as the magnetic flux density (weber per square meter)

J is defined as the electric current density (amperes per square meter)

M is defined as the magnetic current density (volts per square meter).

ρ_e is the electric charge density

ρ_m is the magnetic charge density

The simple medium would be described as electric permittivity (ε), magnetic permeability (μ), and connectivity (σ). The changes in an electromagnetic wave while propagating or scattered through different materials can be described by the boundary conditions for both media 1 and media 2 in the equations.

$$n \times (\mathbf{E}_1 - \mathbf{E}_2) = -\mathbf{M}_s \quad (2.5)$$

$$n \times (\mathbf{H}_1 - \mathbf{H}_2) = \mathbf{J}_s \quad (2.6)$$

$$n \cdot (\mathbf{D}_1 - \mathbf{D}_2) = \rho_e \quad (2.7)$$

$$n \cdot (\mathbf{B}_1 - \mathbf{B}_2) = \rho_m \quad (2.8)$$

Given that the tangential component electric field and normal magnetic field vanishes on the conductor surface and inside metal material, this would produce the below boundary condition equation in the metallic media.

$$n \times \mathbf{E}_s = 0 \quad (2.9)$$

$$n \times \mathbf{H}_n = \mathbf{J}_s \quad (2.10)$$

$$n \cdot \mathbf{D}_n = \rho_e \quad (2.11)$$

$$n \cdot \mathbf{B}_s = 0 \quad (2.12)$$

When an Electromagnetic plane wave hits a metallic object, a surface current J_s will be induced on the outer surface; because of tangential magnetic field and/or normal Electric field as described in equations 2.10 and 2.11, this current would then radiate an Electromagnetic field into the free space as illustrated in Figure 2.1, this process depends on the EM frequency and structure shape and dimensions.

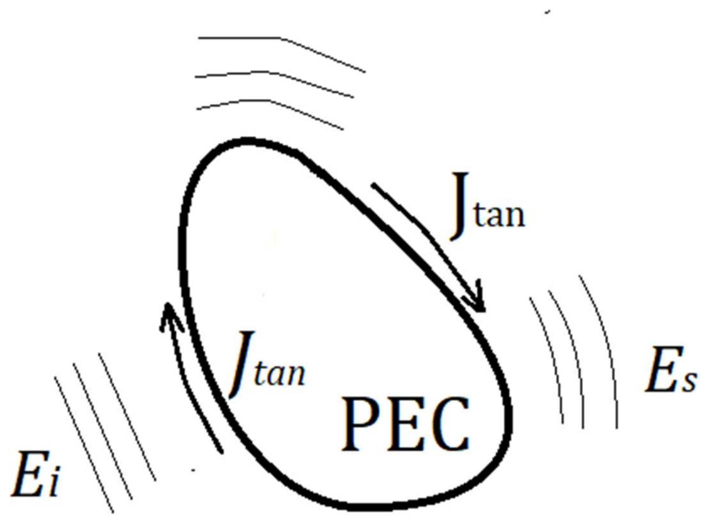

Figure. 2.1: Incident Electric field Ei hit perfect electric conductor (PEC) to induce surface current J_{tan}, the surface current would produce the scattered Electric field Es

To simplify the problem, we would consider a free space to perfect an electrical conductor (PEC) without material losses, as illustrated in Figure 2.1. Solving such radiation and scattering problems starts with Maxwell's Equations, which relate the Electromagnetic fields to current $\boldsymbol{J_s}$ that impressed or induced on the object. The induced surface current can be described by $\mathbf{J} = \sigma\, \mathbf{E_i}$, and by assuming that the magnetic vector potential M=0, then Equations 2.1 and 2.2 can be simplified to

$$\nabla \times \mathbf{E} = -j\omega\mu\, \mathbf{H} \qquad (2.13)$$

$$\nabla \times \mathbf{H} = j\omega\varepsilon\, \mathbf{E} + \sigma\, \mathbf{E} \qquad (2.14)$$

Defining the magnetic vector potential (A) and electric scaler potential quantities (Φ) would simplify the solution for the induced Electromagnetic fields. For electric scaler potential, since the Electric field is always divergent ($\nabla\times$ **E** = 0), we can always describe the electric field by a scaler function (Φ) as in equation 2.16. Similarly, for defining the magnetic vector potential, given that the magnetic field is always solenoid (∇. **H** = 0) it can be expressed in the term curl of a vector function (**A**) as in equation 2.15.

$$\mathbf{H} = \frac{1}{\mu} \times \mathbf{A} \tag{2.15}$$

$$\mathbf{E} = \nabla\Phi \tag{2.16}$$

Using the magnetic vector potential definition in Equation (2.1) and magnetic current (**M**) equal zero, we would get

$$\nabla\times (\mathbf{E}+ j\omega\, \mathbf{A})=0 \tag{2.17}$$

We can also apply the vector identity formula $\nabla\times(\nabla\Phi) = 0$ and then can write the electric field in terms of magnetic vector potential and electric scaler potential.

$$\mathbf{E} = - j\omega\, \mathbf{A} - \nabla\Phi \tag{2.18}$$

Taking the curl for both sides in Equation (2.18) and using the vector identity $\nabla\times\nabla\times A = \nabla(\nabla.A) - \nabla^2 A$, together and after simplifying, we would end up with Helmholtz integral equation, which can provide the electric field for any surface current in PEC material

$$\mathbf{E} = -j\omega\mu\,\mathbf{A} + \frac{1}{j\omega\varepsilon}\nabla(\nabla.\mathbf{A}) \tag{2.19}$$

2.3 Surface Integral Equation

Finding the electromagnetic radiation for any scattering problems or antenna analysis requires solving a surface integral equation as shown in equation (2.19), which can be described either as an Electric field integral equation EFIE, where the boundary condition is enforced on the tangential electrical field, or the magnetic field integral equation MFIE where the boundary condition is enforced on a tangential magnetic field. Of course, both ways will lead to the same result. However, we will only proceed considering the EFIE solution for simplicity.

Since both magnetic vector potential (**A**) and scaler electric potential (Φ) are a function of surface current (***J***) as in below, then we can rewrite Equation (2.18) can in terms of the integral operator $L()$ as in below

$$\boldsymbol{E}_s = L(\boldsymbol{J}_{\boldsymbol{tan}}) = -j\omega\mu\,\boldsymbol{A}(\boldsymbol{J}_{\boldsymbol{tan}}) - \nabla\Phi\,(\boldsymbol{J}_{\boldsymbol{tan}}) \tag{2.20}$$

Where **A** and Φ are can be found below the formula :

$$\mathbf{A}(\boldsymbol{J}) = \mu \oiint_S \boldsymbol{J}(\mathrm{r}).\psi(\mathrm{r},\mathrm{r}')\cdot \mathrm{ds}' \tag{2.21}$$

$$\Phi\,(\boldsymbol{J}) = \frac{-1}{j\omega\varepsilon}\oiint_S \nabla.\boldsymbol{J}(\mathrm{r}').\psi(\mathrm{r},\mathrm{r}')\cdot \mathrm{ds}' \tag{2.22}$$

$$\psi\,(\mathrm{r}') = \frac{\exp\,(-jk|r-r'|)}{4\pi|r-r'|} \tag{2.23}$$

Impugning them directly into equation (2.20) will generate the Electric Integral equation.

$$\boldsymbol{E}_s(r) = -j\frac{\mu}{4\pi\varepsilon r}\oiint \boldsymbol{J}_{tan}(r').\,\psi(r,r')|r-r'|\,ds' \tag{2.24}$$

$$\boldsymbol{H}_s(r) = \sqrt{\frac{\varepsilon}{\mu}}\;\; r' \times \boldsymbol{E}_s(r) \tag{2.25}$$

This formula directly relates the electric field to the induced current on the PEC. Once the current is known, electrical and magnetic fields can be calculated at any point in the spherical coordinate relative to the PEC object.

2.4 Method of Moment

The Method of Moments (MOM) is a computational method for solving integral equations. The first step is to divide the surface of the PEC structure into smaller elements known as a mesh. The current in each element can then be digitized and formulated into a matrix equation to determine the global currents. In the context of the Electric Field Integral Equation (EFIE), the matrix represents the mutual impedance, which relates the unknown current on the surface to the incident field. This can be seen in the equation.

The shape of each element is chosen to be a two-dimensional triangle. The local current can be expanded into basis functions that may have different possible representations. The sum of the set of local currents on each mesh element would realize the total surface current.

The popular representation used for the purpose digitizing such a mesh is the Rao-Wilton-Glisson (RWG) is mainly used as an orthogonal base function to represent the current at each local mesh. The RWG has a rooftop-like current distribution over two adjacent elements, as illustrated in Figure 2.2. The RWG can be expressed in the below formula (2.26), where A_m is the area, ρ_m is the length, and lm is the width of each mesh.

$$\boldsymbol{f}_n(r) = \begin{cases} \frac{l_n}{2\,A_m}\rho_m & ,r \in A+ \\ \frac{-l_n}{2\,A_m}\rho_m & ,r \in A- \\ 0 & ,else\ where \end{cases} \tag{2.26}$$

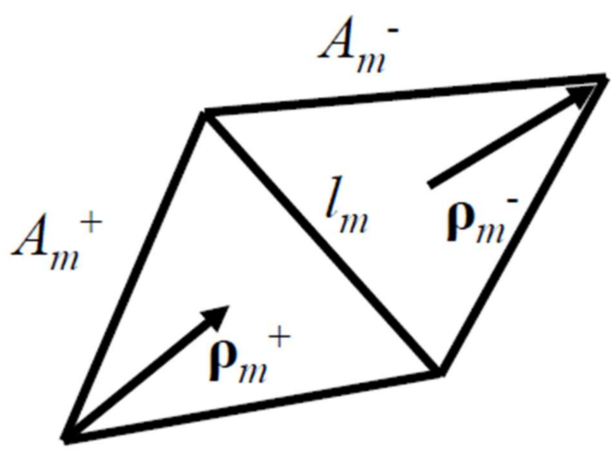

Figure 2.2 RWG current distribution function for each element (mesh)

The RWG basis function exhibits a normal component value at the boundary between the triangle along *lm*, while the normal component of all other edges is zero. This condition guarantees continuity between adjacent triangles, which is another essential property of RWG. Moreover, RWG is divergence conforming, meaning that the divergence is uniform and consistent across the element. This feature ensures that there is no accumulation of charge. We can use a weighted sum of the RWG basis functions to express the surface current on the PCE.

$$\boldsymbol{f}(\mathrm{r}) = \sum a_n \boldsymbol{f}_n(r) \tag{2.27}$$

Inserting the current function directly into the EFIE using Equation 2.27 and the integral operator *L()* we will get $g(r)$.

$$\boldsymbol{g}(r) = \sum a_n L(\boldsymbol{f}_n) \tag{2.28}$$

The weighting coefficient (a_n) can be found according to Galerkin's method by using the same RWG basis functions as a test function and performed inner product between $g(r)$ function and the testing functions,

$$[\mathbf{E}_\mathrm{s}(r)]_\mathrm{m} =< f_m(r'), \boldsymbol{g}(r) > = \sum_{k=0}^{n} a_n < \boldsymbol{f}_m(r'), L(\boldsymbol{f}_n(r)) > \tag{2.29}$$

Applying this method directly to the EFIE in (2.24) results in the linear matrix equation described by

$$[\boldsymbol{E}_s]_m = [Z_{n,m}][\boldsymbol{J}_n] \tag{2.30}$$

When solving for surface currents of a PEC object using the EFIE and proper boundary conditions, the impedance matrix ([Z]) can be found as in (2.31), where ψ(r,r') is the free space Green's function defined by (2.23), and λ is the free space wavelength. The voltage ($[\mathbf{E}_s]_m$) on each basis function is defined by (2.30)

$$[Z]_{m,n} = \frac{j\omega\mu}{4\pi}\iint \boldsymbol{f}_m(r).\boldsymbol{f}_n(r')\ \psi(\mathrm{r},\mathrm{r}')\,ds\,ds' - \frac{j}{4\pi\omega\varepsilon}\iint < ((\nabla.\boldsymbol{f}_m(r)),(\nabla.\boldsymbol{f}_n(r'))> \ \psi(r,r').ds\,ds' \tag{2.31}$$

This solution, which utilizes MoM, allows finding an impedance matrix ([Z]) for any discretized PEC object. The impedance matrix of any object can also be found with generalization lossy and dielectric material if we use a genderized form of EFIE. Finding the impedance matrix of an object is a critical first step in solving for the CMs of any object. as will be shown in the following section.

2.5 Theory Of Characteristic Mode Math

Eigenvalues and eigenvectors are essential concepts in linear algebra, used in many areas to solve mathematics, science, and engineering problems. They are particularly useful in understanding the behavior of linear systems; by composing the Equation system into a set of independent equations, each with a specific eigenvalue can be studied separately from the other values.

By applying the same concept to the scattering or radiation problem, we can express the unknown radiation Electric field as proportional to the current induced on the surface of the PEC object as a MOM matrix of Equation (2.30), where the Z impedance matrix entirely depends on the structure material and shape, the Z matrix can be described in term of the real part and imaginary part.

$$[Z] = [R] + j[X] \tag{2.32}$$

$$[R] = \frac{[Z] + [Z^{*}]}{2} \tag{2.33}$$

$$[\mathrm{X}] = \frac{[Z] - [Z^{*}]}{2j} \tag{2.34}$$

The set of currents found through an eigenvalue decomposition of (2.41) using R as the weighting variable will correspond to an orthogonal set of radiated patterns.

$$[Z]\,[\boldsymbol{J}_n] \; = V_n\,[R][\boldsymbol{J}n] \tag{2.35}$$

Where V_n is the eigenvalue, Jn will be the eigenvector describing the current vector for the nth mode, and R is the far field radiation weighting matrix; by substituting the [Z] to its natural and imaginary component then, we can find that $(V_n = 1 + j\lambda_n)$ and the new matrix set of the Equation can be expressed as where (λ_n) is the new eigenvalue

$$[X][\boldsymbol{J}_n] \; = \lambda_n[R][\boldsymbol{J}n] \tag{2.36}$$

Using the test function $\boldsymbol{J}_m$, we use to decompose the total current of $\boldsymbol{J}_n$ matrix into an orthogonal set of function discrete set of RWG basis functions $\boldsymbol{J}_m$

$$< J_m, [X].[\boldsymbol{J}_n] >= \lambda_n < \boldsymbol{J}_m, [R].[\boldsymbol{J}_n] > \quad (2.37)$$

By defining the delta δ_{mn} function for orthogonality between $\delta_{mn} =< \boldsymbol{J}_m, \boldsymbol{J}_n >$

$$\delta_{mn} = \begin{cases} 1, & m = n \\ 0, & m \,! = n \end{cases} \quad (2.38)$$

And using both Equation (2.37) and (2.38), we can conclude that.

$$< \boldsymbol{J}_m, [X].[\boldsymbol{J}_n] >= \delta_{mn} j\lambda_n \quad (2.39)$$

$$< \boldsymbol{J}_m, [R].[\boldsymbol{J}_n] >= \delta_{mn} \quad (2.40)$$

$$< \boldsymbol{J}_m, [Z].[\boldsymbol{J}_n] >= \delta_{mn}(1 + j\lambda_n) \quad (2.41)$$

Equation (2.37) gives two conclusions first about the orthogonality between the current m of the current vector. J_m , possible orthogonality includes magnitude and polarization.

Second, we can understand how the magnitude of eigenvalues is related to the characteristic field radiation modes by analyzing the complex power as stated in Poynting theory as in the below equation.

$$\frac{1}{2}\iiint (\mathbf{E}.\boldsymbol{J}^*)\, dv = \frac{1}{2}\oiint (\boldsymbol{E} \times \boldsymbol{H}^*) ds + \frac{j\omega}{2}\oiint (\mu|\boldsymbol{H}|^2 - \varepsilon|\boldsymbol{E}|^2)\,.\, ds \tag{2.42}$$

In contrast, the left-hand side of equation (2.30) is an expression of the Scattered or radiated power $\mathbf{E_s}$, which makes it analogous to (2.43)

$$\frac{1}{2} < \boldsymbol{E}_s, \boldsymbol{J}_m^* > = \frac{1}{2} < R.\boldsymbol{J}_n, \boldsymbol{J}_m^* > + \frac{j}{2} < X.\boldsymbol{J}_n, \boldsymbol{J}_m^* > = \delta_{mn}(1 + j\lambda_n) \tag{2.43}$$

The real part of the eigenvalue (λ_n) is a zero, it only affects the [R] operator, and it represents the real radiated power; on the other hand the (λ_n) Is directly linked to the imaginary part and pertains to the imaginary part of Poynting's theorem, which represents the reactive power.

2.6 Characteristic mode parameters and interpretation

A set of parameters can be found from CMA to help understand the antenna operation and characteristic modes; each mode has a characteristic current. (J_n). Then, the total current can be expressed using the weighting factor. a_n As in equation (2.44).

$$\boldsymbol{J} = \sum_{n=1}^{N} a_n \boldsymbol{J}_n \tag{2.44}$$

2.6.1 Eigenvalue physical interpretation:

The matrix equation (2.41) has the eigenvalue (λ_n) which is directly linked to the imaginary of the Poynting power, the value range from −∞ to +∞ . Considering that a mode is at resonance when its associated eigenvalue is zero, it is inferred that the smaller the magnitude of the eigenvalue is, the more efficiently the mode radiates when excited. Additionally, the sign of the eigenvalue determines whether the mode contributes to store magnetic energy ($\lambda_n > 0$) or electric energy ($\lambda_n < 0$), which also can be illustrated by equation (2.40) .

2.6.2 Characteristic angle

Characteristic angles are the angles associated with eigenvalue (λ_n) as defined below

$$\alpha_n = 180 - \tan^{-1} \lambda_n \tag{2.45}$$

From a physical point of view, a characteristic angle models the phase angle between a characteristic current J_n and the associated characteristic field E_n , similar to the λ_n, the mode resonance happens when the characteristic angle is equal to 180 degrees, and the mode has less influence on radiation when the characteristic angle is near 90º or 270º . The radiating bandwidth of the mode can be estimated when characteristic angles are between 135º and 225º.

2.6.3 Modal Significance

The weighting factor a_n in Equation (2.44) can be found by using Equation (2.30) and using the inner product with the orthogonal J_m Set, this will give the below Equation.

$$\sum a_n < Z.\boldsymbol{J}_n, \boldsymbol{J}_m^* > = \sum < E_s, \boldsymbol{J}_m^* > = a_n \, (1 + j\lambda) \tag{2.46}$$

Because of the orthogonality between m and n current segment, a_n can be found only when n=m, and it would represent the current mode contribution and can be expressed as the equation below

$$a_n = \frac{< \boldsymbol{E}_s, \boldsymbol{J}_n >}{(1 + \lambda_n)} \tag{2.47}$$

Equation (2.47) can also be split into two terms: the $< E_s, J_n >$ is named the modal excitation coefficient, with the value depending on how good and correlated is the excitation of the structure to mode *n* current, and the remaining term, this normalized amplitude, only depends on the shape and size of the conducting object named as Modal significant (MS).

$$MS_n = \left| \frac{1}{1 + j\lambda_n} \right| \tag{2.48}$$

The radiating bandwidth of a mode can be estimated as the range of frequencies where the power radiated by the mode is not less than one-half, which corresponds to a radiating field of 0.7 from the max radiating area, BW_n can be expressed as a fraction of the frequency difference (upper minus lower) over the resonance.

$$BW_n = \frac{f_u - f_l}{f_{res}} \tag{2.49}$$

2.6.4 Excitation coefficient of Characteristic Modes

The nominator of equation (2.47) refers to the excitation coefficient, describing the coupling between the excitation and the nth mode current. The value for this parameter helps determine the characteristic current's relationship to the position, magnitude, phase, and polarization of an applied excitation. The higher the value of a particular mode, the more influence and effectively excited by the antenna structure excitation

2.7 Characteristic mode analysis for a wire

To illustrate characteristic mode analysis and its parameters, we use the integral solver for commercial software CST [56] and build a simulation model for a simple wire antenna. For instance, consider a dipole with first resonance 1 GHz, where the total length of the element is 140 mm wire with a diameter of 2 mm. For simplicity, I would assume the wire is made of a perfect conductor and a free-space environment.

After running the CMA tool for the simulation model with no excitation over the frequency range from 0.5 - 6 GHz. The first output of this analysis is the possible current distribution for this structure, which is the set of characteristic mode currents over the length of the wire. The simulation result shows five possible modes at this frequency range as shown in Figure 2.3.

It is vital to notice that all modes satisfy boundary conditions as the current is zero at the edge of the wire. The first current mode $\boldsymbol{J_1}$, is an even mode and excited when the length of the wire is the wavelength ($\lambda/2$), for the frequency 1 GHz, similar to the well-known dipole antenna; for this mode, the current has one peak on the mid of the cable, second order modes $\boldsymbol{J_2}$, has two peaks, and null on the center, this is similar for J_4. Mode 3 and mode 5 are also even, with peak values in the middle of the structure.

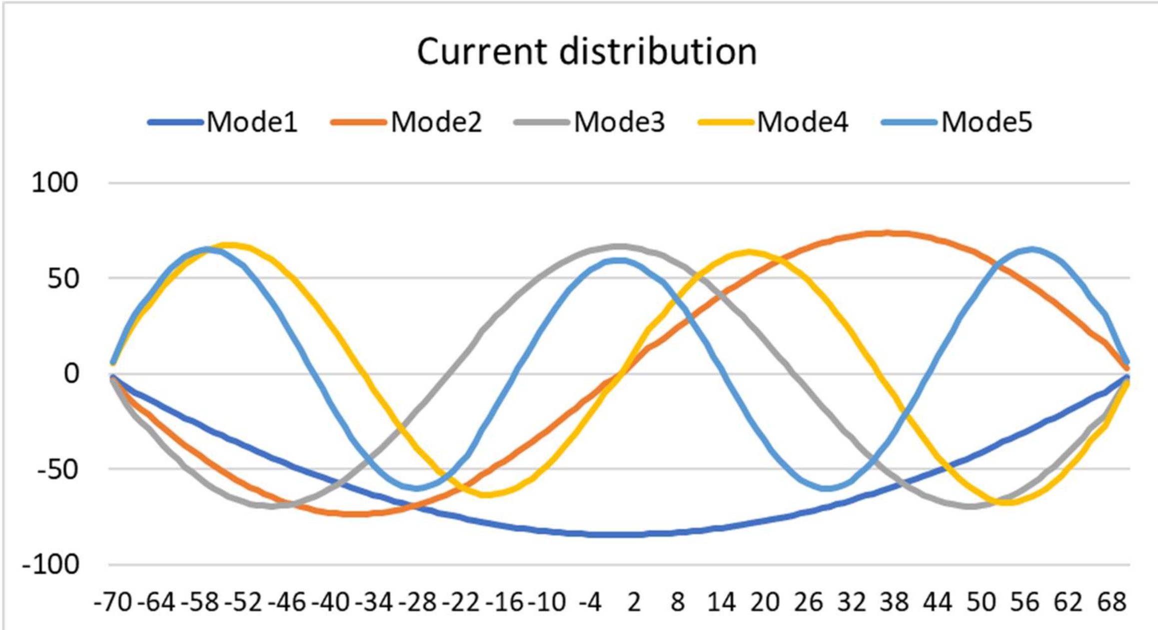

Figure. 2.3: characteristic mode current distribution along half wavelength wire at 1GHz, 140mm length, and 2mm diameter

Using the available commercial EM simulation software with CMA, each mode current can be studied separately, and a radiation pattern can be found for each mode, as shown in Figure 2.4 as the elevation cut for each mode. Mode 1 has the known "donut shape," the omnidirectional radiation pattern. As other modes get excited, different radiation patterns become possible. With this concept in mind, changing the original structure and choosing an excitation position can be used for tuning the antenna to achieve a particular radiation pattern.

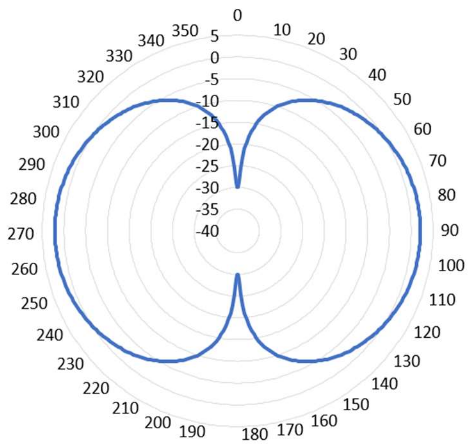

(a) Mode 1 at freq= 1GHz

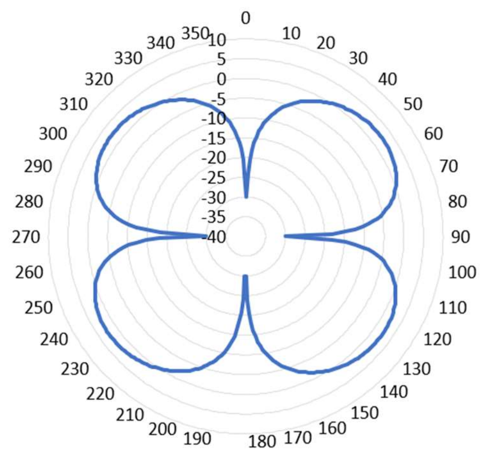

(b) Mode 2 @ freq=2.07 GHz

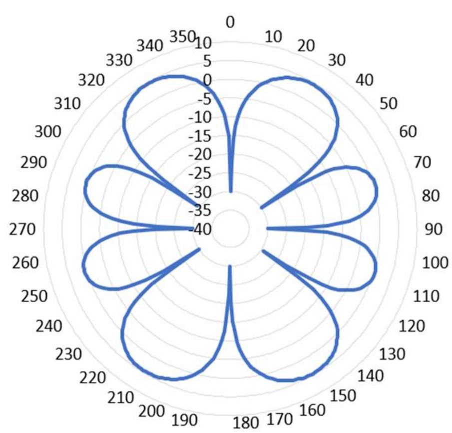

(c) Mode 3 at freq=3.14 GHz

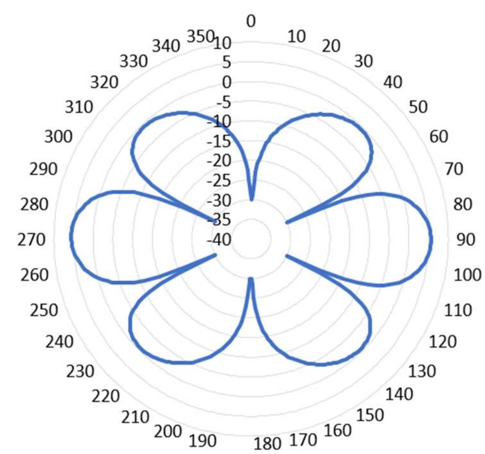

(d) mode 4 at freq= 4.2

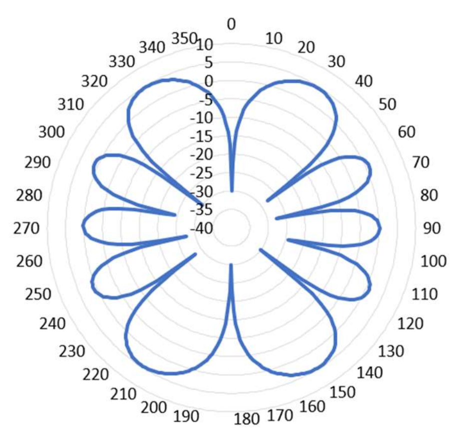

(e) Mode 5 at freq=5.3 GHz

Figure. 2.4: Charactaristc mode electric field elevation cut radiation pattern.

One characteristic mode analysis's mathematical parameter is eigenvalues λn, shown in Figure 2.5 for the 140mm wire example. The plot in the logarithmic scale illustrates the variation when $\lambda_n = 0$, indicating each mode's resonance frequency. Notice that resonance modes become possible for every 1Ghz.

The characteristic angle for each eigenvalue mode is shown in Figure 2.6. It clearly shows the resonance frequency occurs when the characteristic angles =180 degrees and it is aligned with the eigenvalue =0. Mode One resonance is at 1.01 GHz, Mode 2 resonance is 2.07 GHz, Mode 4 resonates at 3.14 GHz, Mode 4 resonates at 4.2 GHz, and Mode 5 resonates at 5.3GHz; also, we can find the estimated bandwidth for each mode as frequency range between 135- 225 degrees, as highlighted in the shaded area in the in figure 2.6.

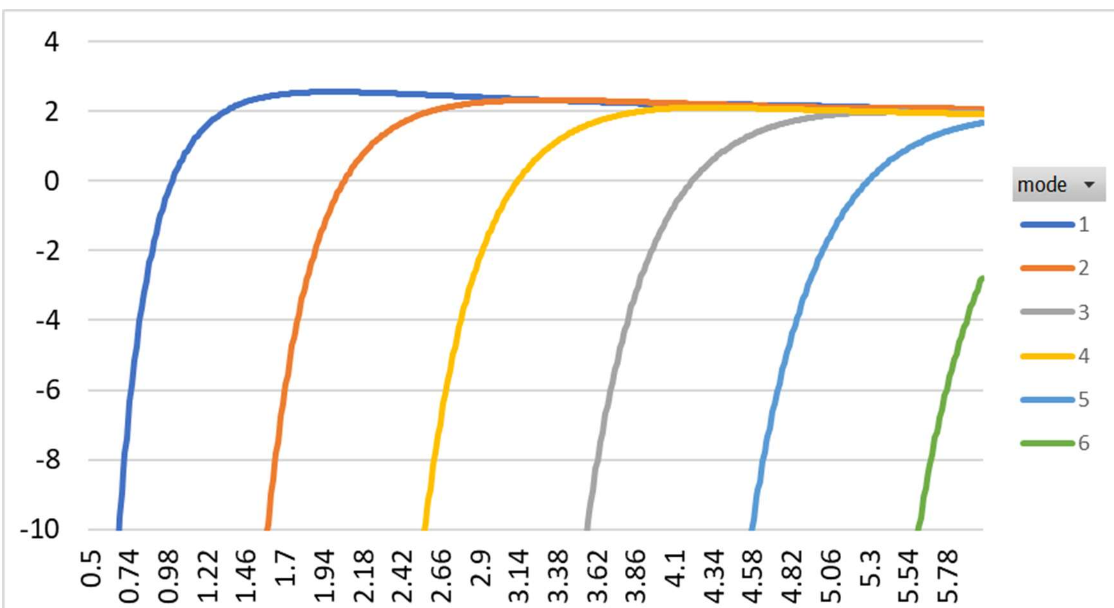

Figure 2.5: Characteristic mode Eigenvalue (λn) for half-wavelength wire

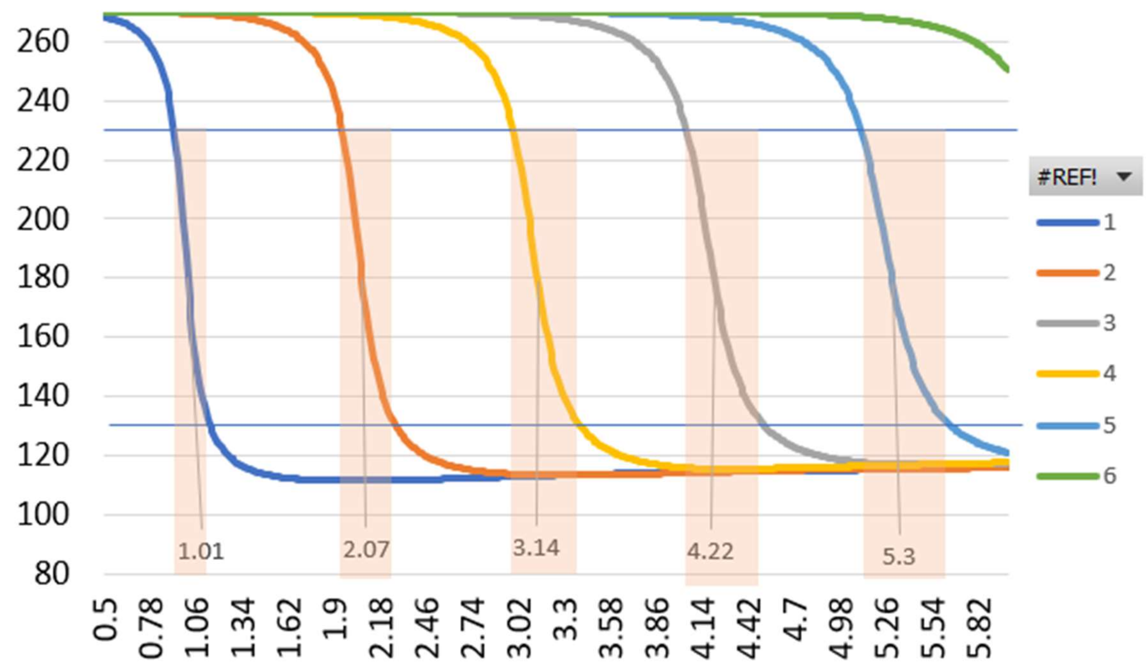

Figure. 2.6: Characteristic Angel for half-wavelength wire

The third output of the characteristic mode analysis is the modal significance. The result for the wire antenna example is illustrated in Figure 2.7. the value of modal significance expresses how well each mode can be excited from this structure at a specific frequency range; maximum radiation would occur at resonance frequency where the energy is radiated real power and is found when MS =1. The second important read of modal significance is the orthogonality of those modes. In this particular example, the modes are orthogonal in magnitude, where only one mode is excited at a specific frequency range. The third conclusion is related to the bandwidth of each excited mode as defined where half power or 0.7 of the MS. Table below shows each mode resonance frequency (f_0) and approximate bandwidth BW.

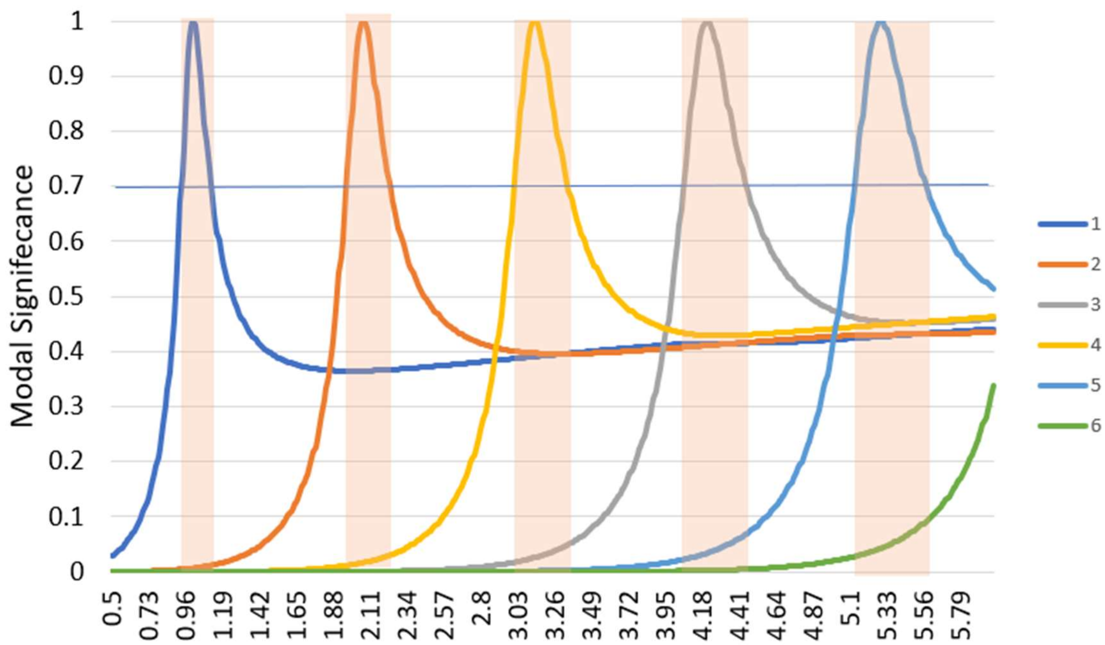

Figure. 2.7: Modal significance for half-wavelength wire

Mode #	Resonance frequency(GHz)	Bandwidth (GHz)
1	1 GHz	0.17
2	2.07 GHz	0.28
3	3.14 GHz	0.34
4	4.2 GHz	0.4
5	5.3 GHz	0.48

Table 2.1: Characteristic mode for half-wave wire Resonance frequency and Bandwidth

If we insert the feeding point in the middle of 140mm as a dipole, only mode 1, mode 3, and mode 5 get excited because those modes correlate with the excitation. This can be found by seeing the weighted modal coefficient that includes both Modal significance and excitation coefficient, as shown in Equation (2.42). Since the current for modes 2 and 4 has a low value at the center, those modes won't be excited.

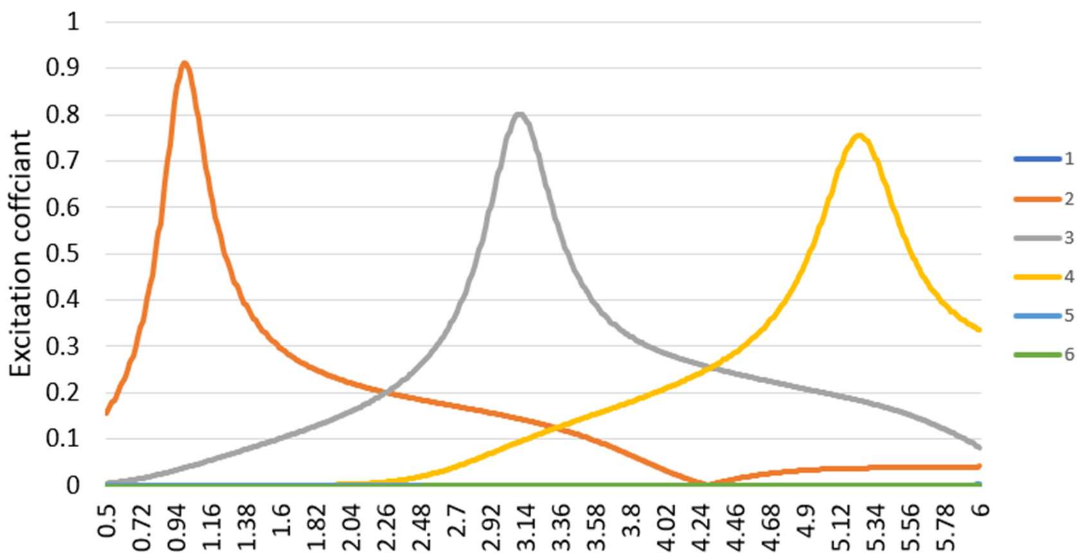

Figure 2.8: Excitation coefficient for the wire Antenna with source feed in the middle

CHAPTER THREE

CONSISTENT RADIATION PATTERN FOR 5G -SUB 6 GHZ PLANER MONOPOLE

Designing wide-band monopole antennas has been studied in multiple works. Most of the time, the study focuses on impedance bandwidth and radiation efficiency. However, For automotive wide-band antenna applications, the antenna must achieve specific radiation patterns for optimal performance. So, this study in this chapter provides an antenna design that provides a consistent radiation pattern across the 5G cellular bands and according to automotive requirements.

First, the broadband radiation pattern issues and the literature survey for the solution designed for 5G monopole for Automotive applications are discussed. Next, illustrate a proposed design and how the characteristic modes are arranged to meet the radiation pattern requirement, including some design parametric sweeps, dimensions, features, and matching circuits. The result of the antenna performance is illustrated in the last section.

3.1 Wideband Monopole Radiation Pattern problems

To illustrate the challenge encountered in designing a broadband antenna for the Automotive industry, we used an example of a typical wideband antenna shown in figure 3.1(a). Its one-sided PCB FR4 size is 58X30X1mm, and the semi-circle bottom feed of this structure would achieve the widest impedance bandwidth according to [64]; simulation VSWR is a figure (3.1-b) even though the impedance bandwidth and radiation efficiency are good, and covering the whole frequency range, this does not reflect the entire picture for the antenna performance. The radiation pattern needs to be considered for the best performance for automotive applications, as discussed in Chapter 2, section 2.2.3.

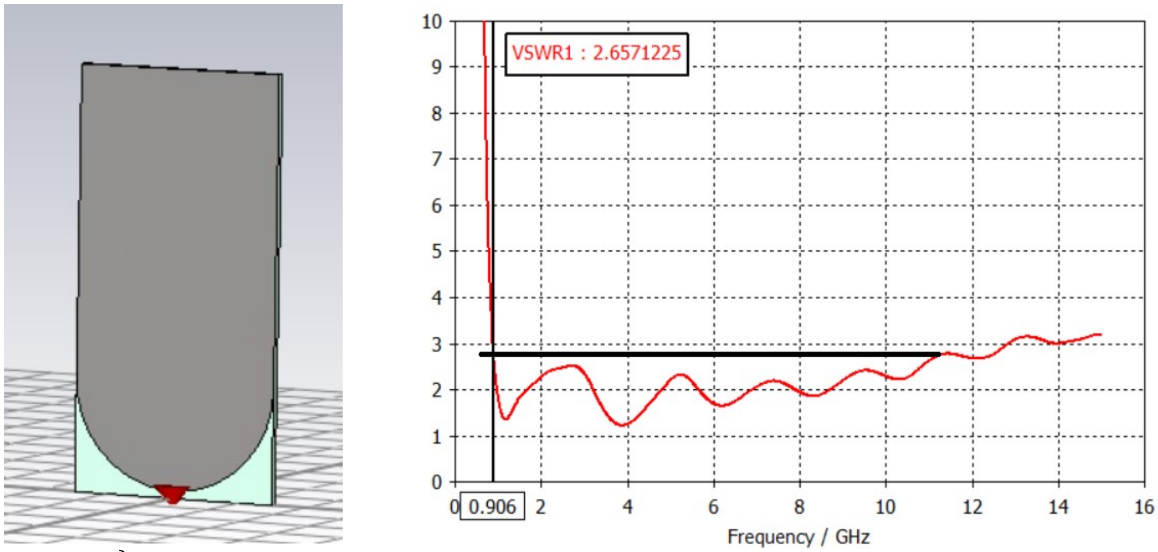

a) structure b) VSWR

Figure. 3.1: Typical Ultrawide planer monopole antenna

Fairfield gains radiation pattern (E-plane) is shown in Figure 3.2 (a), representing linear average gain at each elevation instead of azimuth point. This representation is common in automotive to show how the radiation is distributed per elevation. The figure shows that the frequency range 3.4 -4.8GHz starts to have low gain at the zone of Elevation theta =[80-90] degrees; as discussed in Chapter 2, the optimal cellular performance for automotive focus on the antenna gain at the elevations theta between 60 -90 degrees, which is shown across the frequency range in figure 3.2 (b) to focus on those elevations performance, the drop in the gain is clear in the frequency range 4.4 to 4.8 GHz, it also low frequency 620 MHz has low efficiency and uncovered frequency range due to limited height available for the antenna design.

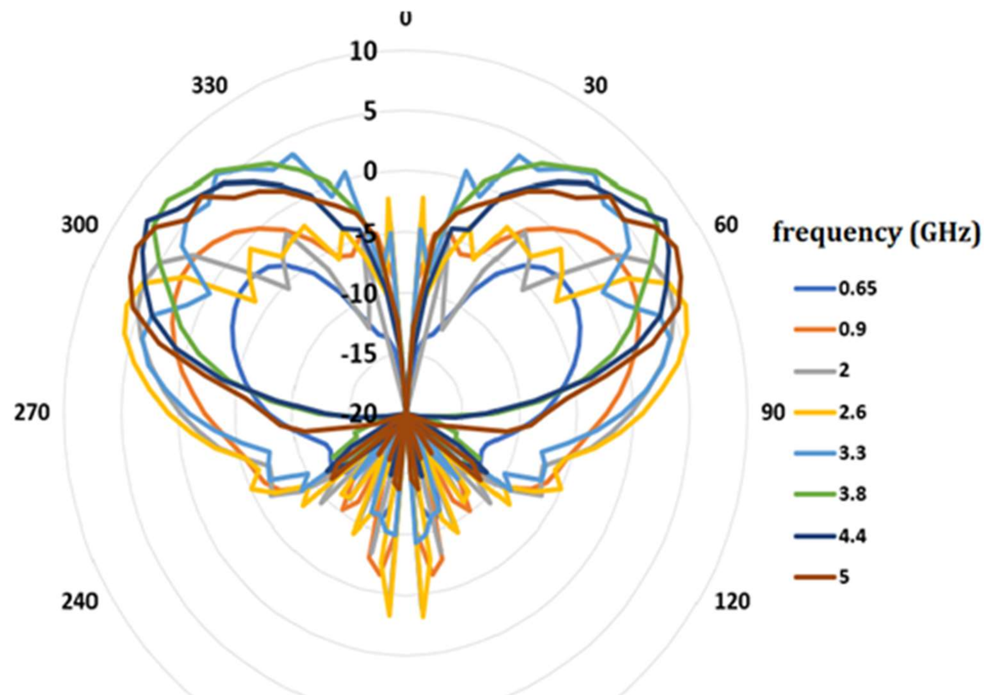

(a)

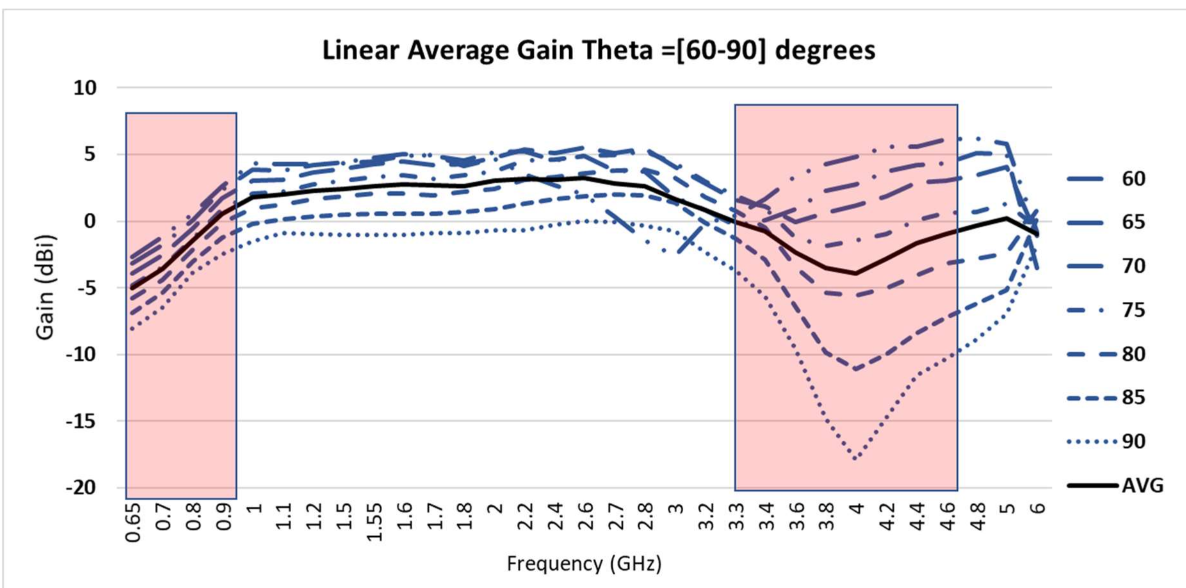

(b)

Figure. 3.2: Drop in the gain for typical wide band design because
a) Elevation cut b) LAG over the frequency range for theta between [60-90]

CMA can explain the undesired radiation pattern behavior and the drop in the gain after analyzing the characteristic modes of the structure and the associated Radiation pattern for each of the excited modes. Typical wideband antenna structure modal significance is shown in Figure (3.3). It shows that mode first, mode 1, has very low modal significance at a low band in the 617 -860 MHz frequency range. This means the antenna has low efficiency at this frequency range. Second, even though mode 1 is a broadband first-order mode that has a good radiation pattern, mode 2 and mode 3 are higher-order modes that get more significance and dominate the operation of the antenna beyond 3 GHz. since mode 2 and mode 3 have the undesired radiation pattern where a null at horizon level as shown in Figure (3.4), the excited radiation pattern will not be optimal for automotive application.

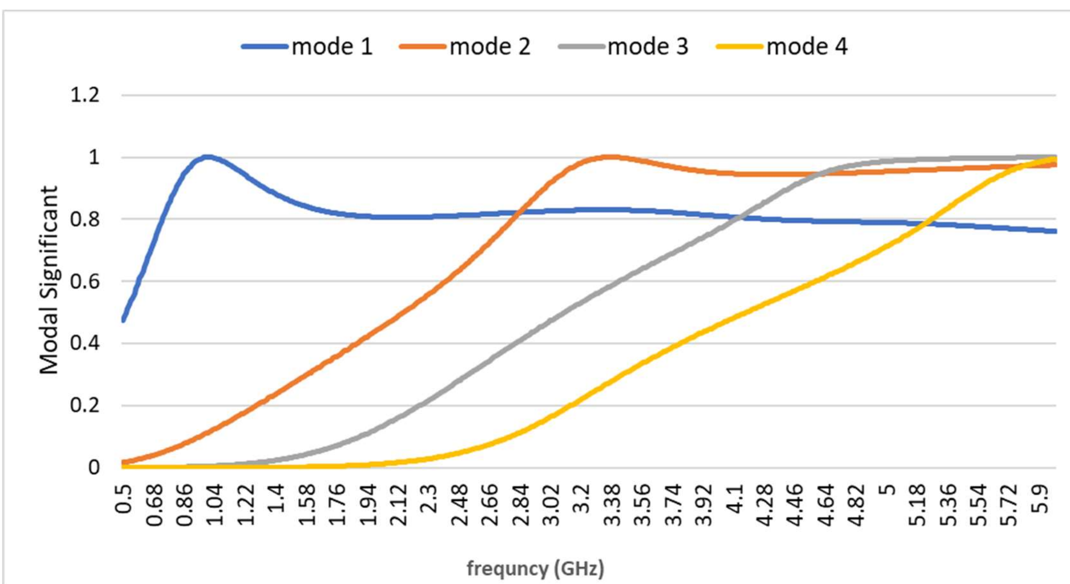

Figure3.3 Modal significance for typical wideband monopole

.

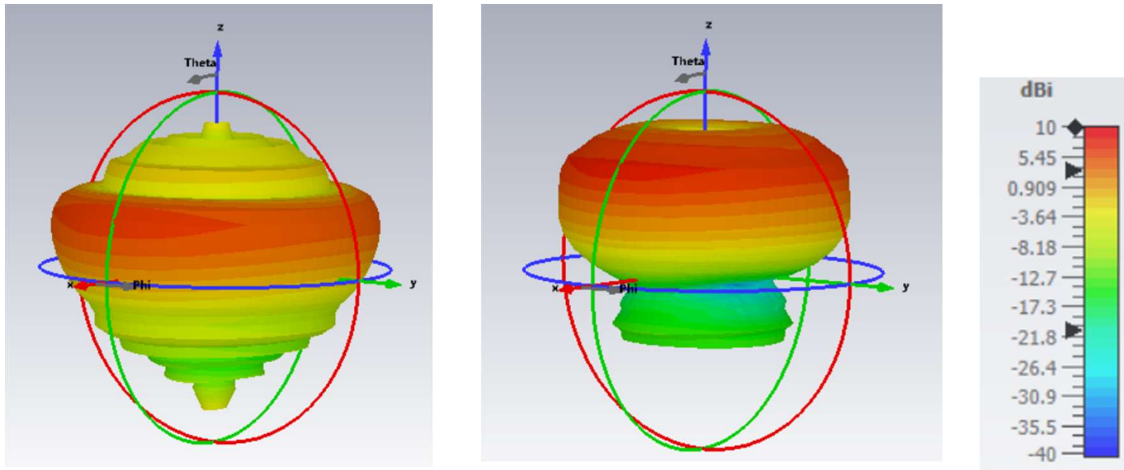

(a) (b)

Figure. 3.4: Monopole Radiation pattern (a) at 2.6 GHz optimal radiation pattern for automotive (b) Radiation Pattern at 3.8 GHz Non-optimal pattern for automotive due to higher order mode

In General, as the required antenna fractional bandwidth increases beyond 100%, the possibility to excite higher order radiation mode increases, 5G Sub-6 fractional bandwidth is 150 %, and most of the standard structure won't have the optimal elevation radiation pattern. Without considering manipulating the higher-order modes

Also, we notice that the first order mode (mode 1) is not low enough to cover 617MHz, which causes a lower band's low efficiency. So, to solve those issues, we need to manipulate the excitation of those modes and first lower the start of the mode 1 resonance to have a more significant value at 617 MHz. This may be achieved by changing the structure with the longer current path to cover low frequency. Second, for the gain drop after 3 GHz, those higher-order modes must be avoided or reduced significantly in the antenna operational frequency range.

3.2 Monopole antenna design for cellular 5G sub 6GHz

Recent antennas specifically designed for 5G sub-6GHz bands have adopted a shark-fin style [15-18]. Even though the VSWR and radiation efficiency are good, none of these designs have thoroughly addressed the optimal of radiation patterns in both the azimuth plane (H-plane) and the elevation plane (E-plane).

The study literature [15] shows that directionality experiences a decline when operating at frequencies exceeding 2.1 GHz. Moving on to [16], the antenna showcases commendable omnidirectional properties; nevertheless, it exhibits reduced gain at lower elevations, as illustrated in the plots for 2.64 GHz and 3.42 GHz. Meanwhile, in [17], the linear average gain (LAG) demonstrates a gain reduction within the frequency range of 2.4 to 3.8 GHz, coupled with a deterioration in omnidirectionality for frequencies surpassing 3.9 GHz. Similarly, the antenna design examined in [18] experiences a loss of directionality in the radiation pattern within the 3.3 to 5 GHz frequency range, with a corresponding decrease in LAG occurring between 4.2 and 5 GHz. This is summarized in the Table below.

The proposed antenna resolves those radiation pattern defects by utilizing the modal analysis to synthesize the intrinsic monopole first-order mode radiation pattern for all operating bands and avoid higher-order modes interrupting the in-band performance. The results show more consistent gain and omnidirectionality across the desired frequency ranges that better match automotive requirements.

Table 3.1: 5G monopole antennas Radiation pattern problem in comparison to the proposed solution

Design Concept	Size and frequency range	Azimuth pattern	Elevation Pattern
The proposed Design, using CMA	Size: 58X30X1 mm^3 Frequency: 617-5000 MHz	Good Omnidirectionality Max-Min = 1 dB at 4.8 GHz	Minimum Average [Theta 90-75] LAG +1dBi at 5GHz
[15] Wideband Vivaldi Monopole for LTE	Size: 69.1x0.86x73 mm^3 Frequency: 700-5000 MHz	Decline in directionality 2.1 – 5 GHz Max-min = 10 dB at 2.5 GHz	Average LAG drops to -3dBi at 2.64 GHz,
[16] Automobile antenna two wide band monopoles	Size: 60x26.4x76 Frequency: 700-6000 MHz	Good Omnidirectionality Max-Min = 2 dB at 5.4 GHz	Average LAG drops to -4dBi at 2.64 GHz
[17] multi-band wideband Design for Vehicular 5G. Two branches with a common base	Size: 38.5x15x60 mm^3 Frequency: 617-5000 MHz	Decline in directionality 2.5 – 5 GHz Max-Min = 7 dB at 5 GHz	Min LAG average Theta [90-75] degrees = -3.4 dBi at 3.4 GHz
[18] Multiband Antenna for Vehicular 5G. Two branches with a common base	Size: 58 × 37 ×17 mm^3 Frequency : 617-5000 MHz	Decline in directionality 2.5 – 5 GHz Max-min= 10 dB at 5 GHz	Min LAG average theta [90-75] degrees = -3dBi at 4.8 GHz

3.3 Proposed Antenna structure.

The idea of the proposed design is to use two structures: long-structure and short-structure; each covers a portion of the frequency range with a first-order mode as a desired radiation pattern mode for automotive applications. The antenna is built on a two-layer FR4 printed circuit board (PCB) with a relative dielectric constant of 4.3. Each structure is printed on one layer and connected at the feeding point, as illustrated in

Figure (3.5-a); the dimensions are shown in Figure (3.5-d).

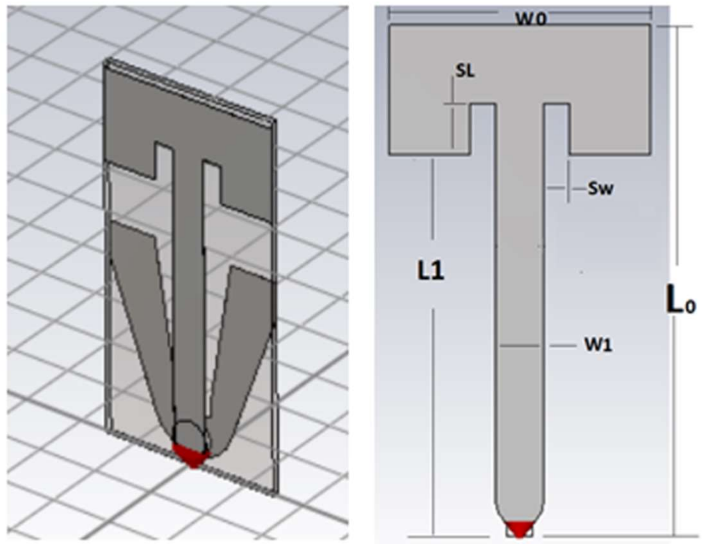

(a) (b)

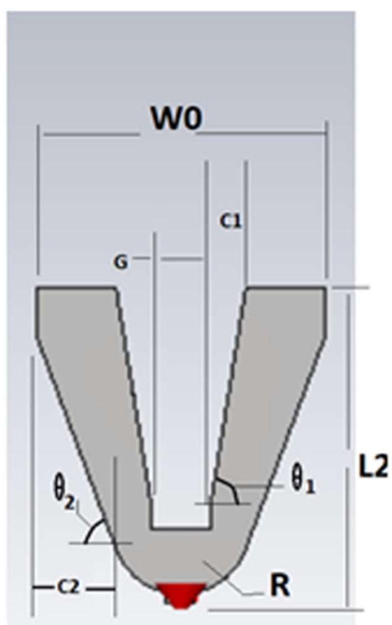

(c)

W0	30 mm
L0	58 mm
L1	44 mm
W1	5.5mm
Sw	3mm
SL	6mm
L2	34 mm
C1	4mm
ϴ1	80 deg
C2	10mm
ϴ2	75 deg
G	6mm
R	7mm

(d)

Figure. 3.5: proposed Antenna structure a) whole structure, b) long-structure, c) short-structure d) dimensions table.

The first structure's top layer, "long-structure" Figure (3.5-b), is a T-shape planar monopole structure that utilizes the height available to cover the low-frequency range of 0.617-0.96 GHz. The second property of this structure is it controls higher-order modes with undesirable radiation patterns in the non-cellular frequency range from 2.7-3.3 GHz and beyond 5 GHz, respectively.

The second structure, "short-structure" Figure (3.5-c), is a wideband planar monopole intended to cover the frequency range from 1.71-5 GHz with a first-order frequency mode and to minimize the influence of higher-order modes prior to 5 GHz by reducing its modal significance. The structure has a trapezoidal gap in the center line to minimize the coupling to the long-structure. In addition, the gap size helps to provide high impedance at the global navigation satellite system (GNSS) frequency band to offer a decent noise rejection and avoid desensitization for possible adjacent GNSS functions. The detailed design parameters are discussed in the following section.

The antenna is intended to be symmetric around the centerline to maintain the roundness of the omnidirectional radiation pattern for the high-frequency bands. The design dimensions were selected based on characteristic mode analysis, which allows for synthesizing and controlling the dominant radiation mode for each frequency range, as described in the following two sections.

3.4 Characteristic Mode Analysis

By running the CMA for the complete antenna structure over an infinite ground plane using CST simulation software, the characteristic angle and modal significance for the first six excited modes are shown in Figures (3.6-a) and (3.6-b), respectively.

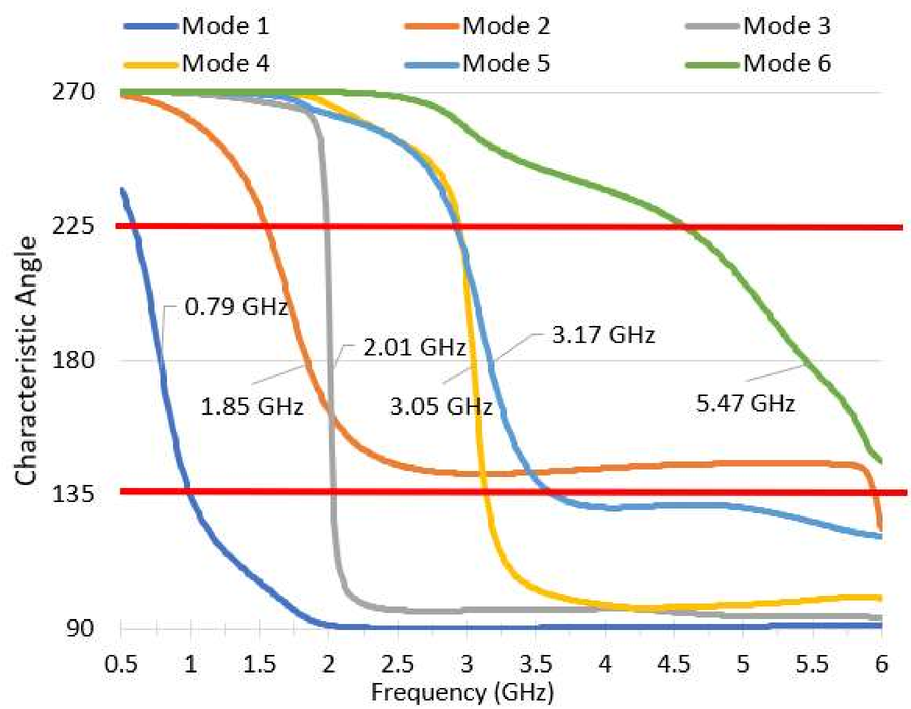

(**a**)

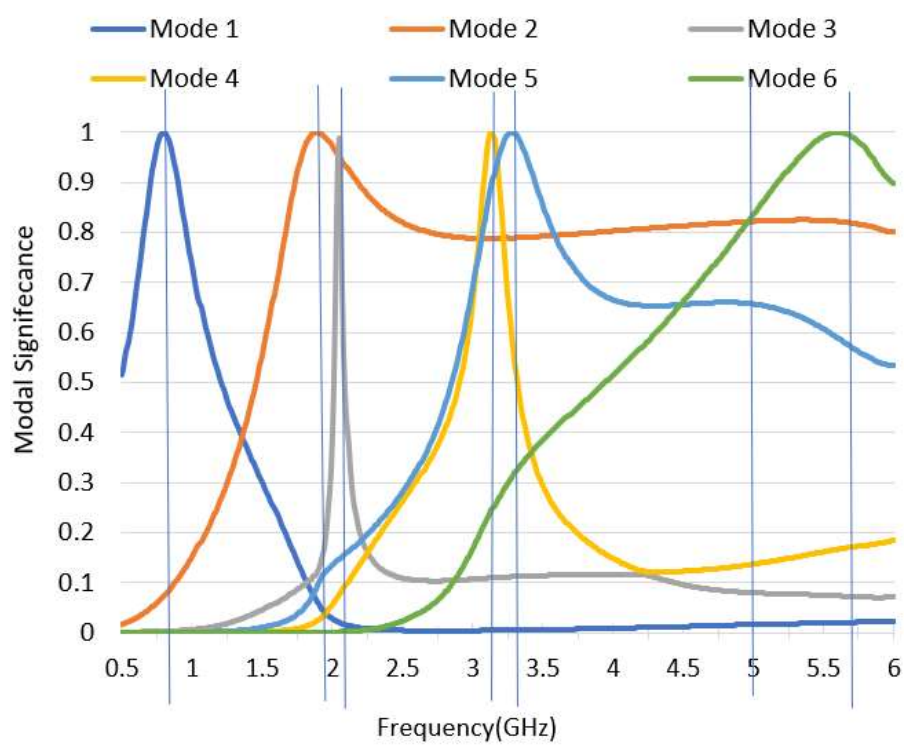

(**b**)

Figure. 3.6: Characteristic Mode Analysis for the proposed antenna a) modal characteristic angle and b) modal significance

Mode 1 resonance is at 790 MHz and shows good potential to cover the low band frequency range from 617 - 960 MHz. The Mode 2 resonance is at 1850 MHz and has potential bandwidth extending from 1.7 to 5 GHz. Mode 3 resonates at 2.01 GHz. Mode 4 and Mode 5 have resonances at 3.05 and 3.17 GHz, respectively. Finally, Mode 6 resonates at 5.47 GHz; it takes over Mode 2 and starts to dominate the radiation performance beyond 5 GHz.

The radiation pattern and the current flow for each characteristic mode are shown in Figures 3.7 and 3.8, respectively. The simulation setup considers infinite ground plane and current mode consider on the whole antenna structure

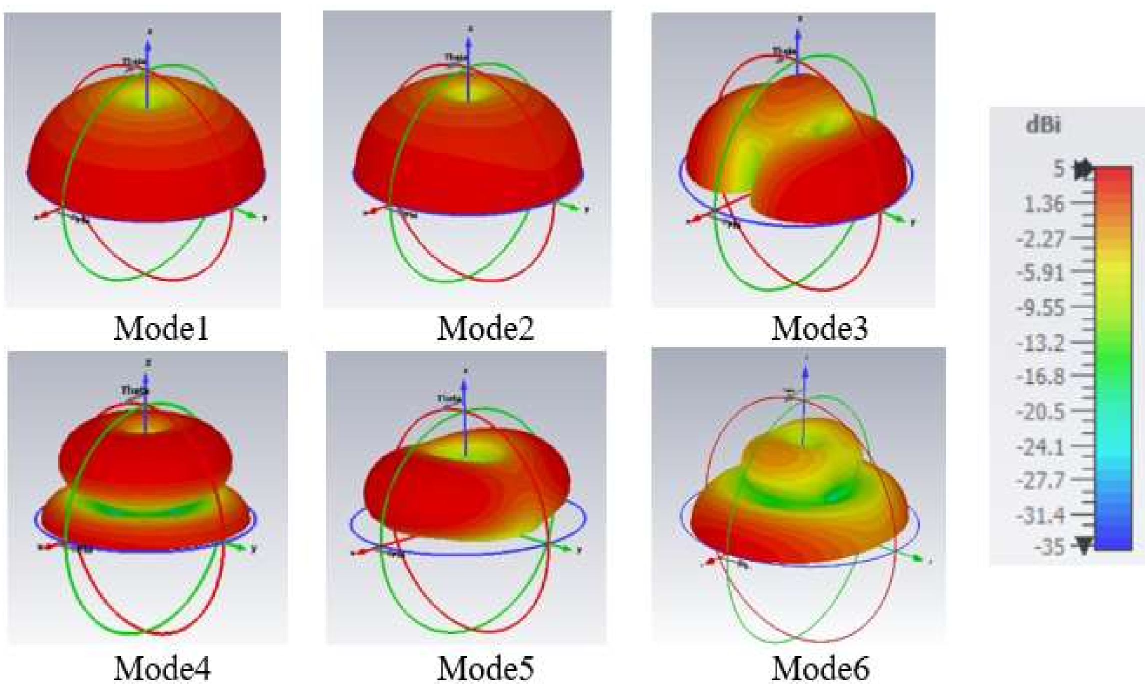

Figure 3.7. Modal radiation pattern (Directivity) at resonance frequencies for Mode 1 at 0.79 GHz, Mode 2 at 1.85 GHz, Mode 3 at 2.01 GHz, Mode 4 at 3.05 GHz, Mode 5 at 3.17 GHz, and Mode 6 at 5.47 GHz

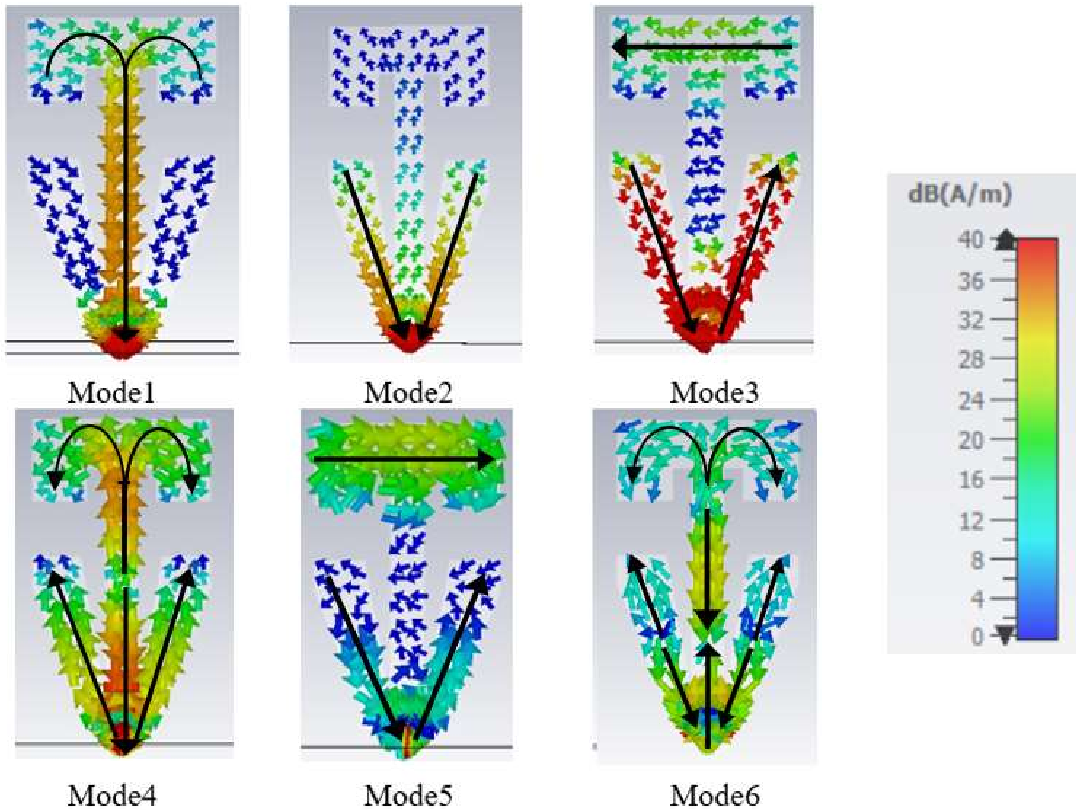

Figure 3.8. Modal current distribution at resonance frequencies for Mode 1 at 0.79 GHz, Mode 2 at 1.85 GHz, Mode 3 at 2.01 GHz, Mode 4 at 3.05 GHz, Mode 5 at 3.17 GHz, and Mode 6 at 5.47 GHz

Mode 1 is a first-order mode excited by the long-structure. Mode 2 is also a first-order mode that is excited from the short-structure. Both Mode 1 and Mode 2 have the desired radiation pattern for automotive applications since they have high gain at the horizon. Mode 3 exists because of the trapezoidal cut in the short structure, which allows the currents to travel parallel to the ground plane; similarly, Mode 5 has currents traveling horizontally across the top of the long structure. Mode 3 and Mode 5 won't be excited with the intended application when the feeding point is at the bottom of the structure. Mode 4 is a combined second-order mode of the long-structure and first-order mode of the short-structure. Its radiation pattern is null at low elevations, making it unsuitable for the automotive requirement. Thus, the structure was tuned to narrow bandwidth and has low modal significance in the cellular bands, as will be discussed in the next section. Mode 6 combines the long structure's third-order mode and the short structure's second-order mode; the radiation pattern has an elliptical shape in the azimuth plane. Since both Mode 4 and Mode 6 interrupt the operation of Mode 2, causing undesired radiation patterns, it is vital to tune those out of the operational frequency range of 2.7 – 3.3 GHz or beyond 5 GHz.

3.5 Antenna structure tuning

Using the CMA tool, modal significance was monitored while changing the structure dimension to set each mode on the intended frequency range, as shown in the previous section, where the desired mode has high modal significance over cellular bands, and undesired modes have low modal significant value in the cellular frequency ranges.

3.5.1. Long-structure Tuning

The long structure has three radiation modes shown in Figure 3.9: Mode 1, Mode 2, and Mode 3 correspond to Mode 1, Mode 4, and part of Mode 6 in the whole structure characteristic mode analysis discussed. Mode 1 is intended to have a first-order mode in the frequency range from 617 - 960 MHz, Mode 2 and Mode 3 are higher-order modes that need to be avoided from cellular bands in the frequency range of 2.7 - 3.3 GHz and beyond 5 GHz, respectively. Therefore, the modal significance metric was used to adjust each mode's frequency range while sweeping the three main dimensions of the long-structure W1, L1, and SL, shown in Figure (3.5-b).

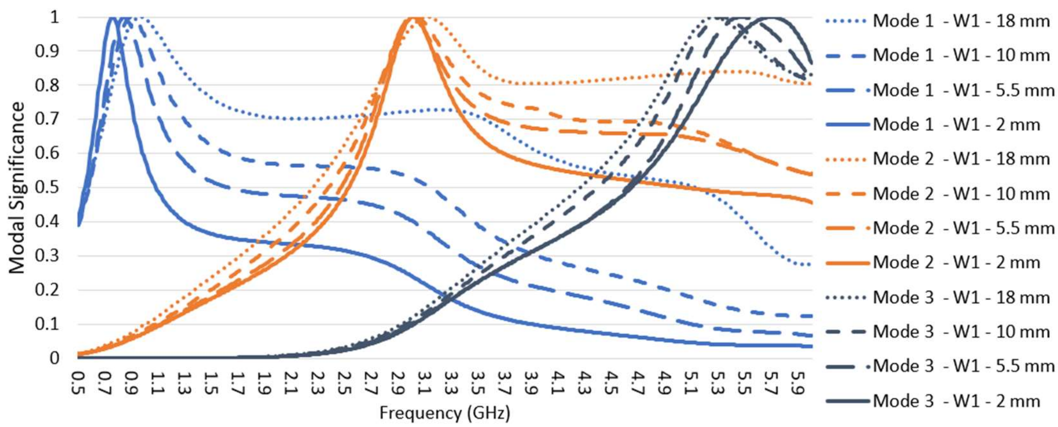

(a)

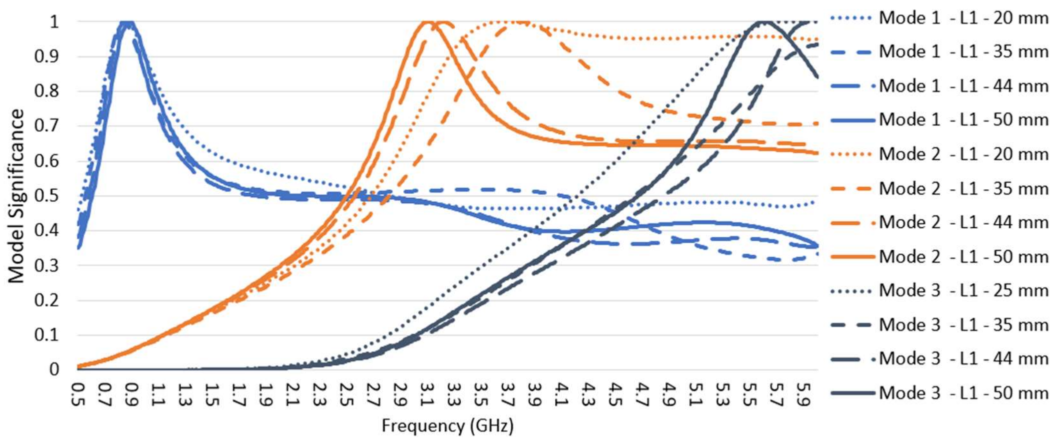

(b)

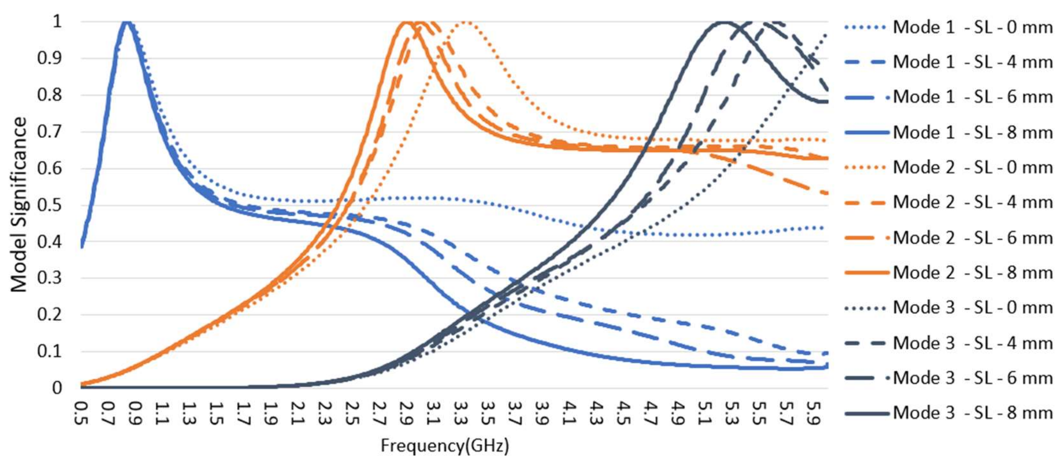

(c)

Figure 3.9. Modal significance for the long-structure while varying three dimensions in Figure 3: a) vertical width W1 b) vertical height L1 c) slot SL

The width W1 was evaluated at the following values {2,5.5,10,18 mm} for L1= 44mm and SL=6mm; the results are shown in Figure (3.9-a). As W1 decreases, the resonance for Mode 1 shifts down to cover lower frequencies, Mode 3's resonance shifts up in frequency, while Mode 2's resonance is unchanged. Also, the potential bandwidths for Mode 1, Mode 2, and Mode 3 decrease. Therefore, the design value selected was 5.5 mm, mainly to maintain sufficient bandwidth of Mode 1 to cover the low-frequency range of 617 - 960 MHz.

The dimension L1 was evaluated at L1 = {20, 35, 44, 50 mm}, for W1 = 5.5 mm and SL= 0 mm. The corresponding modal significance values are plotted in Figure (3.9-b). As L1 increases, the bandwidth for Mode 2 significantly decreases, and its resonance shifts down toward the intended non-cellular frequency range of 2.7-3.3 GHz. The design value selected was 44 mm, showing a decent narrow bandwidth for Mode 2 and lower modal significance for Mode 3 before 5 GHz. Any higher L1 will start affecting the Mode 1 modal significance at 617 Mhz. Since Mode 2 still has high modal significance at 3.3 GHz, it needs to be further adjusted by tuning SL slot dimension.

The slot SL was evaluated at SL = {0, 4, 6, 8 mm} for L1 = 44 mm and W1 = 5.5mm. The modal significance results are plotted in Figure (3.9-c). The SL slot serves as a fine tune and a compromise between Mode 2 and Mode 3. As SL increases, Mode 2 and Mode 3 shift down in frequency, while Mode 1 has a non-significant bandwidth change. The design value was selected as 6 mm to get Mode 2 in the right spot in the middle of the non-operational frequency range of 2.7 - 3.3 GHz and to stop the lower edge of Mode 2 and Mode 3 from having significant values for frequencies at 2.7 GHz and 5 GHz, respectively.

3.5.2. Short-structure Tuning

The short structure has two modes shown in Figure 3.10: Mode 1 and Mode 2 correspond to Mode 2 and part of Mode 6 in the whole structure characteristic mode analysis discussed in section 3.2.2.

Mode 1 is intended to cover the frequency range from 1.71 to 5 GHz with the first-order mode with the desired radiation pattern. Mode 2 is a higher-order mode that needs to be avoided from cellular bands. The short structure was tuned to result in a low modal significance before 5 GHz to achieve this.

Three different feed widths were analyzed to find optimized structure for the short structure, All shapes have a semi-circle feed shape with radii of 15 mm, 7 mm, and 3 mm; also, the three shapes share the outer dimension top widths of 30 mm and total heights of 34 mm, as shown in Figure 3.10.

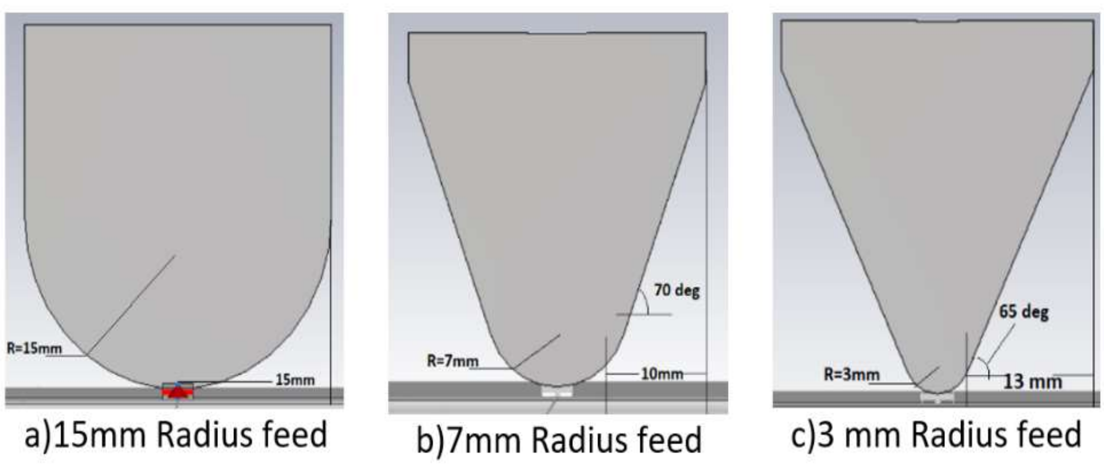

Figure 3.10. Short-Structure feeding width

The modal significance and return loss data for the three feed sizes are shown in Figure 3.11 and Figure 3.12, respectively.

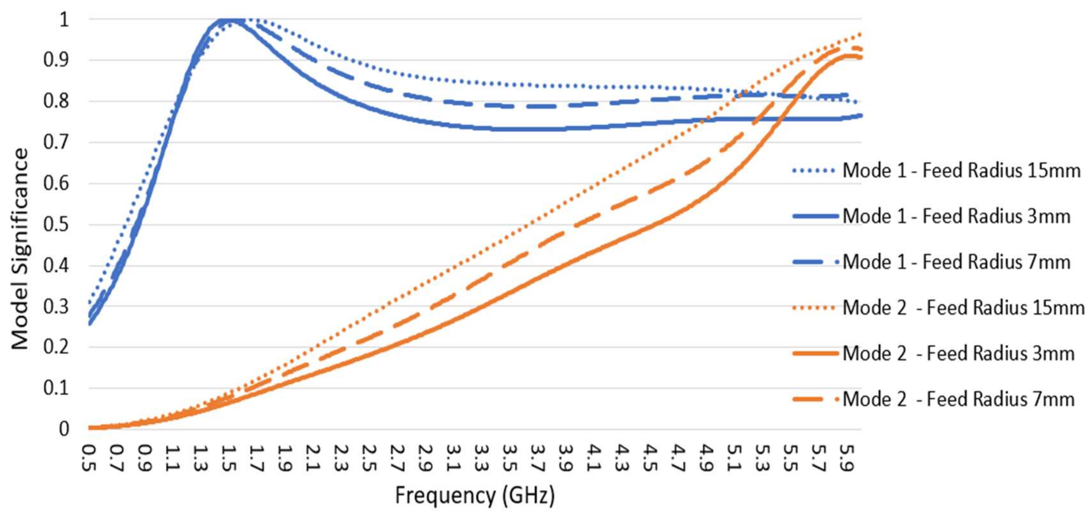

Figure 3.11. Modal significance for the three feeding sizes is shown in Figure 3.10.

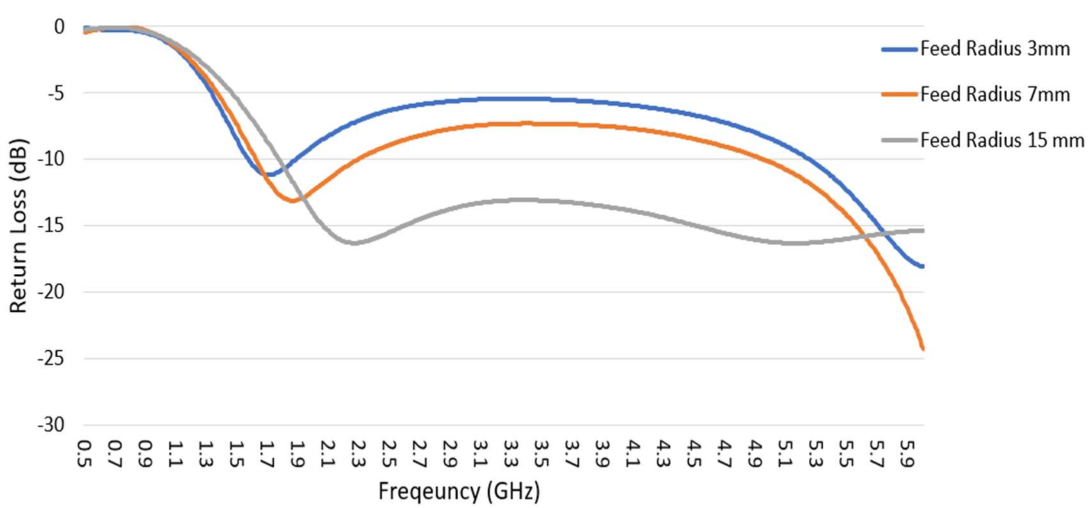

Figure 3.12 Return loss for the three feeding sizes, as shown in Figure 3.10.

As the feed width decreases, Mode 1 resonance frequency barely changes; however, the modal significance value decreases in the frequency range 2.3 – 5GHz, which also introduces higher return loss, as shown in Figure 3.12. Similarly, for Mode 2, as the feed width decreases, the modal significance value decreases for frequencies before 5 GHz, which helps to reduce the effect of this undesired mode. Therefore, the compromised design feed radius selected was 7 mm, to maintain adequate modal significance and return loss below 7dB for Mode 1 while getting lower modal relevance to Mode 2.

3.5.3. Combining Long and Short Structures

Even though the short and long structures operate on different frequency ranges, the direct connection between the two systems won't give the expected complex admittance sum, as illustrated in Figure 3.13, because the coupling between the two structures generates a mutual impedance and changes the excitation mechanism between the structures. Thus, a trapezoidal cut was introduced in the short-structure to minimize the coupling.

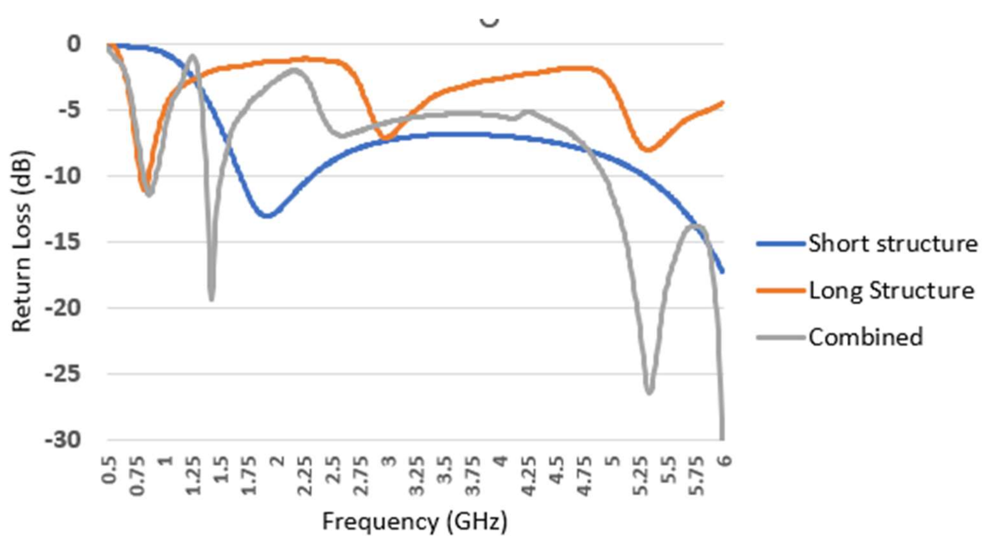

Figure 3.13. Return loss for long structure, short structure, and direct combine

The return loss was monitored in Figure 3.14 with a different value of ϴ1 while keeping G = 6mm in Figure 3.5c. As ϴ1 increases, the coupling between the long and short structures decreases. And the high band frequency resonance moved toward higher frequencies and achieved a better 50 ohm impedance match in the mid-frequency range. The design value ϴ1 was selected to be 80 degrees to maintain a good match at 1710 MHz.

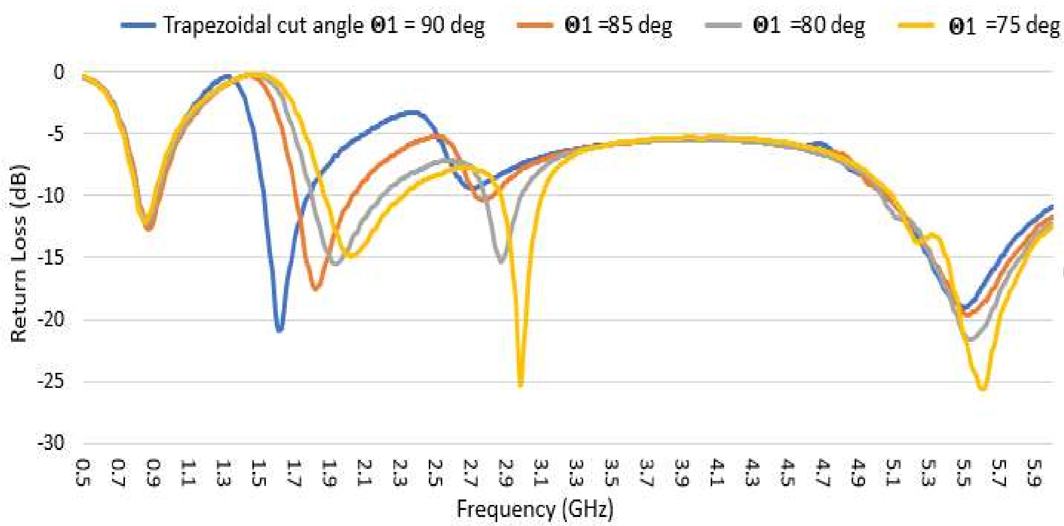

Figure 3.14 Return loss while sweeping the trapezoidal cut angle (ϴ1) in the short structure

On the other hand, the gap between the long and short structures controls the impedance between the low and high bands, giving decent rejection and high impedance at the GNSS frequency bands. For instance, for L1 GNSS frequency range 1.559 -1.61 GHz, the return loss is 0.5 dB to 1 dB, providing 9.6 dB to 6.8 dB extra rejection for cellular noise into the GNSS Band.

Finally, with the optimization for the radiation pattern, the return loss was not improved, so a matching circuit was used to compensate and provide a good 50 matching across the frequency range. Figure 3.15 illustrates the matching circuit, introduced to the feeding point where the antenna is connected to the horizontal PCB on the baseplate shown in Figure 3.16b; the matching circuit extends the impedance match down to 617 MHz and improves the return loss for the frequency range from 3.3 GHz to 5 GHz.

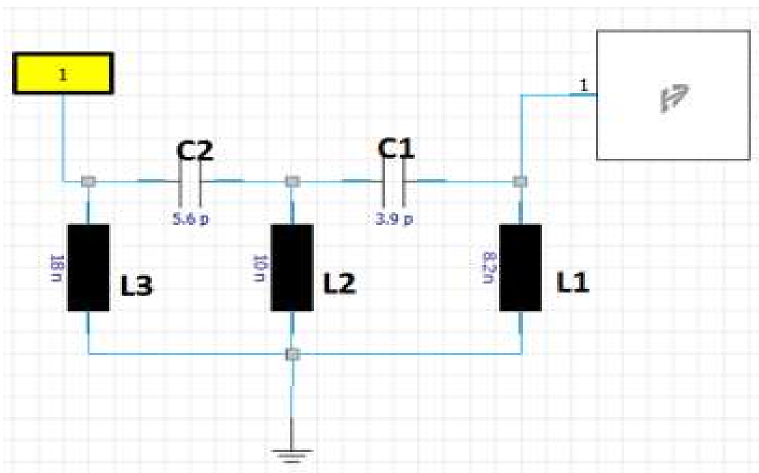

Comp	Value
C1	3.9pF
C2	5.6pF
L1	8.2nH
L2	10nH
L3	18nH

Figure 3.15. Antenna matching circuit and component values

3.6 Results

3.6.1. Antenna Evaluation Setup

The antenna was fabricated on FR-4 using a PCB milling machine, as shown in Figure (3.16-a). Both top and bottom layers were connected using four vias soldered at the feed point. The overall structure was mounted on a horizontal PCB with the matching circuit populated. The horizontal PCB is connected to a metal baseplate of 8mm height to mimic the shark-fin environment, as shown in Figure (3.16-b).

The prototype antenna was measured in a far-field anechoic chamber with an inner dimension of 13×4×4 m^3, The AUT gain was calculated using the gain substitution method relative to standard antennas.

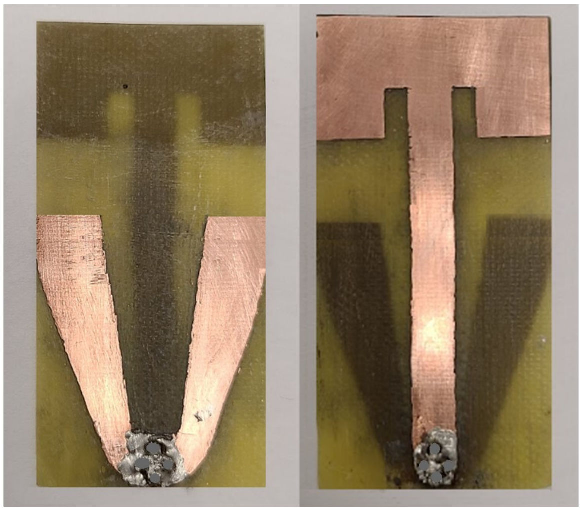

Bottom Layer Top Layer

(a)

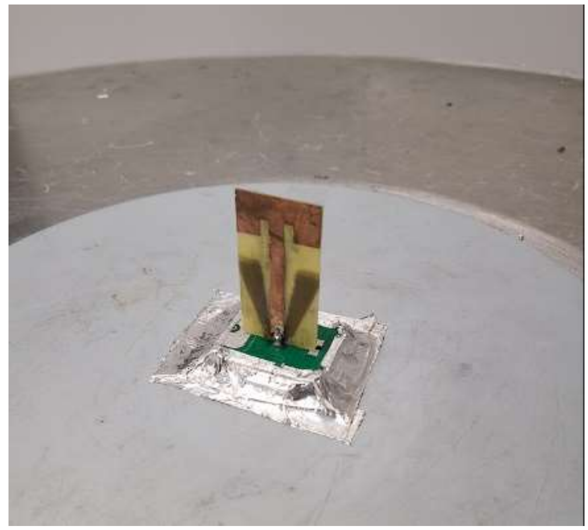

(b)

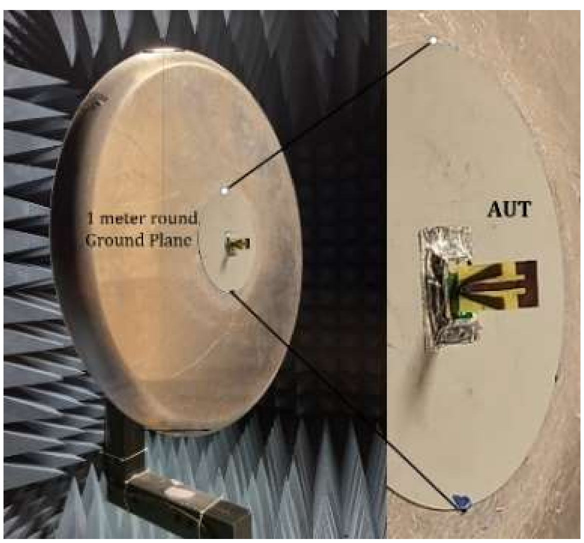

(c)

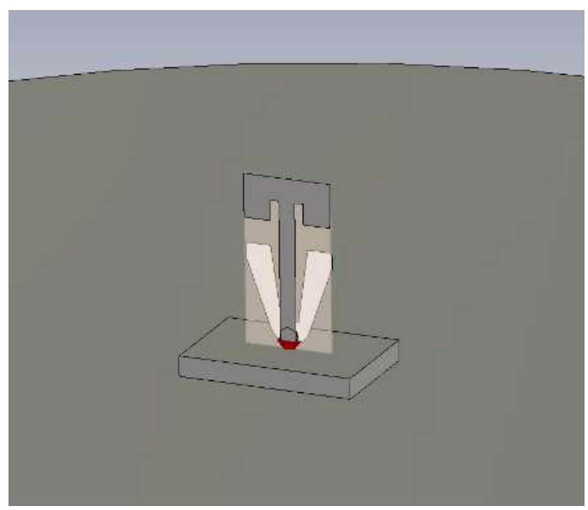

(d)

Figure 3.16. a) Fabricated antenna b) Antenna prototype. c) Antenna measurement setup d) Simulation model

The AUT was evaluated on a 1-meter ground plane, as shown in Figure (3.16-c). The 1-meter ground plane is a typical setup to assess an automotive antenna element despite the different vehicle roof shapes, tilt, and sizes. The antenna was simulated using CST time-domain solver software [40] with the same setup as the prototype is shown in Figure (3.16-d).

All simulation and measurement data were collected for the full sphere with a resolution of 5 degrees in azimuth and 5 degrees in elevation. And for three frequency ranges; low band 0.617 -0.96 GHz in a 20 MHz frequency step, high band 1.71-2.7 GHz in a 50 MHz step, and ultra-high band 3.3-5 GHz with a step of 75 MHz.

3.6.2. VSWR and efficiency

The S-parameters of the simulating results, including the matching circuit, were collected. The prototyped antenna was also measured with a similar setup at the feeding point, and the same matching circuit was applied. Both simulated and measured results are plotted in Figure 3.17.

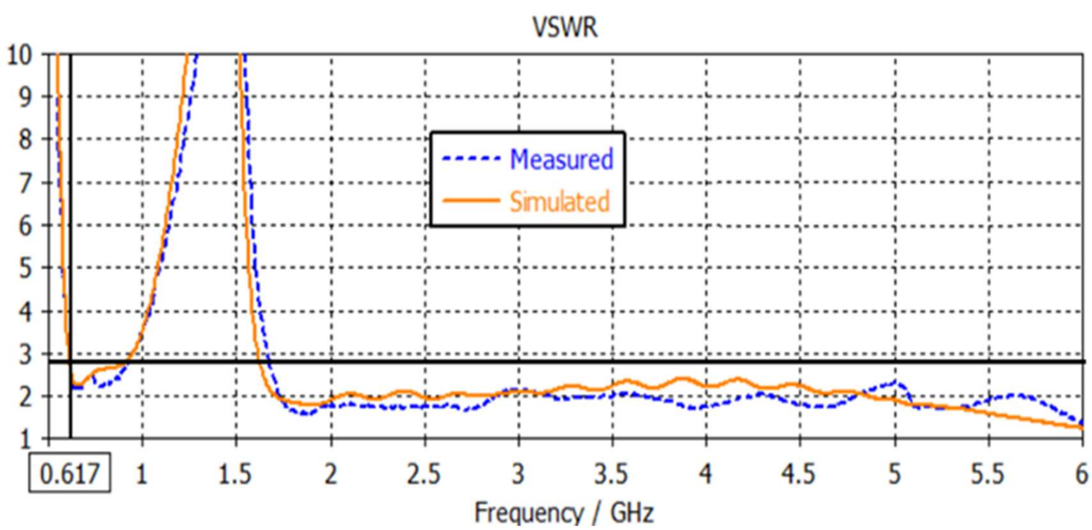

Figure 3.17. Comparison of measured and simulated VSWR

As a result of this matching circuit the VSWR was below 2.7:1 for the low-frequency range 617 - 960 MHz and 2.5:1 for frequencies 1.71 - 5 GHz.

Antenna total efficiency data was collected from simulation software and measurement data, as shown in Figure 3.18. In both cases, the efficiency values include the matching circuit and mismatch loss. Measurement data has a slightly lower average efficiency of around 5% compared to the simulation data, probably due to a non-ideal matching circuit and actual PCB material loss on the prototype; overall, the trend between simulation and measurement matches. Measurement data show more fluctuation over frequency, especially at lower frequencies, possibly due to measurement accuracy in the chamber. Measurement efficiency for low, high, and ultra-high bands are 70%, 85%, and 79%, respectively.

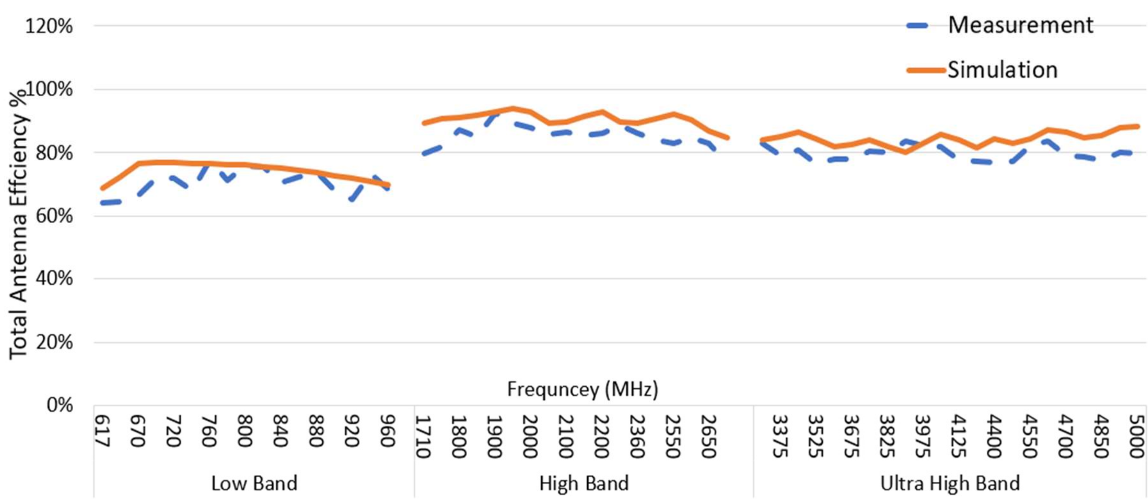

Figure 3.18. AUT total efficiency for prototype measurement and simulation

3.6.3. Radiation Pattern Analysis

The main goal of the proposed antenna design is to provide an improved radiation pattern which is omnidirectional and has a high gain at lower elevations. This can be achieved by maintaining the intrinsic monopole first-order mode radiation pattern across the new 5G cellular frequency ranges.

The 2D radiation pattern for the simulated realized gain compared to the prototype measurements at different frequency points is shown in Figure 3.19. The elevation plane radiation pattern at $\phi=90^\circ$ for the frequencies 0.84 GHz, 1.9 GHz, 2.6 GHz, 3.9 GHz, and 4.7 GHz are shown in Figures (3.19-a, c, e, g, and i), respectively. Both measurement and simulation have a good match.

The radiation pattern is generally focused toward the elevation of the interest area shaded in red (theta=[60-90] degrees). Since the antenna was simulated/measured on a finite 1-meter ground plane, peak gain tends to move lower elevations as the frequency gets higher due to the relatively larger electrical size of the ground plane. At 0.840 GHz, the peak gain was 2.7 dBi at theta 50 degrees; however, the beam is broad and covers the in-tended elevation zone very well. At the mid-frequency ranges 1.9, 2.6, and 3.9 GHz, the beam is very well set in the intended elevation range with a peak gain of 5dBi. At 4.7 GHz, the pattern starts to have a second beam at higher elevations due to the influence of higher-order Mode 6 described in section 2.2. The main lower beam gets narrower but still effectively covers the intended range with a peak gain of 4.5 dBi.

Figure 3.19. 2D Radiation pattern

0.84 GHz

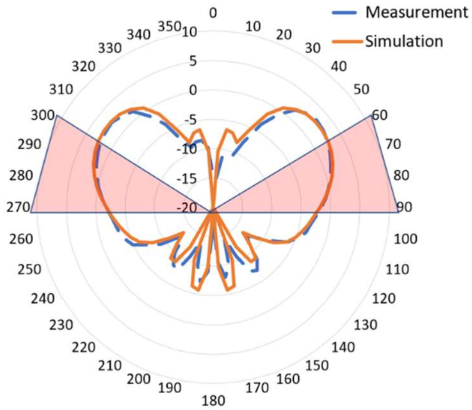

(a)

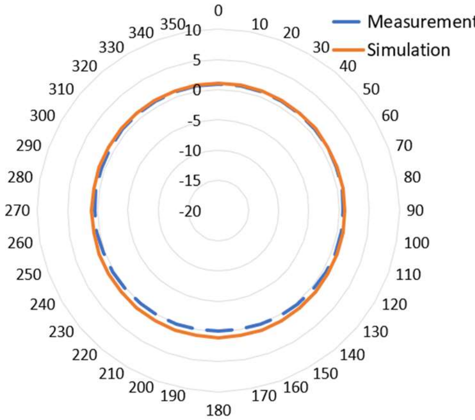

(b)

1.9 GHz

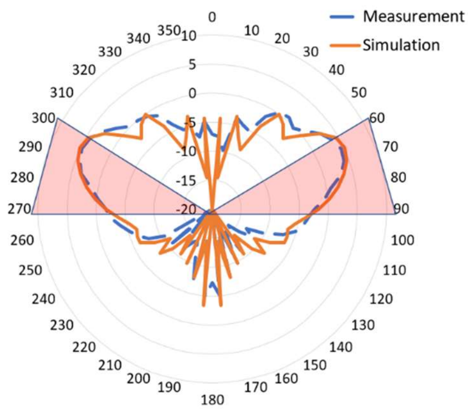

(c)

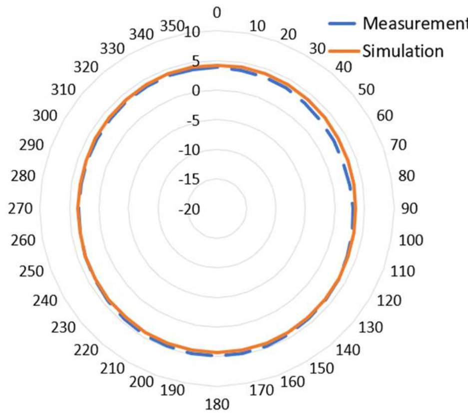

(d)

2.6 GHz

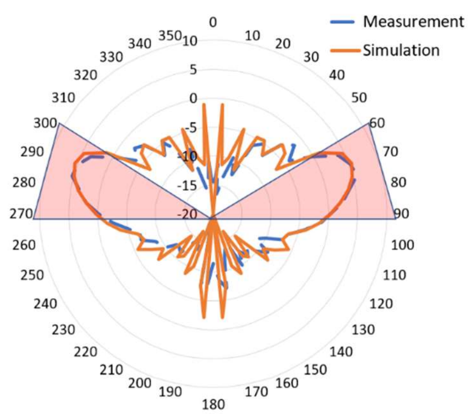

(e)

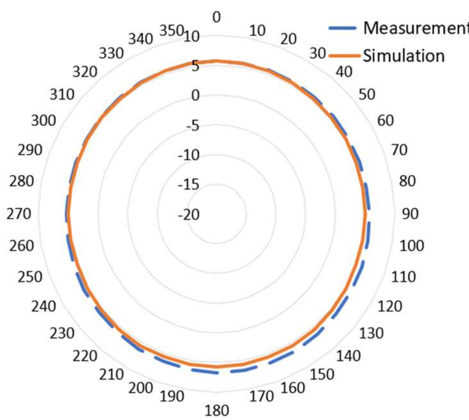

(f)

Figure 3.19 —Continued

3.9 GHz

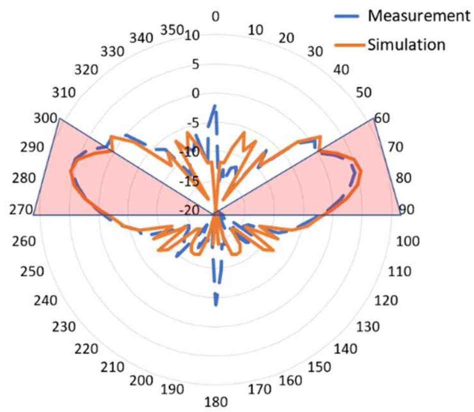

(g)

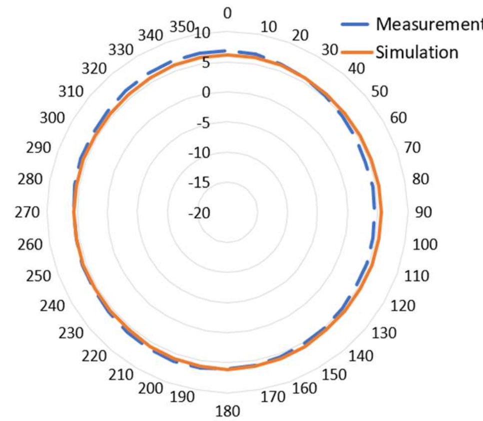

(h)

4.7 GHz

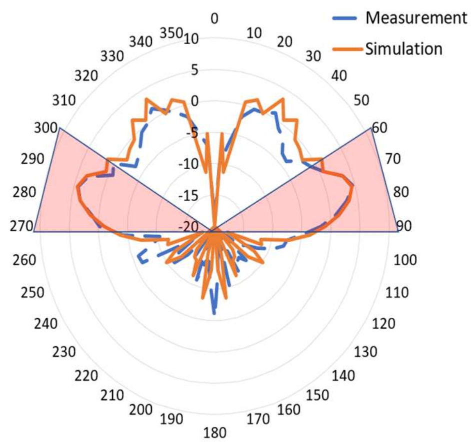

(i)

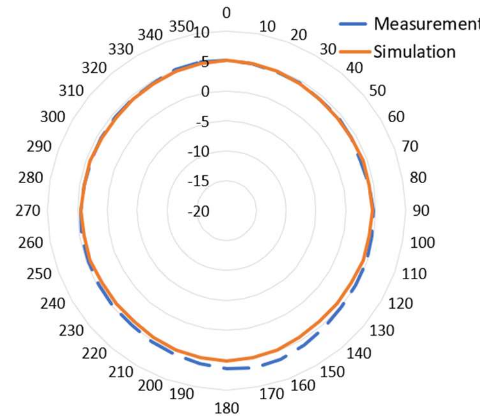

(j)

Figure 3.19. 2D Radiation pattern for

a) 0.84 GHz elevation plane (**ϕ**=90) **b)** 0.84 GHz azimuth plane (**Θ** =75)

c) 1.9 GHz elevation plane (**ϕ** = 90) **d)** 1.9 GHz azimuth plane (**Θ** =75)

e) 2.6 GHz elevation plane (**ϕ** =90) **f)** 2.6 GHz azimuth plane (**Θ** =75)

g) 3.9 GHz elevation plane (**ϕ** =90) **h)** 3.9 GHz azimuth plane (**Θ** =75)

i) 4.7 GHz elevation plane (**ϕ** =90) **j)** 4.7 GHz azimuth plane (**Θ** =75)

The azimuth plane radiation pattern at Θ=75∘ for the frequencies 0.84 GHz, 1.9 GHz, 2.6 GHz, 3.9 GHz, and 4.7 GHz are shown in Figures (3.19-b, d, f, h, and j), respectively. The measurement results exhibit excellent omnidirectionality throughout the operational frequency bandwidth and a good match to simulation data with a slight drift due to an imperfect prototype build and measurement accuracy. As the frequency grows higher, the radiation pattern shape tends to be slightly elliptical because of the higher-order mode.

The primary automotive antenna performance metric is the LAG at specified elevation angles. The LAG for theta = [60-90] degrees was calculated by the equation described in Chapter 1, section 2, at each frequency point and plotted in Figure 3.20.

Results show a consistent and flat gain across frequency and a similar gain for measurement and simulation. The low band average LAG is between 0 dBi and 0.9 dBi. The high-frequency band's average LAG is between 2 dBi and 3.5 dBi. Finally, the average LAG for ultra-high bands is between 1.4 dBi and 2.8 dBi.

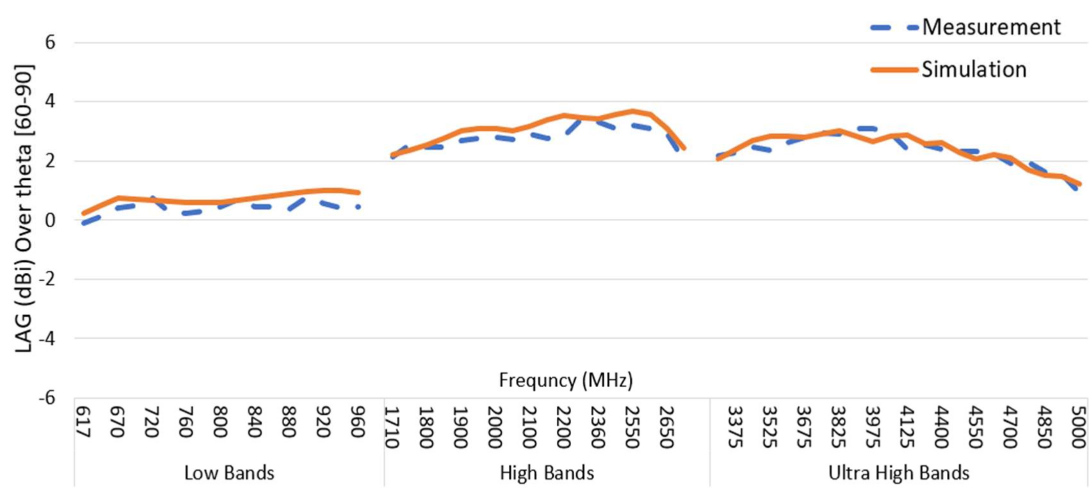

Figure 3.20: AUT Linear Average gain for elevation zone theta [60-90] across the frequency range for prototype measurement and simulation data

Similarly, to illustrate the omnidirectionality across the operating frequency range, the average STD for theta = [60-90 degrees] was calculated by equation 5 and is shown in Figure 3.21. Again, the trend for both the measured and simulated antenna shows a good correlation. Measurement data is 0.5 dB higher on average due to measurement accuracy. In the ultra-high band, the STD slightly ramps up as the azimuth pattern tends to an elliptical shape, as discussed in section 3.3 for the azimuth plane plots.

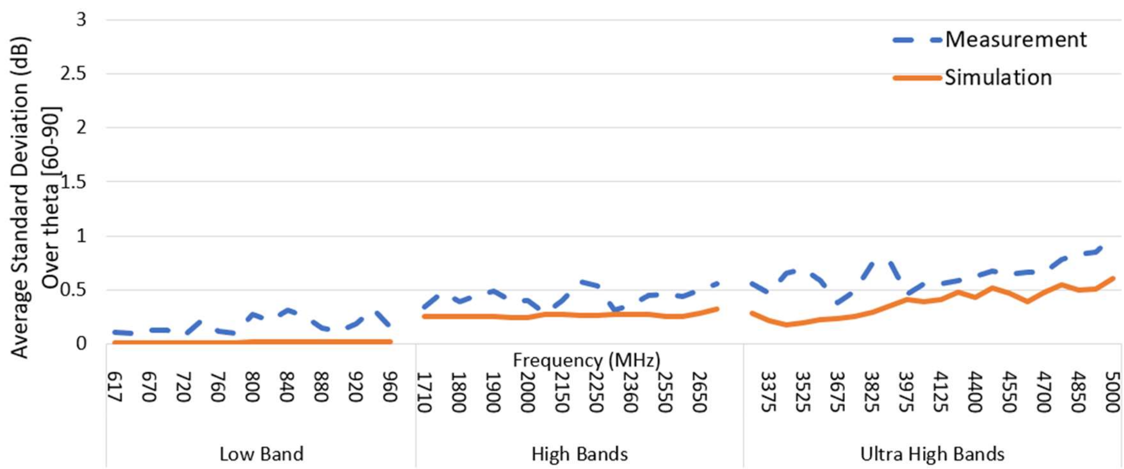

Figure 3.21: AUT average standard deviation for elevation zone theta [60-90] across the frequency range for prototype measurement and simulation data

Statistical figures 3.20 and 3.21 provide the best summary of the antenna performance across the frequency range and also over the intended elevation; the LAG shows that the average gain characteristic is flat over the frequency range, and the STD shows that the radiation pattern is perfectly round, which best achieve the radiation requirement for automotive antenna.

CHAPTER FOUR

MULTI-FUNCTIONAL ANTENNA FOR 5G AND GNSS

Wireless services for modern automobiles, including wireless local area network 5G cellular and legacy cellular technologies, V2x, Global Positioning System (GPS), SDARS, Bluetooth, Wi-Fi, and broadcast services such as AM, FM, DAB; vehicles need to be equipped with more antennas packed into a constrained space to keep the good exterior shape and mechanical stability.

A common implementation for an antenna system is to package all antenna services in one part to simplify the vehicle manufacturing process. Multiple antenna elements are used inside the package; one antenna element for each wireless service allows an Ideal radiation characteristics. However, when various antennas coexist in one package, a complication arises in the interoperation of those services and achieving adequate inter-isolation and filtration between the antennas because of the crucial part of the design and extra effort and spacing between the antennas.

Consolidating antennas in a single structure to implement multiple services that simultaneously or switch between different modes of operation. While multi-band antennas would extend the frequency range to cover multiple antenna services, they usually have similar radiation patterns and polarization. This chapter will illustrate antenna design combining two different antenna functions, GNSS and 5G cellular, each with different polarization and radiation pattern requirements.

4.1 GNSS and cellular requirement:

The fundamental wireless functionalities in automobiles are navigation services, which mainly rely on global satellite positioning systems, and cellular services that offer high-speed data access and facilitate information exchange for various purposes. Furthermore, the coexistence of GNSS and cellular technologies would offer additional services like vehicle tracking, fleet management, and enhanced safety and security features.

Vehicle cellular communication requires a linearly polarized antenna with an omnidirectional radiation pattern. For automotive, the antenna's gain must be maximized close to the horizon at theta angles between 60 and 90 degrees to ensure a good communication range when the vehicle is far from the cell tower, as illustrated in Figure 4.1. The 5G-sub 6 GHz frequency bands covering 5G and the legacy technologies reside in the frequency bands 617-960 MHz, 1710 – 2690 MHz, or 3300 – 5000 MHz, which correspond to the low band, the high band, and the ultra-high band, respectively.

Optimal GNSS performance requires a wide beam unidirectional pattern with right-hand circular polarization (RHCP), the pattern boresight orientation should be towards the zenith to receive satellite ranging signals, as depicted in the radiation pattern in Figure 4.1. The GNSS L1 frequency bands consist of Beidue (1559-1563 MHz), GPS (1574-1576 MHz), and Glonass (1597-1606 MHz).

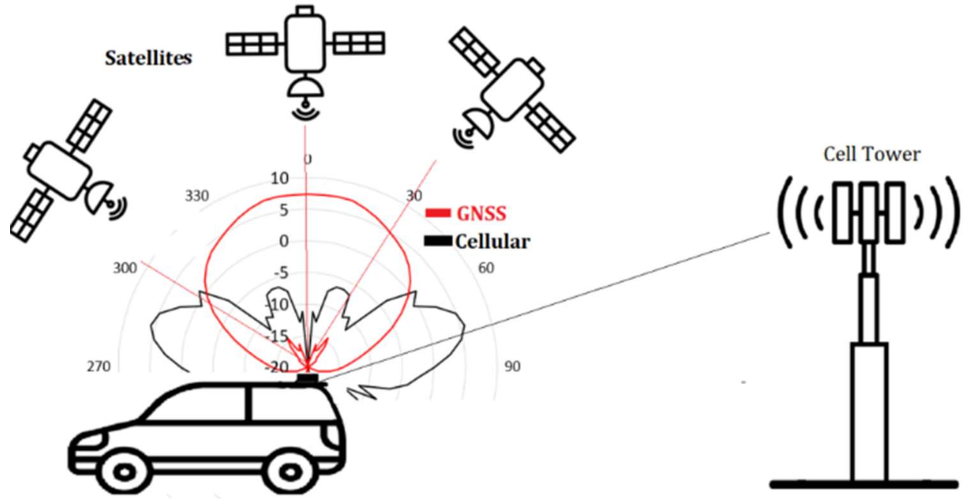

Figure 4.1. Vehicular Dual-function antenna radiation pattern requirement for GNSS (red) and Cellular (black)

Typical antenna system implementation uses two separate antennas, one for GNSS and one for cellular function. GNSS usually uses a ceramic patch antenna packaged with the cellular element. Table 1 compares the work in this chapter work and antennas in the literature on GNSS and cellular functions in the same package. [18] uses a single structure but employs a monopole, which doesn't align with GNSS requirements due to its omnidirectional, linear polarization and low gain at the zenith. Both [22] and [23] use two separate antennas for GNSS and 5G cellular, offering good performance but nearly double the size of our proposed design. Meanwhile, [24] and [25] employ two separate antenna designs with smaller sizes and acceptable performance. Still, it only covers a very narrow band for GPS and cellular, which doesn't meet the required 5G connectivity for automotive. Our proposed multi-functional, single-structure design concepts achieve the needed performance while minimizing size, complexity, and cost.

Table 4.1: Comparison of this work to Antenna systems with GNSS and Cellular functions

Design Concept/size	GNSS L1 performance	5G Cellular performance
This work: **One Antenna** **multi-function** **Antenna** 5G cell and GNSS L1 **Size:** 75X50X30 mm^3	**Frequency**:1559-1606 MHz **VSWR** < 3:1 **Polarization**: RHCP **Radiation pattern**: Hemispherical **RHCP gain** at zenith = 5.2 dBc **Axial** ratio at zenith < 2 dB	**Frequency**: 0.62-0.96, 1.71-2.69, and 3.30-5.00 GHz. **VSWR**: < 3:1 **Polarization**: linear **Radiation pattern**: Omnidirectional **LAG** [theta=60-90]/freq: 0.8,1.8 and 2.2 dBi **Peak Gain** / freq: (3.9, 6.5, and 8.1) dBi
[18] **One Antenna** **Multi-band** **antenna** 5G cell and GNSS L1 **Size:** 70X37X17 mm^3	**Frequency**:1559-1606 MHz **VSWR** 2:1 **Polarization**: linear **Radiation pattern**: Omnidirectional **RHCP** gain at Zenith = -10 dBc **Axial ratio** at Zenith= N/A	**Frequency**: 0.62-0.96, 1.71-2.69 and 3.30-5.00 GHz. **VSWR**: 3.3:1 **Polarization**: linear **Radiation pattern**: Omnidirectional **LAG** [theta=75-90] (0.8, 2 and -1) dBi **Peak Gain** per freq range: N/A
[23] **Two** **Antennas.** **Side by side** 2X 5G cell and GNSS L1 **Size:** 230X55X28 mm^3	**Frequency**: 1559-1606 MHz **VSWR** 3.5:1 **Polarization**: RHCP **Radiation pattern**: Hemispherical **RHCP gain** at zenith = 4 dBc **Axial ratio** at zenith < 3 dB	**Frequency**: 0.62-0.96, 1.71-2.69 and 3.30-5.00 GHz. **VSWR** 3.3:1 **Radiation pattern**: Omnidirectional **Polarization**: linear **LAG** [theta=75-90]: (-2.1, 0.6, and 3.1)dBi **Peak Gain** per freq range: N/A

Table 4.1 ---Continued

[22] **Two Antennas Stacked** 5G Cells and GNSS L1L5 **Size**: 250X100X70 mm^3	**Freq**:1160-1190, 1560-1610 MHz **VSWR** 2:1 **Polarization**: RHCP **Radiation pattern**: Hemispherical **RHCP gain** at zenith = 1.5, 1 dBc **Axial ratio** at zenith < 3 dB.	**Frequency**: 0.45-0.47, 0.82-0.96, 1.71-2.69, 5.20-5.70GHz **VSWR** 2:1 **Radiation pattern**: Omnidirectional **Polarization**: linear **LAG** per freq range: N/A **Peak Gain**/ freq range = (0, 4, 6.4 and 9) dBi.
[24] **Two Stacked Antenna** Narrowband cell (GSM900 and DCS1900) and GPS **Size:** 60X60X12 mm^3	**Frequency**: 1575+-1.23 MHz **VSWR** 2:1 **Polarization**: RHCP **Radiation pattern**: Hemispherical **RHCP gain** at zenith = 4 dBc **Axial ratio** at zenith < 3 dB	**Frequency**:0.89-0.96, 1.71-1.88 GHz VSWR 2:1 **Radiation pattern**: Omnidirectional **Polarization**: linear **LAG** per freq range: N/A **Peak gain** per freq range: (-2, -1) dBi (from the plot)
[25] **Two Antenna Side by side** Narrowband cell (3G DCS1800,IMT) and GPS **Size:** 80X80X6 mm^3	**Frequency**:1575+-1.23 MHz **VSWR** 3:1 **Polarization**: RHCP **Radiation pattern**: Hemispherical **RHCP gain** at zenith = -1 dBc **Axial ratio** at zenith < 2.7 dB	**Frequency**: 1.71-1.88, 2.50-2.69 GHz **VSWR** 2:1 **Radiation pattern**: Omnidirectional **Polarization**: linear **LAG** per freq range: N/A **Peak gain** per freq range:1.8 dBi, 4 dBi

4.2 Proposed Antenna Design

The proposed design idea involves merging two basic antenna geometries into a unified structure, enabling the antenna to serve dual purposes. The flat plate with a U-slot cut is ideal for GNSS as it allows for circular polarization and hemispherical radiation pattern [59-63]. PIFA structure is known for omnidirectional and linear polarization, suitable for 5G cellular sub-6 GHz. These two antenna structures can be combined into one port, a single structure. CMA was employed to finely tune the combined structure and ensure the preservation of intrinsic geometry radiation modes and performance.

4.2.1 Antenna Design and Dimensions

The antenna's primary structure comprises a PIFA with a wideband center feed and a U-slot on top, as shown in Figure 4.2. The overall size is 75×50×30 mm3. The antenna was built with sheet metal and a 1 mm thick FR4 PCB in the center to serve as antenna feed and provide the necessary mechanical support for the structure.

Some of the main design features is the U-slot, shown in Figure 4.2 top view, which generates the required mode for the GNSS radiation function. Also, it splits the top plate into the outer and inner areas, providing dual-band operation for cellular, low band 0.62-0.96 GHz, and higher bands in 1.71 -5.00 GHz.

Furthermore, the PCB structure can be seen in the Figure 4.2 side view. It shows a wide band feed to provide the necessary bandwidth for cellular to operate up to 5GHz. Finally, the PIFA shorting plate -shown in Figure 4.2 front view- is essential for the PIFA to have a good input match at the low band. The shorting location was chosen to be in the corner, which also helps maintain the circular polarization at the GNSS frequency band.

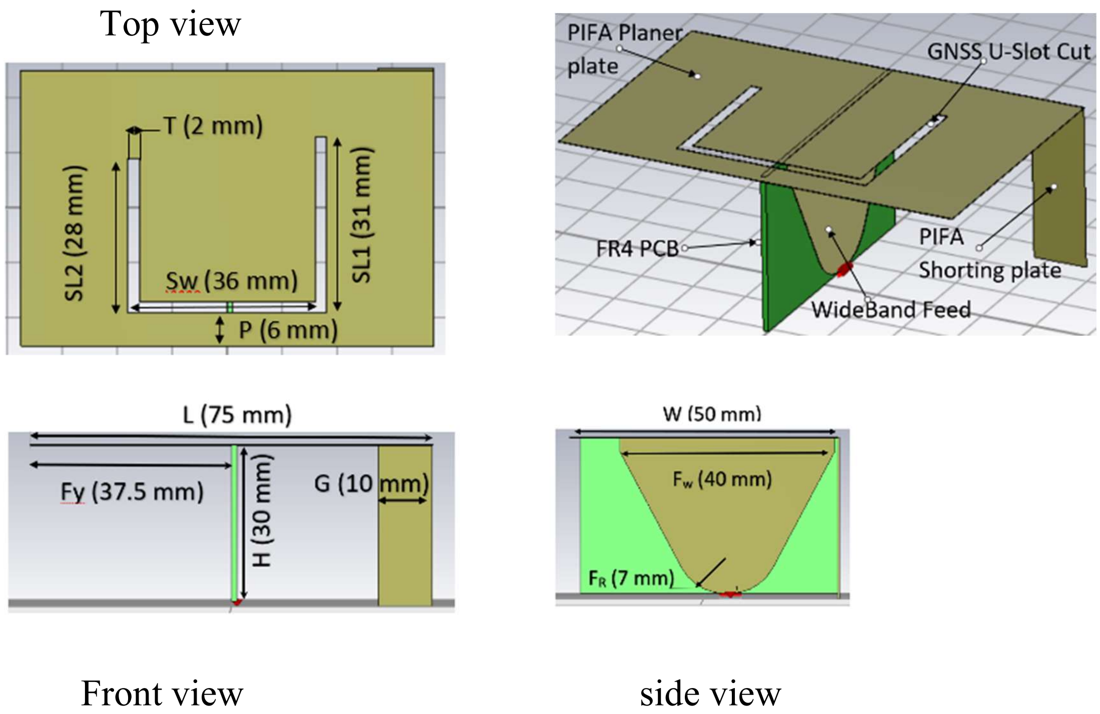

Figure 4.2: Proposed antenna model and dimensions

4.2.2 Characteristic mode analysis (CMA)

The CMA provides insight into possible radiation modes for a specific antenna geometry. Considering the distinct radiation patterns and polarization requirements for cellular and GNSS functions, these characteristic modes must be capable of meeting the performance requirements at each frequency range. Thus, leveraging CMA helps to focus on tuning those modes independently.

The proposed antenna structure was analyzed on an infinite ground plane using a commercial software tool CST [23] integral equation solver, and the results for the seven dominant radiation modes are shown in Figure 4.3 (a,b, and c) for modal characteristic angles, modal significance, and weighting modal coefficient (|WMC|), respectively.

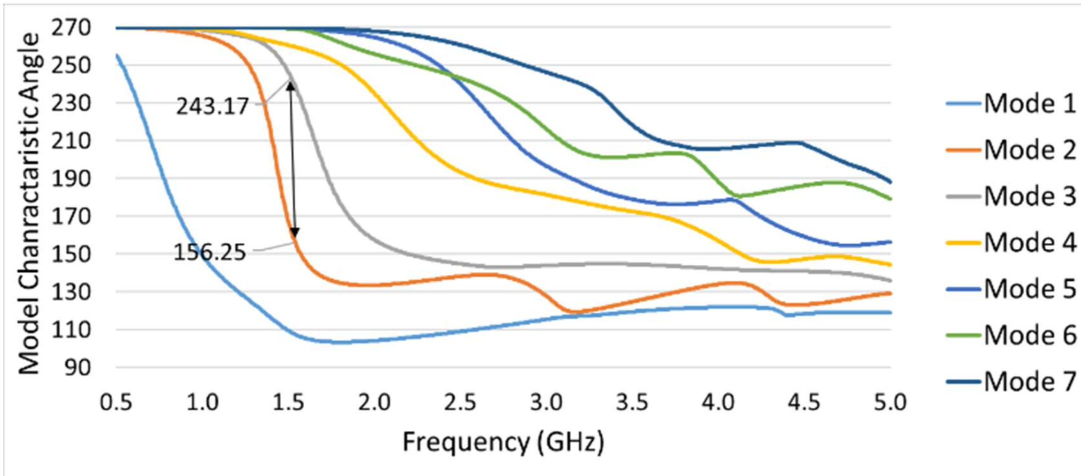

(a) Modal characteristic angle

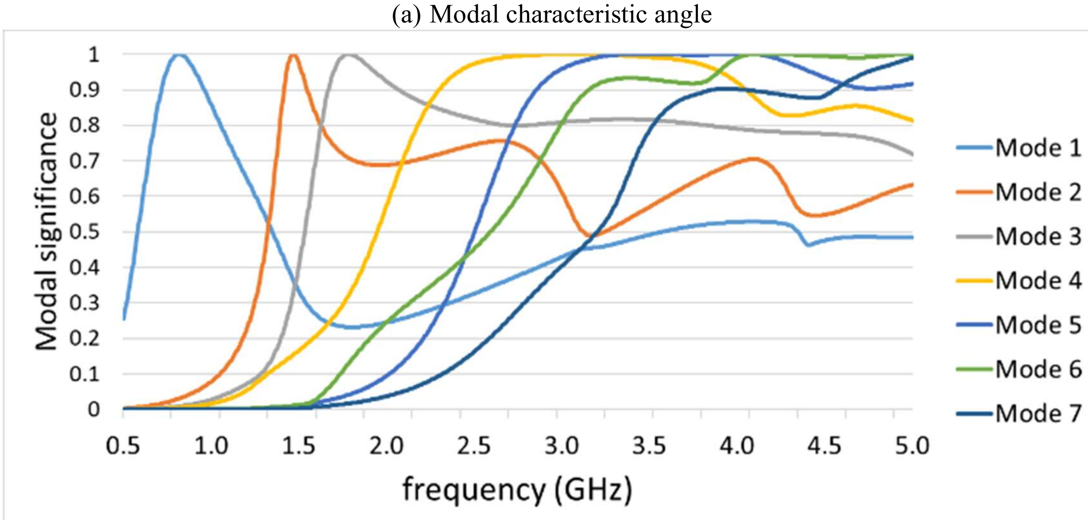

(b) Modal significance

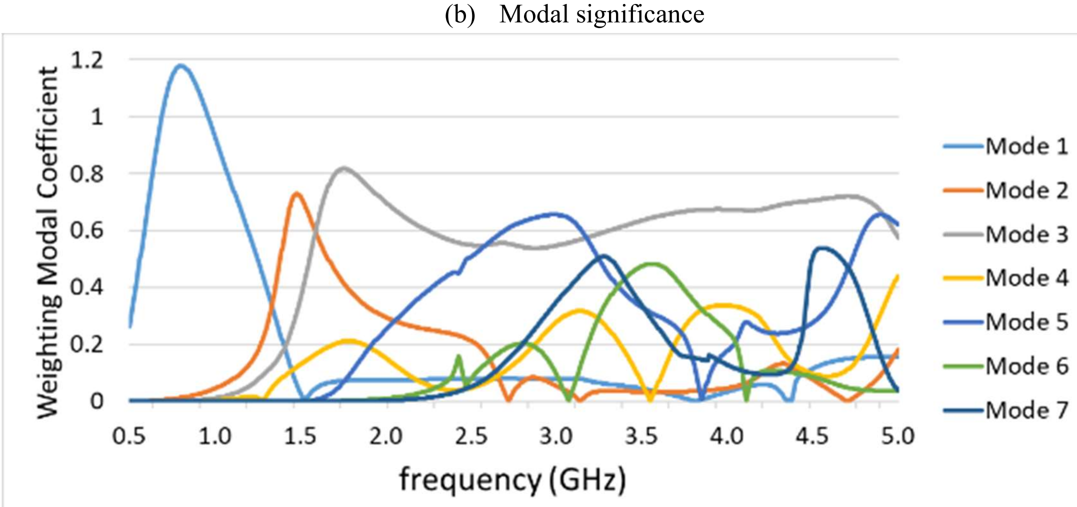

(c) Weighting modal coefficient.

Figure 4.3**:** Characteristic mode analysis for the proposed antenna structure

Mode 1 is the only significant mode for cellular' low band'. It resonates at 780 MHz and is intended to cover the frequency range from 617 to 960 MHz. The radiation pattern for Mode 1 is omnidirectional, as shown in Figure 4.4(a). the current flow is distributed over the feed, shorting plate, and the outer dimension for the top plate as shown in Figure 4.4(b). The total current path is approximately half the wavelength distance in quarter wavelength PIFA size, which is the known advantage of the PIFA with a shorting pin versus the patch antenna.

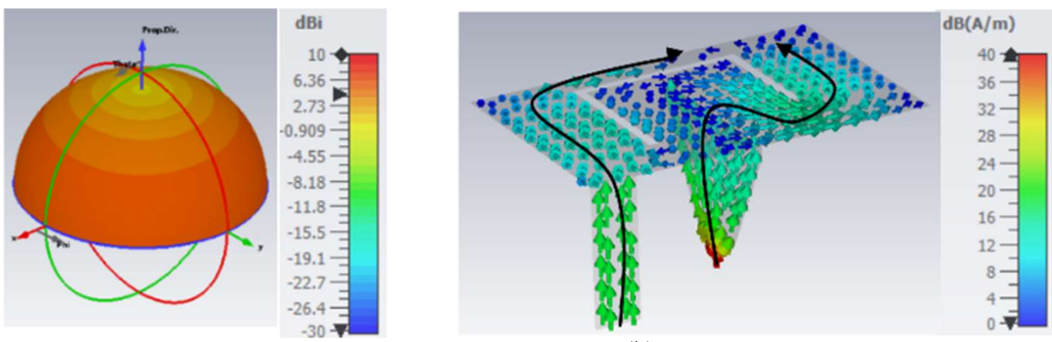

(a) (b)

Figure 4.4: Cellular low band modes Characteristics at 0.78 GHz a) Mode 1 radiation pattern. b) Mode 1 surface current.

At the GNSS frequency range, Mode 2 and Mode 3 have high modal significance values and resonance frequencies at 1.49 and 1.76 GHz, respectively. The modal significance curve intersects at the middle of the GNSS L1 frequency range. The radiation pattern for Mode 2 and Mode 3 at 1.58 GHz are directive with a maximum gain toward the zenith, as shown in Figure 4.5 (a, b), which is suitable to receive the GNSS satellite ranging signal.

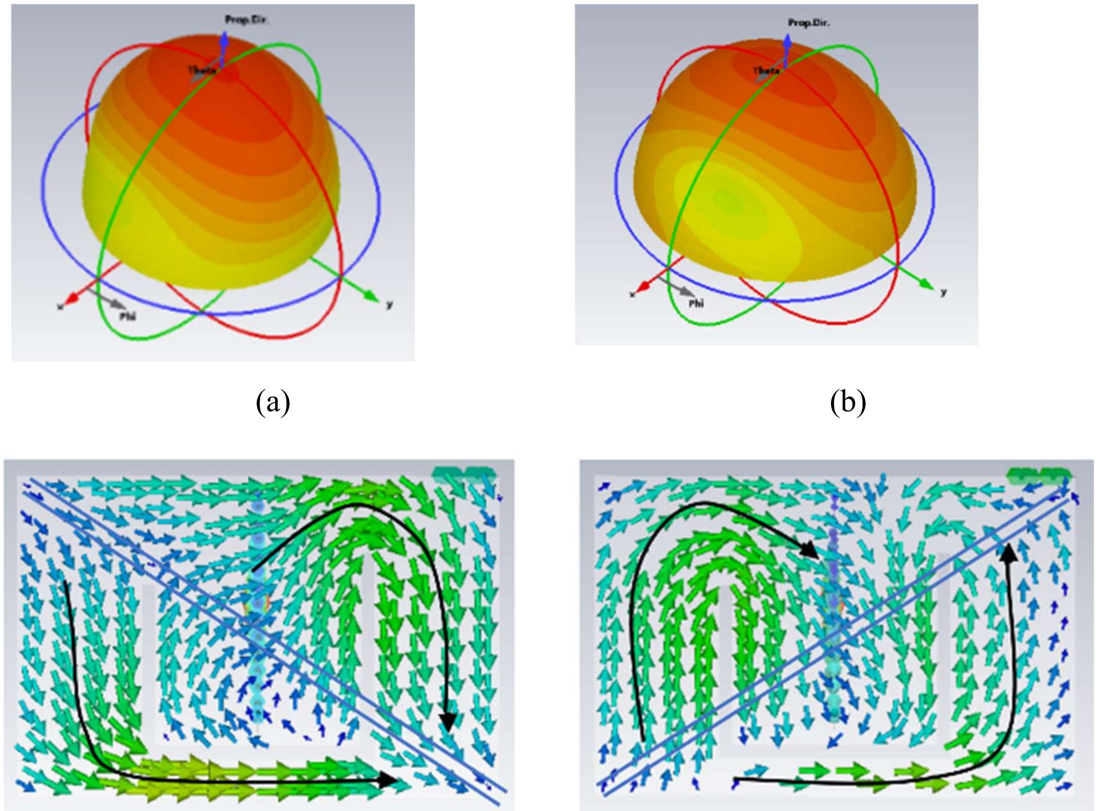

(a) (b)

(c) (d)

Figure 4.5: GNSS band characteristics modes at 1.58GHz a) Mode 2 Radiation pattern b) Mode 3 Radiation pattern c) Mode 2 surface current d) Mode 3 Surface current

Those modes need to be orthogonal and have a 90-degree phase shift to achieve right-hand circular polarization. Thus, by analyzing the surface current distribution shown in Figure 4.5 (c,d). Mode 2 and Mode 3 have very similar current distributions but at adjacent corners of the plate, making them primarily orthogonal. The phase difference can be found from a characteristic angle for each mode Figure 4.3(a); Mode 2 leads Mode 3 by 87 degrees.

In the cellular 'high band' and 'ultra-high band', Mode 3 dominates with high |WMC| across the bands in the frequency range of 1.71-5.00 GHz, as shown in Figure

4.3(c). The broadband feed structure is the primary geometry; however, due to different current distribution possibilities on the top plate with USlot and shorting plate, higher-order modes would be introduced, influencing the overall radiation pattern. Figure 4.6 and Figure 4.7 illustrate the mode radiation pattern and current distribution for the high band and ultra-high bands, respectively.

(a) Mode 3 at 2 GHz

(b) Mode 4 at 2 GHz

(c) Mode 5 at 2 GHz

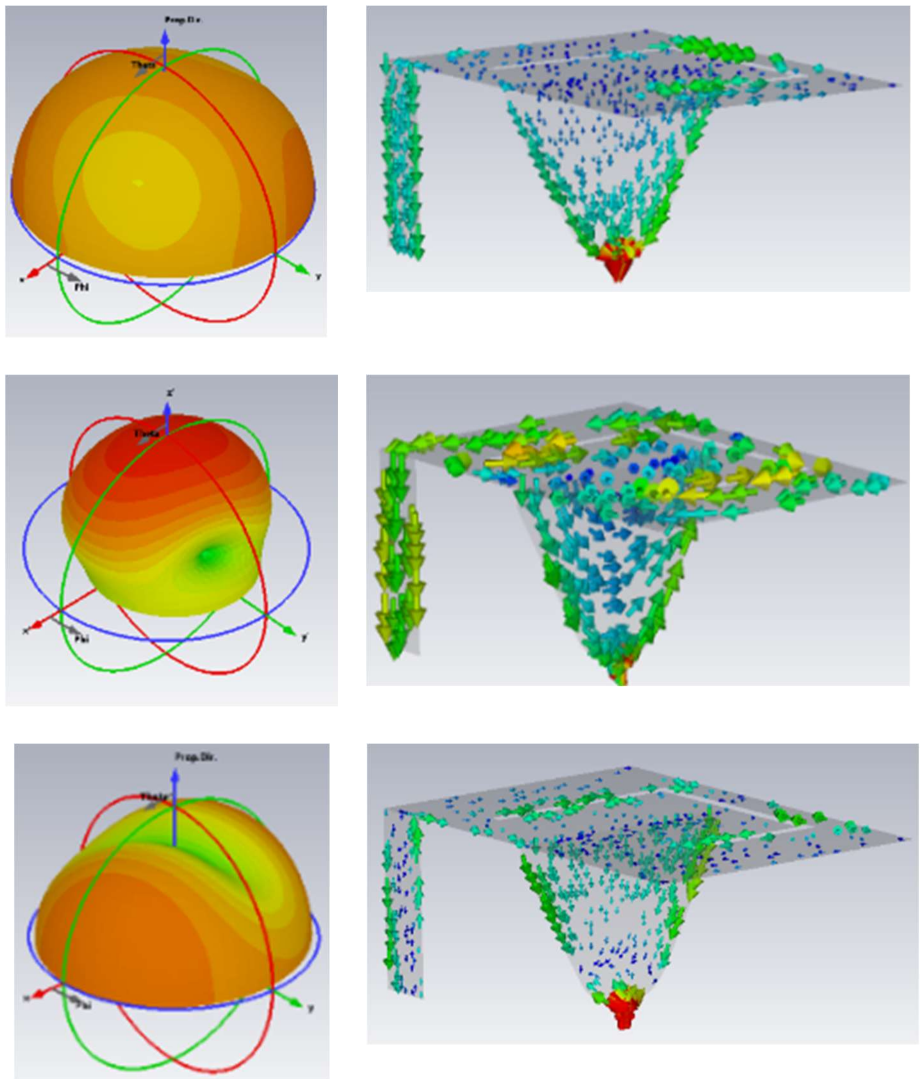

Figure 4.6: Characteristic modes radiation pattern and surface current for cellular high band at 2 GHz

(a) Mode 3
at 3.6 GHz

(b) Mode 6
at 3.6 GHz

(c) Mode 7
at 3.6 GHz

Scale

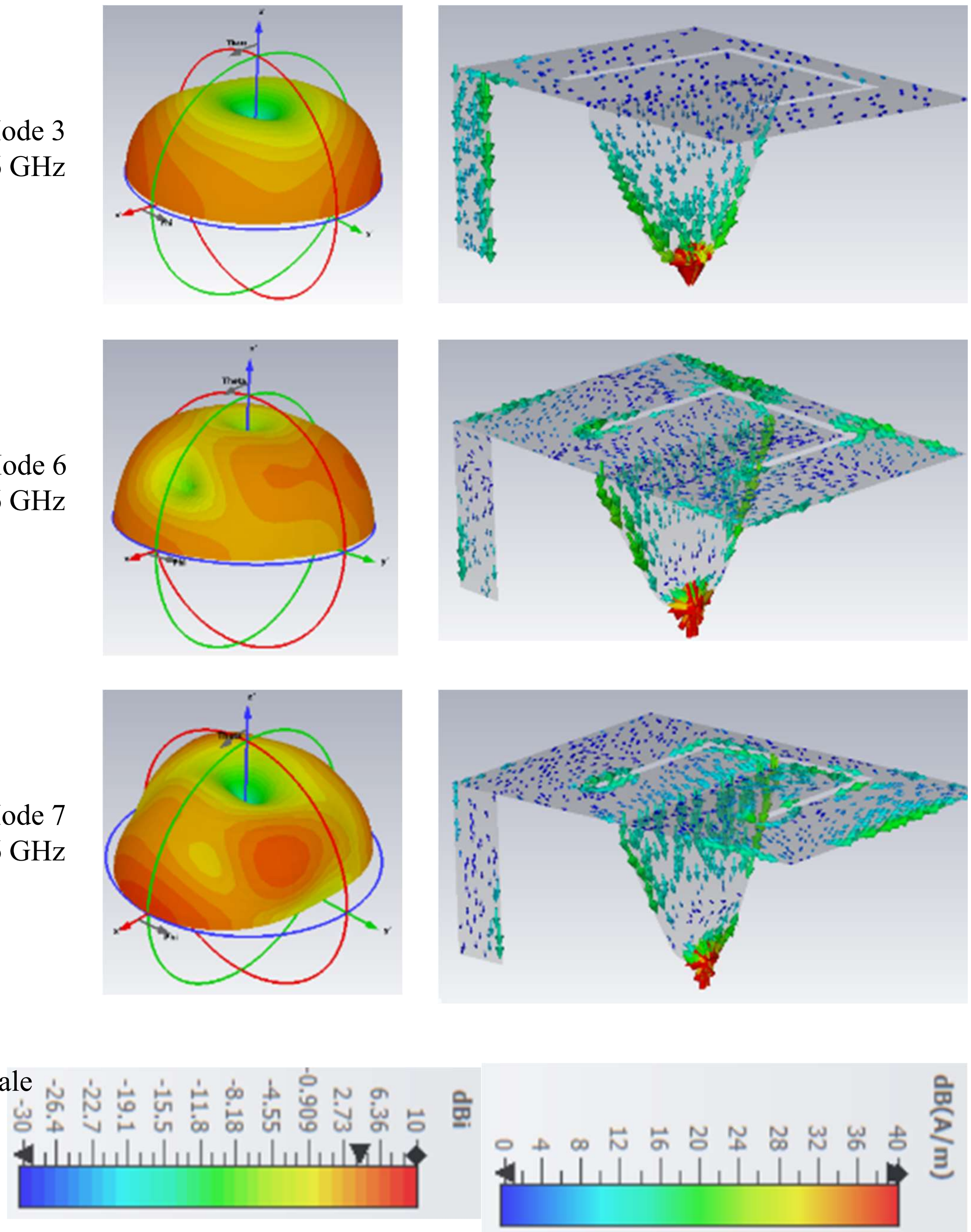

Figure 4.7: characteristic modes radiation pattern and surface current for cellular ultra-high bands at 3.6 GHz

In the 'high band,' the Mode 3 radiation pattern tends to cover lower elevation post-resonance. When combined with Mode 5, these modes generate an excellent omnidirectional radiation pattern for the rest of the high bands. On the other hand, Mode 4 has a low |WMC| because the surface current distribution travels horizontally on the feed line, as illustrated in Figure 4.6. In the 'ultra-high band,' Mode 3 continues to have an excellent omnidirectional radiation pattern. However, the overall radiation pattern is combined with higher order modes (Mode 5, 6, and 7), as shown in Figure 4.7, which affects the overall pattern.

In summary, because of characteristics modes arrangement over the frequency spectrum, the total gain radiation pattern using full-wave simulation over the frequency range is shown in Figure 4.8.

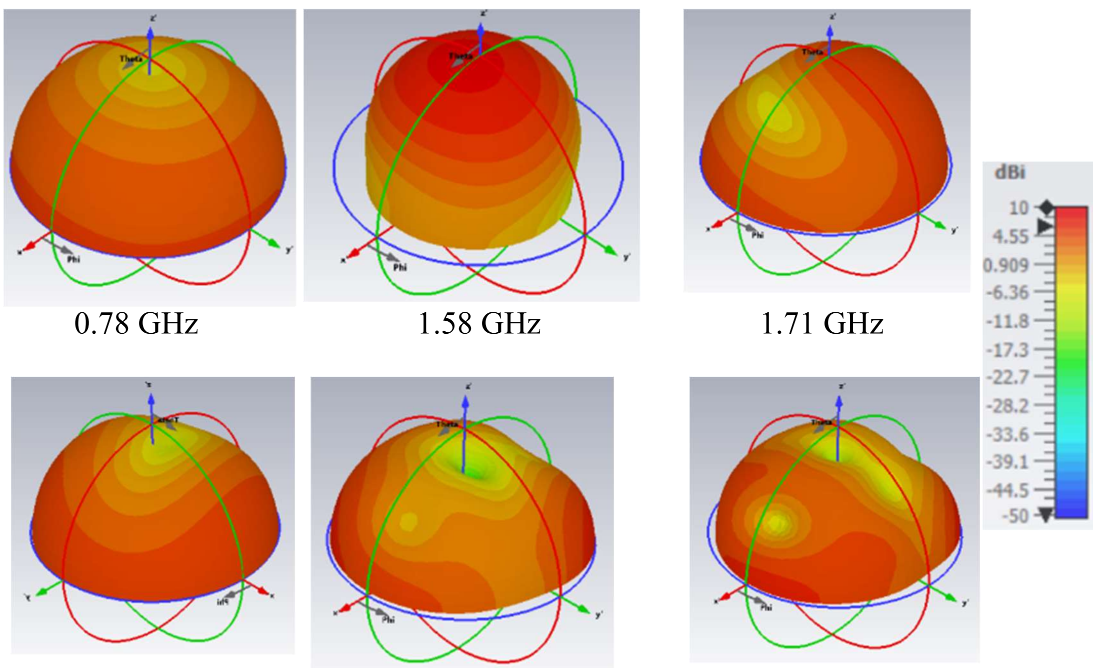

0.78 GHz 1.58 GHz 1.71 GHz

2.70 GHz 4.20 GHz 5.00 GHz

Figure 4.8: Total realized gain radiation pattern for the proposed antenna on an infinite ground plane at a different frequency

First, the antenna has an omnidirectional theta-polarized radiation pattern in the 'low band' 617-960 MHz. Then, the antenna becomes unidirectional with boresight toward the zenith at 1.58 GHz in the GNSS band. After that, the radiation pattern moves from directional to omnidirectional at 1.71 GHz and becomes suitable for cellular functionality with a high gain at low elevation angles for the rest of the high band up to 2.69 GHz. Finally, in the 'ultra-high band' 3.30-5.00 GHz, the antenna exhibits omnidirectional radiation, but the directionality is slightly affected by higher-order modes.

4.2.3 Parametric Study using (CMA)

The |WMC| for the most significant modes was monitored while changing the structure's main dimensions. First, the outer dimensions of the structure's width (W), Length (L), and Height (H) were studied in Figure 4.9 (a, b, and c). Each dimension was swept in 5 mm steps, and the solid line shows the selected design value. As the width (W) increases, there is a slight downshift in resonance frequency for Mode 1 and Mode 2 and no significant change in the resonant frequency for the higher-frequency modes. Changing the structure length (L) has a noticeable effect on the |WMC| value for Mode 2 and Mode 3; this directly affects the GNSS radiation pattern, circular polarization, and the start of the high cellular band. Lastly, as the antenna height (H) increases, all modes shift to lower frequencies, and Mode 3 has higher |WMC| at 'ultra-high bands.'

Figure 4.9: Weighting modal coefficient while changing the structure dimension.

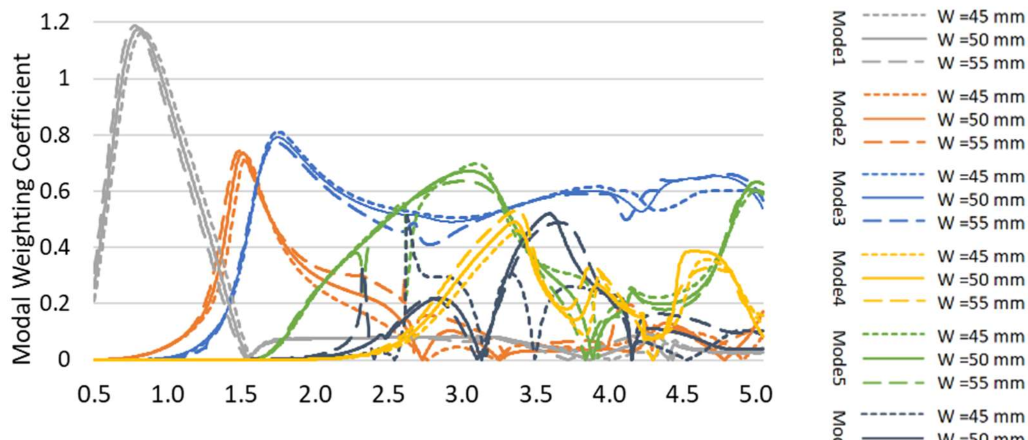

(a) Sweep outer dimensions width (W)

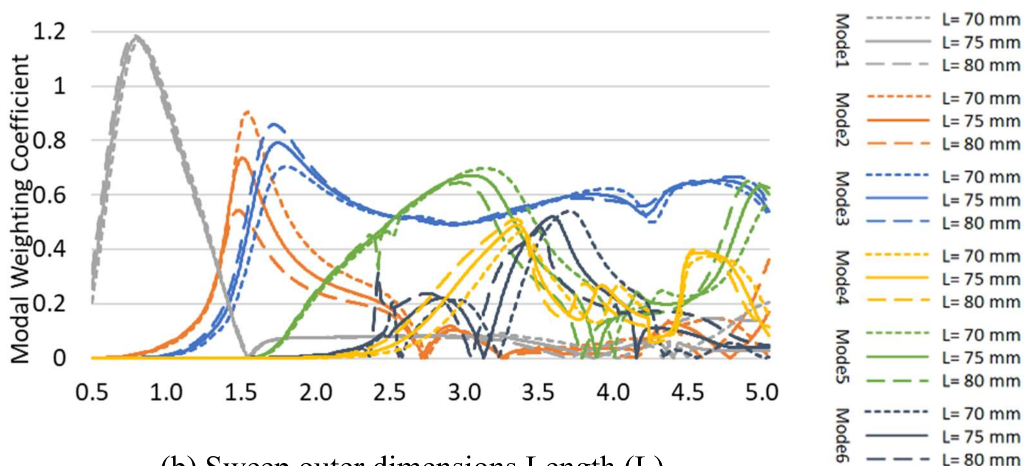

(b) Sweep outer dimensions Length (L)

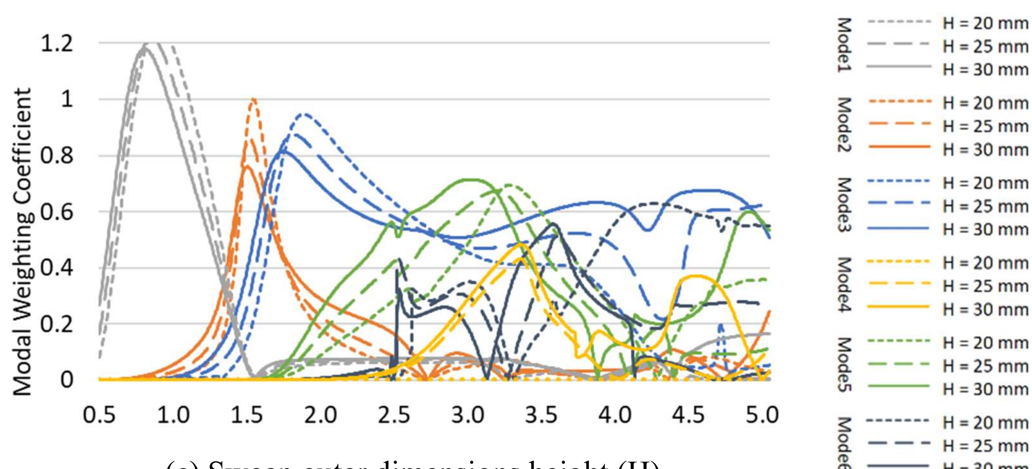

(c) Sweep outer dimensions height (H)

Figure 4.9—Continued

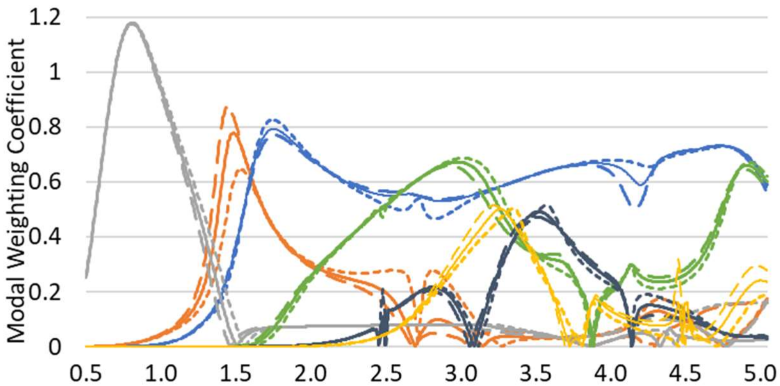

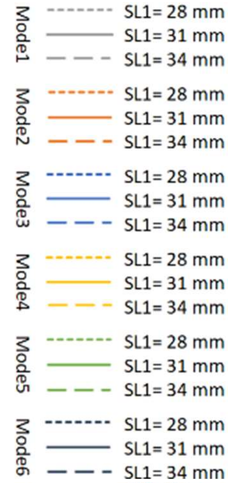

(d) Sweep U-slot long branch (SL1)

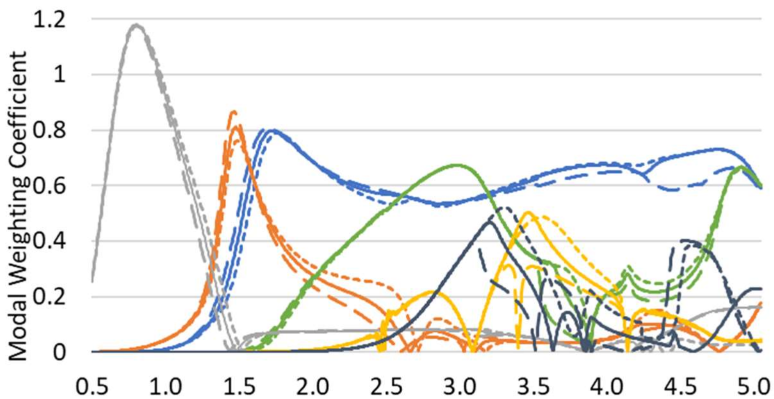

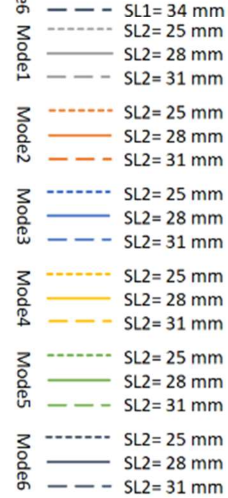

(e) Sweep U-slot short branch (SL2)

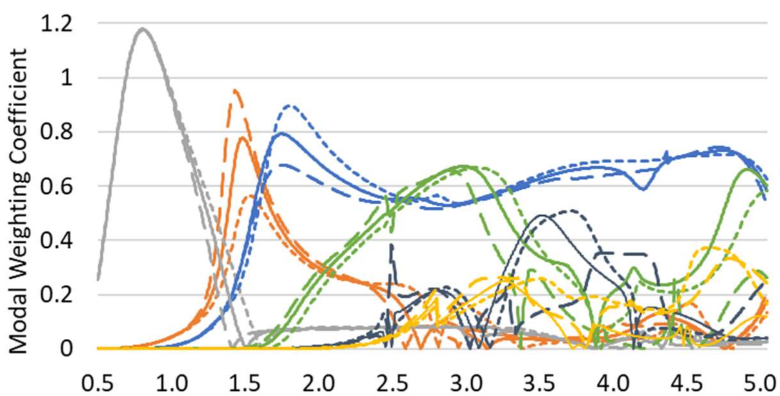

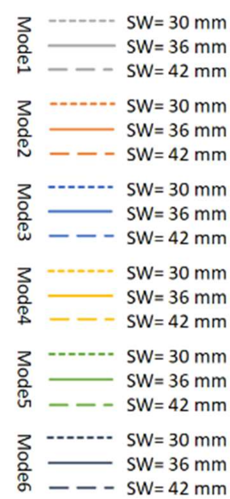

(f) Sweep U-slot width (Sw)

The U-slot dimensions were investigated by sweeping in 3 mm steps. The |WMC| was monitored in Figure 4.9(d, e, and f). As the long slot arm (SL1) increased, a significant shift in Mode 2 to a lower frequency and higher |WMC| value was noticed. Furthermore, there was minimal effect on Mode 3 and other cellular modes. As the U-slot short arm (SL2) increased, Mode 3 shifted to a lower frequency while having much less effect on Mode 2, thus changing the length difference between the two U-slot branches helps fine-tune the phase difference between the modes for a better axial ratio. Finally, the width of the U slot (Sw) was analyzed, and as (Sw) increased, both Mode 2 and Mode 3 shifted in frequency. However, it also balanced the amplitude between those two modes, helping to tune the circular polarization.

4.2.4 Antenna matching and Return Loss

After tuning the structure to achieve the best radiation characteristics and optimizing the radiation pattern performance using characteristic mode analysis, the return loss and the 50-ohm impedance matching were inadequate at the LTE band B71 range 617-700 MHz and GNSS band frequency range. This would cause a reduction in the overall efficiency due to insertion losses. So, to reduce the power reflection, a matching circuit at the antenna port was used, as shown in Figure 4.10(a). The return loss was improved to below 6 dB for all cellular and GNSS bands, as shown in Figure 4.10(b).

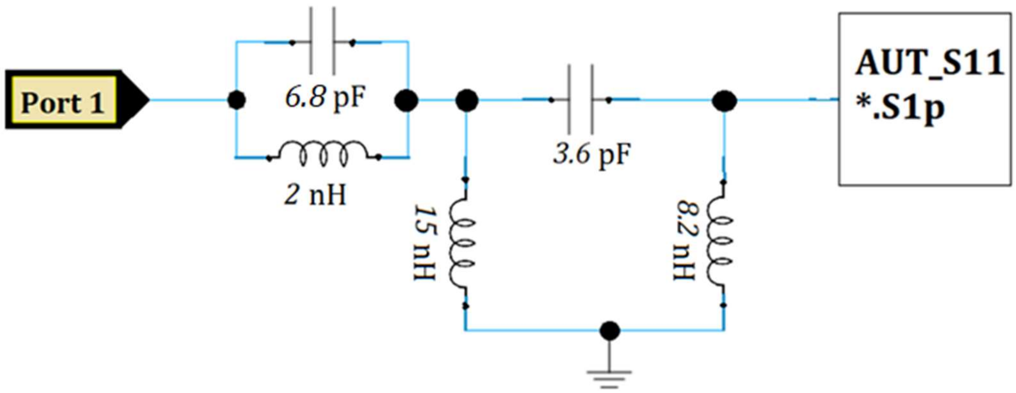

(a)

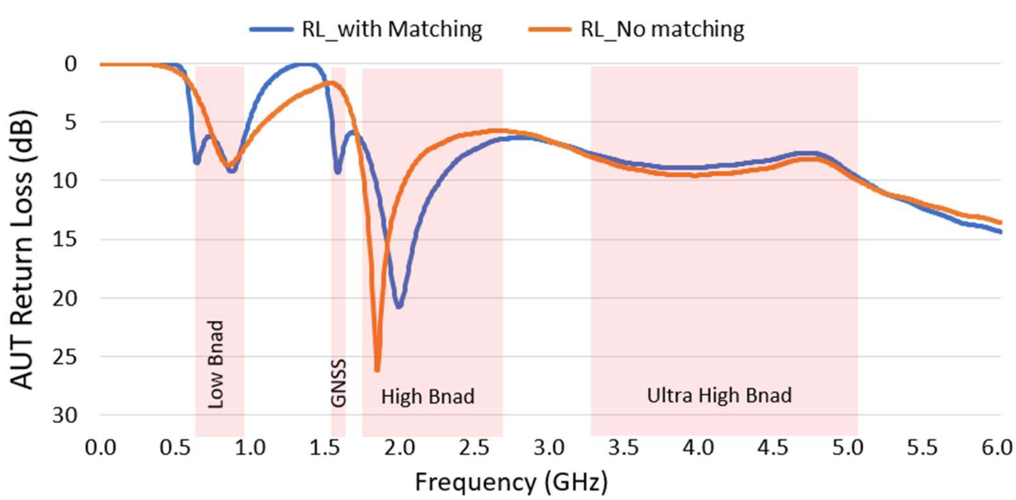

(b)

Figure 4.10: Return loss improvement a) matching circuit b) Return loss improvement using a matching circuit.

4.3 Results

The proposed antenna prototype was fabricated and evaluated on a 1-meter round ground plane. In a similar setup, the antenna model was simulated using an electromagnetic full-wave tool, and the results and performance metrics are discussed in the following sections.

4.3.1 Fabrication and measurement setup

The antenna was built using a 0.3 mm brass sheet and 1 mm PCB FR4 for the feeding structure. The PCB top was soldered directly along the sheet metal center line, and then the antenna feed and the shorting metal sheet were soldered directly to the main PCB with the populated matching circuit. Finally, the structure was mounted on a 1-meter circular ground plane, as shown in Figure 4.11(a); measurement was collected in an anechoic antenna chamber. A similar simulation model was used for evaluation as shown in Figure 4.11(b).

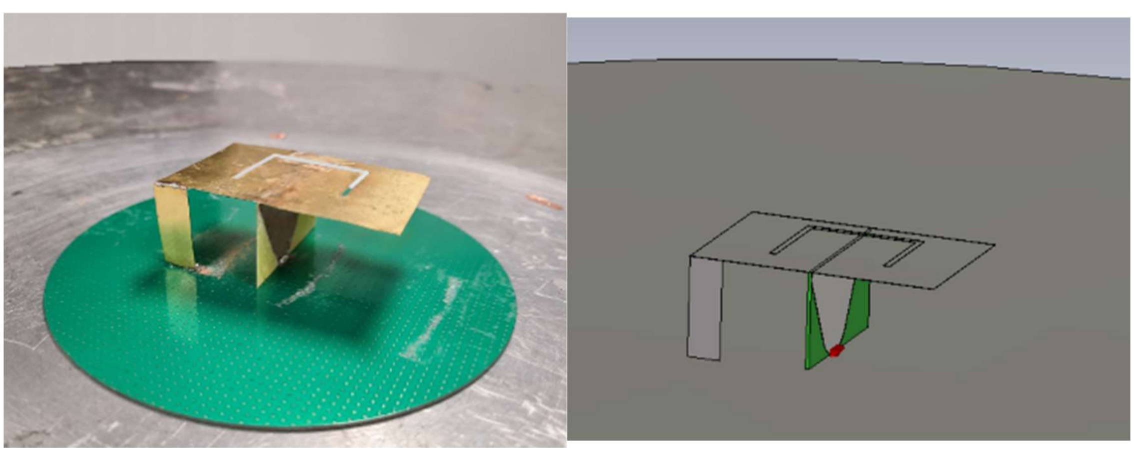

(a) (b)

Figure 4.11:Antenna evaluation model a) fabricated prototype. b) simulation model

Measurement and simulation data were collected for the full sphere with a resolution of 5 degrees in azimuth and elevation for the following frequency resolutions per band: 'low band' 0.617– 0.96 GHz in 20 MHz frequency steps, GNSS L1 band 1.559-1.606 GHz in frequency steps of 5 MHz, 'high band' 1.71–2.69 GHz in a 50 MHz frequency steps, and 'ultra-high band' 3.30–5.00 GHz with a frequency step of 75 MHz.

4.3.2 VSWR

The S-parameters of the simulation results, including the matching circuit discussed in Figure 4.10(a), were collected. The prototyped antenna was also measured with a similar setup at the feeding point and the same matching circuit using high-quality factor components. The results for both simulated and measured are plotted in Figure-4.12, and the VSWR was below 3:1 over the desired operating frequency range.

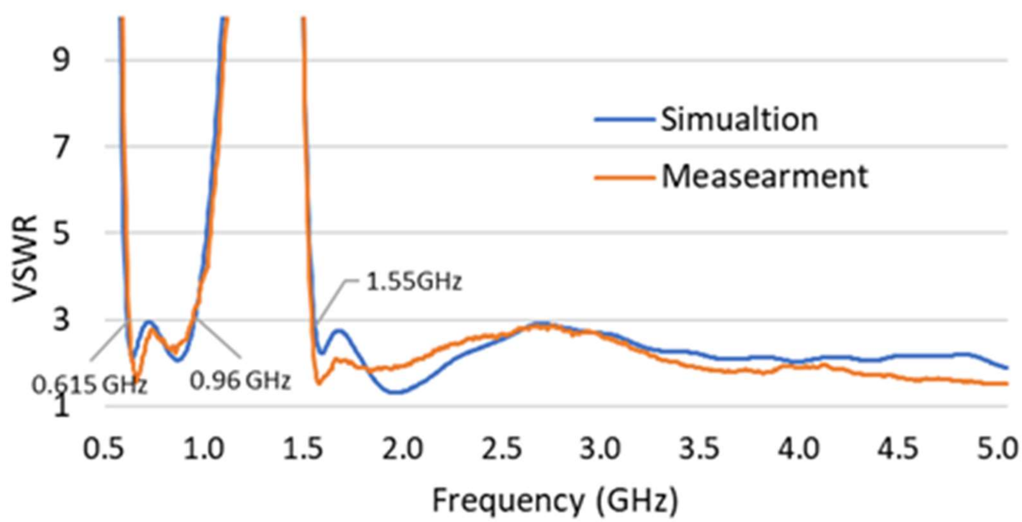

Figure 4.12: Antenna VSWR for both measurement and simulation

4.3.3 Radiation efficiency

The antenna's total efficiency was collected from simulation software and measurement data, as shown in Figure 4.13. In both cases, the efficiency values include the matching circuit and mismatch loss. Measurement data had a lower average efficiency of around 5-10 % compared to the simulation data. This was probably due to a non-ideal matching circuit and the actual PCB material loss on the prototype. Overall, the trends matched. The average measurement efficiency for GNSS band was 65%, and the efficiency for cellular 'low band', 'high band', and 'ultra-high band' were 62%, 80%, and 79%, respectively.

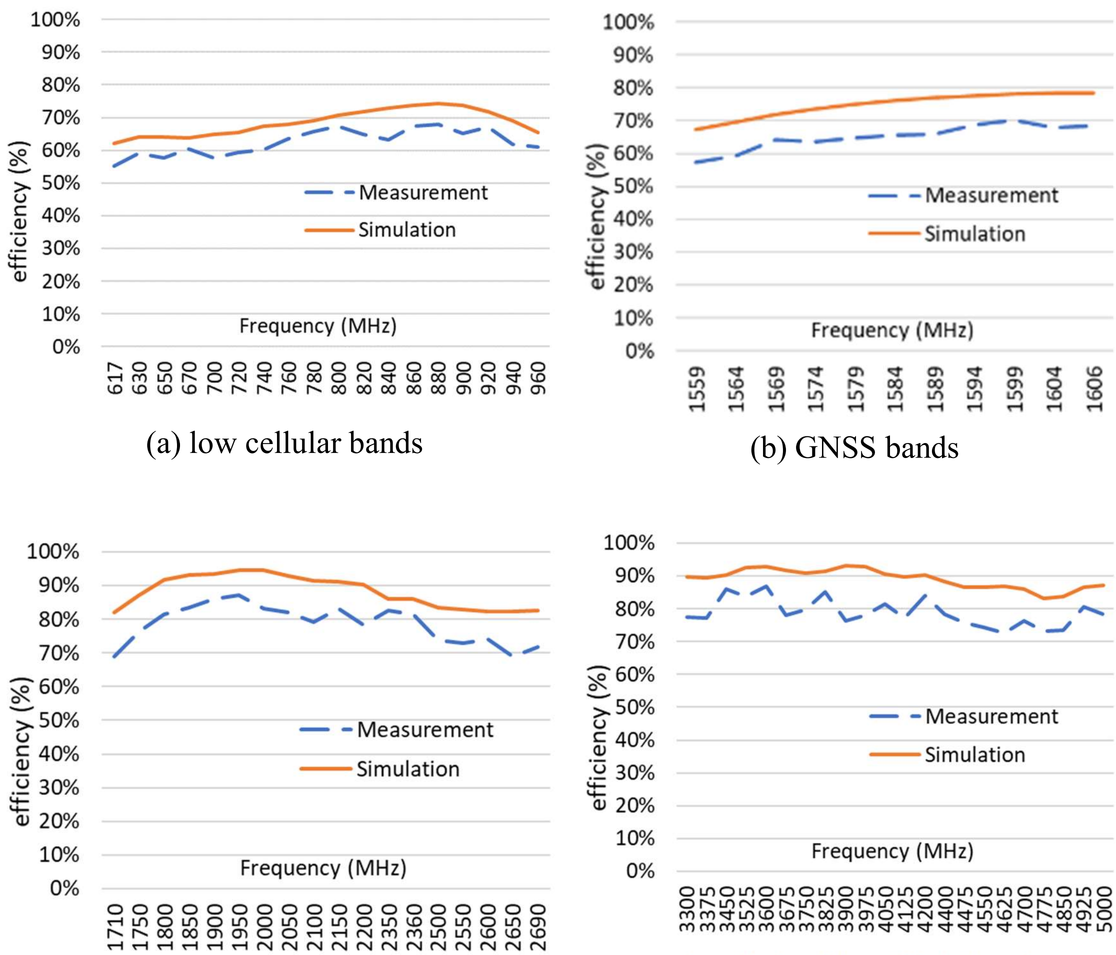

(a) low cellular bands

(b) GNSS bands

(c) cellular High Bands

(d) cellular Ultra-High Bands

Figure 4.13: Total Antenna efficiency at different frequency ranges.

4.3.4 GNSS Radiation Performance

The radiation pattern performance was evaluated by simulation and measurement at GNSS L1 frequencies, as shown in Figure 4.14 for the tow perpendicular elevation cuts ZX and ZY plans. The main beam for simulation and measurment agrees well and meets the required directionality toward the zenith. However, a skew from one side can be notice and it is most likely due to the shorting metal or asymmetrical U-slot which lead to asymmetrical radiation. The RHCP gain at the zenith measures between 5-5.8 dBc, while the simulation was 6.9-7.5 dBc. The left-hand circular polarization (LHCP) gain is also shown in the same plot. The cross-polarization (XPR) at boresight shows 20-25 dB, indicating a good polarization priority.

The antenna's performance can be evaluated statistically as a linear average gain (LAG) for the GNSS frequencies 1559-1606 MHz at each elevation for the upper hemisphere, along with the average axial ratio for each elevations, as shown in Figure 4.15. The gain has an average peak of 7.2 dBc and 5.4 dBc, while the average axial ratio of 1.1 dB and 1.7 dB at boresight for simulation and measurement, respectively. The half-power beamwidth and the 3.0 dB axial ratio beamwidth were aligned with values of 70 degrees. The average axial ratio starts to degrade significantly for elevations below theta 45 degrees as the antenna radiation loses its horizontal (phi) component field as it gets closer and tangential to the ground plane in the test setup. thus lower elevation vertical polarization dominates and axial ratio increase.

(XZ-plane)	(XY plane)

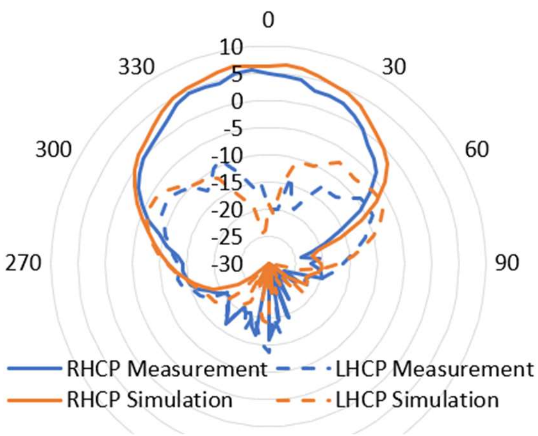

(a) plane cut (φ=0), 1559 MHz

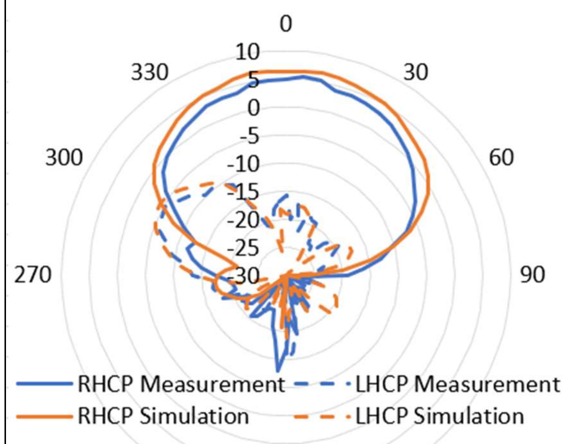

(b) plane cut (φ=90) , 1559 MHz

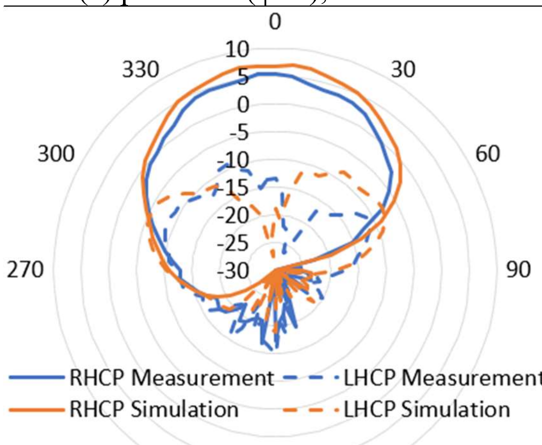

(c) plane cut (φ=0) ,1574 MHz

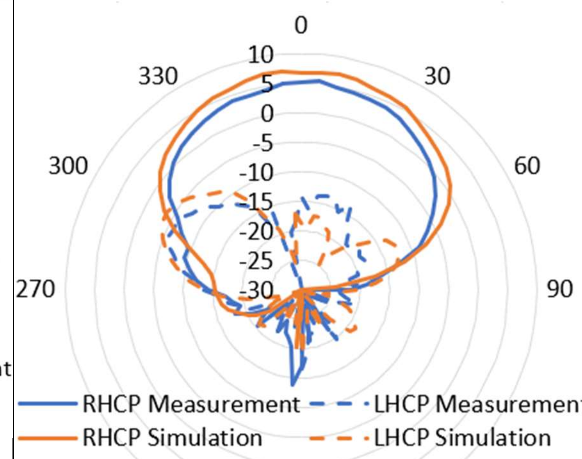

(d) plane cut (φ=90) , 1574 MHz

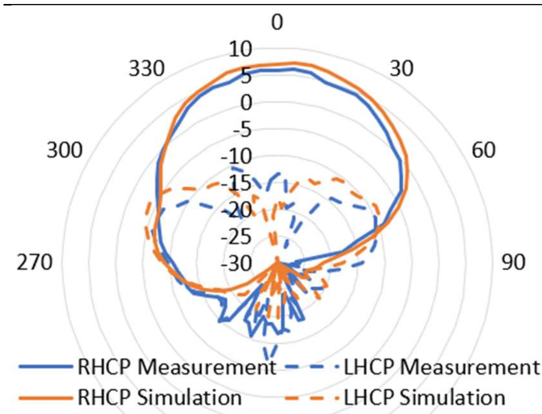

(e) plane cut (φ=0) ,1604 MHz

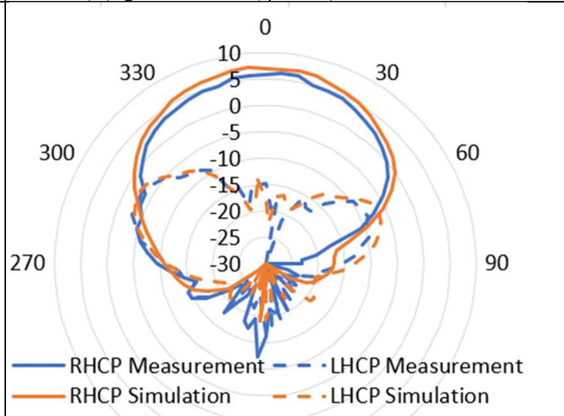

(f) plane cut (φ=90) , 1604 MHz

Figure 4.14: GNSS 2D Radiation pattern per band. ***a,b)*** Beidue 1559MHz. ***c,d)*** GPS at 1574 MHz. ***e,f)*** GLONASS at 1604 MHz.

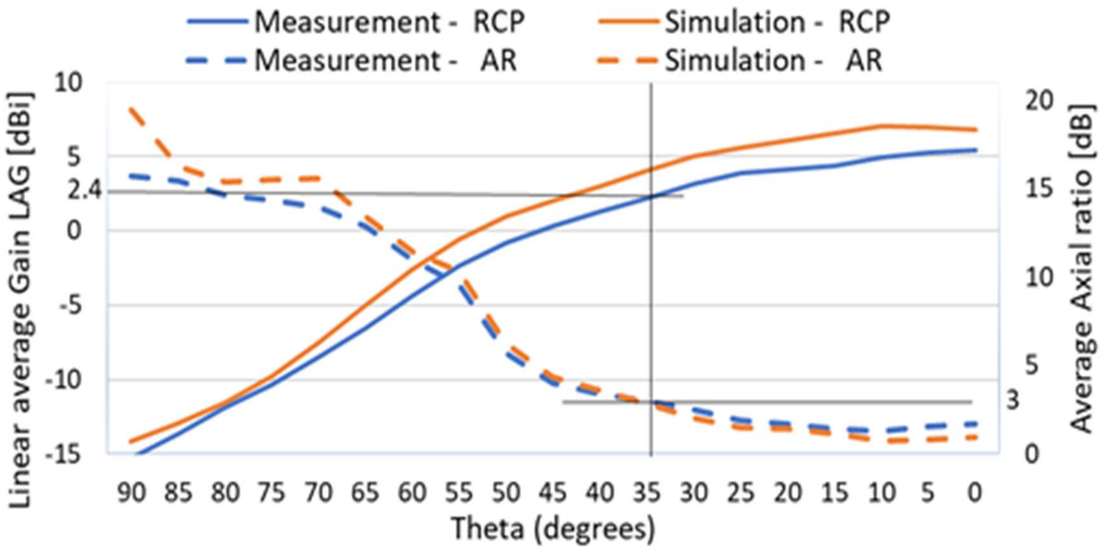

Figure 4.15: GNSS band Average Linear average gain (LAG) and average axial ratio (AR)

4.3.5 Cellular Radiation performance

The radiation pattern for the AUT cellular bands is shown in Figure 4.16, it indicates the elevation cut at Phi =0 and azimuth cut at theta = 75 degrees and at the mid-frequency range for the low, high, and ultra-high bands. Again, measurement and simulated data show a good match. Since the antenna was simulated/measured on a finite 1-meter ground plane, peak gain tends to move to lower elevations, and the pattern becomes more focused as the frequency increases because the ground plane has a relatively larger electrical size. The maximum gain measured was 3.7 dBi, 5.2 dBi, and 7.4 dBi for the 0.78 GHz, 2.20 GHz, and 4.20 GHz, respectively.

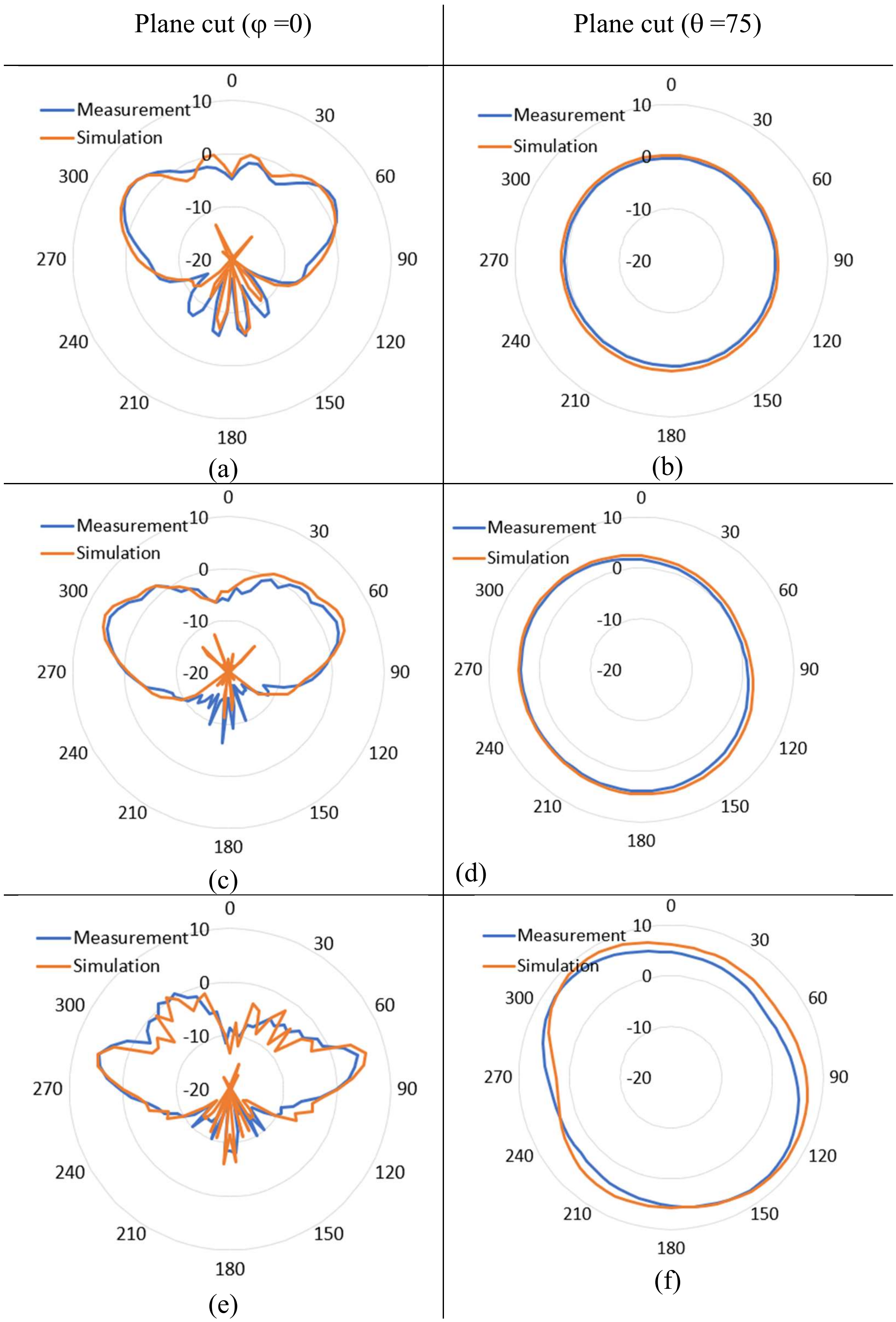

Figure 4.16: Cellular total gain 2D radiation pattern for simulation and measurement at **a,b)** Mid of low Band 0.78GHz. **c,d)** Mid of high band 2.20 GHz. **e,f)** Mid of ultra-high Band 4.20 GHz.

It is common to evaluate the cellular automobile antenna using the statistical metric linear average gain (LAG) to show the performance over the frequency range for the interested elevation zone from theta 60-90 degrees, as shown in Figure 4.17. The LAG has a consistent and flat gain across the frequency band for the measurement and simulation results. The 'low band' LAG is between -1.3 dBi and 0.5 dBi. The cellular 'high band's LAG is between 0.8 dBi and 2.2 dBi. Finally, the average LAG for the 'ultra-high band' was between 1.4 dBi and 2.6 dBi.

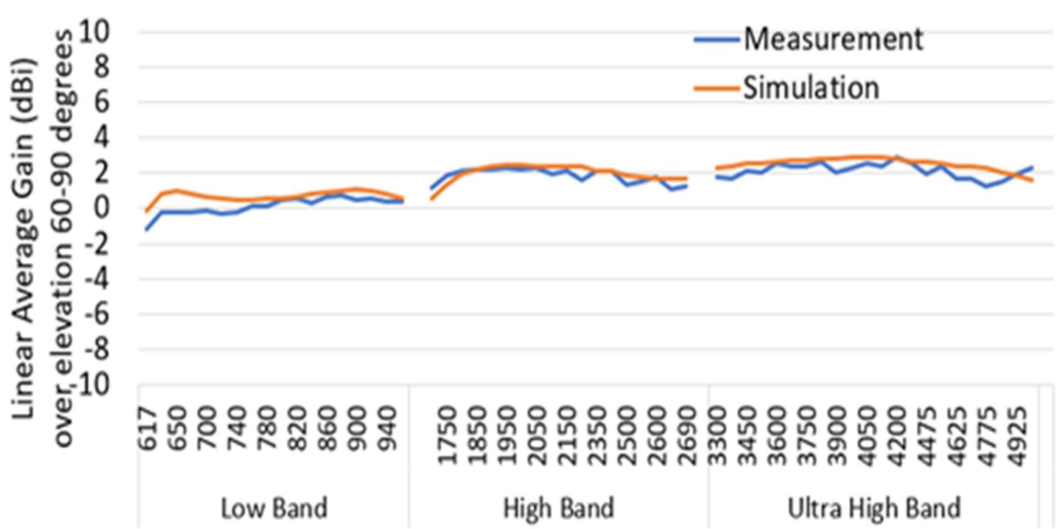

Figure 4.17: Cellular Linear Average Gain for measurement and simulation

CHAPTER FIVE

CONCLUSIONS

The characteristic mode theory is a powerful tool that decomposes the total current on a conductive structure into the orthogonal current set despite the excitation condition; each current mode is associated with the orthogonal radiation mode. This allows each mode to be manipulated separately, the TCM is widely used for different aspects of antenna design, such as increasing impedance bandwidth, enhancing the isolation between antenna elements in a MIMO system, and miniaturization by choosing excitation metallic parts in hand-held or electrically small structure devices. It is also beneficial for radiation pattern steering and enhancement.

In this study, we successfully utilize CMA to combine basic antenna geometries to superpose their modes and synthesize the required radiation pattern and polarization at the intended frequency range. By understanding the characteristic modes associated with specific geometry, the combined structure can also analyzed and returned, ensuring the preservation of intrinsic geometry radiation modes and performance.

This study focuses on automotive antenna applications, mainly using CMA to solve challenges associated with the new 5G cellular antenna element design, including covering the new bands in the frequency range 617GHz-5GHz. Second, this study focuses on optimizing antenna radiation pattern for automotive application and antenna performance by assuring only the modes with desired performance is operating in the bands. Third, the study shows the possible solution to help multi-function packaging, especially for 5G cellular and GNSS function, either by making cellular antenna providing high rejection at the GNSS band or by consolidating GNSS together in the same Cellular Antenna structure.

The first part, chapter 3, presents an antenna design for the newly defined 5G sub-6GHz bands for vehicle rooftop applications. The design method utilizes the CMA to combine two wide band monopoles and avoid higher order modes, which provide an optimal and consistent radiation pattern across the cellular frequency ranges: low band 0.617-0.96 GHz, high band 1.7 - 2.7 GHz, and ultra-high band 3.3 - 5 GHz. The antenna was fabricated on a two-layer FR4 PCB. The Total size was 58×30×1 mm3. The performance was evaluated by a prototype measurement and simulation data on a 1-meter diameter ground plane. The VSWR was below 2.7:1, the average antenna efficiency was 80%, and the LAG for theta between (60-90 degrees) was 0.5 dBi for frequencies below 1 GHz and 2.5 dBi for frequency bands higher than 1 GHz up to 5 GHz. The gain standard deviation for 360-degree azimuth at theta angles close to the horizon 60 to 90 degrees was below 1 dB.

The second part, chapter 4 illustrates a novel multi-functional antenna that exhibits radiation characteristics that simultaneously fulfill the requirements for both cellular and GNSS applications. The antenna's radiation pattern demonstrates omnidirectionality and linear polarization for the cellular bands within the 617-5000 MHz frequency range. Conversely, the radiation pattern is hemispherical with right-hand circular polarization for the GNSS L1 frequency range of 1559-1606 MHz. The CMA was a pivotal method to tune the radiation modes required for each function. The physical dimensions of the antenna were 75×50×30 mm^3. It was fabricated and evaluated on a 1-meter circular ground plane—the measurement results aligned closely with the simulation data, indicating reliable performance. The Voltage Standing Wave Ratio (VSWR) remains below 3:1 across the bands, and the overall measured efficiency ranges from 62% to 80%. Regarding the GNSS measurements, the antenna exhibits a maximum gain of 5.4 dBc for right-hand circular polarization at boresight, with an axial ratio of 1.7 dB. In comparison, the cellular bands' omnidirectional radiation pattern demonstrates a linear average gain of 0.3 dBi, 1.8 dBi, and 2 dBi for the low, high, and ultra-high bands, respectively.

This design approach, utilizing characteristic mode analysis, has effectively addressed radiation pattern issues and to provide an optimal performance over a wide frequency range. Similarly, it can be employed to expand antenna functionality to encompass additional functions with similar radiation pattern and polarization properties, such as Wi-Fi, V2X, BLE, and more. Furthermore, it has the potential to extend the operation of two functions with distinct radiation patterns and polarization, as seen in GNSS and cellular technologies. This approach opens opportunities for consolidating multiple antennas, promoting space and material reuse, and simplifying the production of automotive antenna products.

REFERENCES:

[1] Abdulsalam, Fathi M A. "Antenna Design Using Optimization Techniques over Various Computational Electromagnetics: Antenna Design Structures Using Genetic Algorithm, Particle Swarm and Firefly Algorithms Optimization Methods Applied on Several Electromagnetics Numerical Solutions and Applications Including Antenna Measurements and Comparisons." ProQuest Dissertations Publishing, 2018.

[2] Constantine A. Balanis. Antenna Theory: Analysis and Design, 3rd Ed. Hoboken, New Jersey: John Wiley & Sons, Inc, 2005.

[3] Antenna Standards Committee "IEEE Standard Definitions of Terms for Antennas" IEEE Standards Board, March 18, 1993

[4] Abdelkader, G.; Elgazzar, K.; Khamis, A. Connected Vehicles: Technology Review, State of the Art, Challenges and Oppor- 408 tunities. Sensors 2021, 21, 7712.]

[5] S. Kumar, A. S. Dixit, R. R. Malekar, H. D. Raut and L. K. Shevada, "Fifth Generation Antennas: A Comprehensive Review of Design and Performance Enhancement Techniques," in IEEE Access, vol. 8, pp. 163568-163593, 2020

[6] V. Rumsey, "Frequency independent antennas," in Proc. IRE Int. Conv. Rec., vol. 5. 1957, pp. 114–118

[7] G. Artner, W. Kotterman, G. Del Galdo and M. A. Hein, "Automotive Antenna Roof for Cooperative Connected Driving," in IEEE Access, vol. 7, pp. 20083-20090, 2019

[8] Seong-Youp Suh, W. L. Stutzman, and W. A. Davis, "A new ultrawideband printed monopole antenna: the planar inverted cone antenna (PICA)," in IEEE Transactions on Antennas and Propagation, vol. 52, no. 5, pp. 1361-1364, May 2004,

[9] B. Sanz-Izquierdo and R. Leelaratne, "Evaluation of wideband LTE antenna configurations for vehicle applications," 2013 Loughborough Antennas & Propagation Conference (LAPC), 2013, pp. 383-387.

[10] A. Michel, P. Nepa, M. Gallo, I. Moro, A. P. Filisan and D. Zamberlan, "Printed Wideband Antenna for LTE-Band Automotive Applications," in IEEE Antennas and Wireless Propagation Letters, vol. 16, pp. 1245-1248, 2017.

[11] Cheng Y, Lu J, Wang C. Design of a Multiple Band Vehicle-Mounted Antenna. International Journal of Antennas & Propagation. December 2019:1-12.

[12] F. Melli et al., "Low Profile Wideband 3D Antenna for Roof-Top LTE Vehicular Applications," 2019 IEEE-APS Topical Conference on Antennas and Propagation in Wireless Communications (APWC), 2019, pp. 157-159.

[13] I. Goncharova and S. Lindenmeier, "A high-efficient 3-D Nefer-antenna for LTE communication on a car," The 8th European Conference on Antennas and Propagation (EuCAP 2014), 2014, pp. 3273-3277.

[14] D. Preradovic and D. N. Aloi, "Ultra Wide Planar Monopole Antenna for LTE Application in Automobile," 2018 IEEE International Conference on Electro/Information Technology (EIT), 2018, pp

[15] D. V. Navarro-Méndez et al., "Compact Wideband Vivaldi Monopole for LTE Mobile Communications," in IEEE Antennas and Wireless Propagation Letters, vol. 14, pp. 1068-1071, 2015.

[16] Luo, Wei; Chen, Wuquan; Feng, Yulu; Yang, Yuqi." A novel automobile antenna for vehicles communication of IoT systems in 5G network" EURASIP Journal on Wireless Communications & Networking. 10/29/2020, Vol. 2020.

[17] M. O. Khalifa, A. M. Yacoub, and D. N. Aloi, "A Multiwideband Compact Antenna Design for Vehicular Sub-6 GHz 5G Wireless Systems," in IEEE Transactions on Antennas and Propagation, vol. 69, no. 12, pp. 8136-8142, Dec. 2021.

[18] Ibrahim, Ahmad S., Ahmad M. Yacoub, and Daniel N. Aloi. "A 3-Dimensional Multi-band Antenna for Vehicular 5G Sub-6 GHz/GNSS/V2X Applications." International journal of antennas and propagation 2022 (2022).

[19] Abdul-Rahman, E.; Aloi, D.N. Design of a 5G Sub-6 GHz Vehicular Cellular Antenna Element with Consistent Radiation Pattern Using Characteristic Mode Analysis. Sensors 2022, 22, 8862.Web

[20] Liu, Ying, et al. "An Integrated Shark-Fin Antenna for MIMO-LTE, FM, and GPS Applications." IEEE antennas and wireless propagation letters 18.8 (2019): 1666–1670.

[21] Ghafari, Elias, et al. "A Vehicular Rooftop, Shark-Fin, Multi-band Antenna for the GPS/LTE/cellular/DSRC Systems." 2014 IEEE-APS Topical Conference on Antennas and Propagation in Wireless Communications (APWC). IEEE, 2014. 237–240.

[22] Ai, Zhuang et al. "Design of A Combination Antenna for Automotive Mobile Communication Systems." 2019 International Symposium on Antennas and Propagation (ISAP). Antenna Branch of Chinese Institute of Electronics, 2019. 1–3.

[23] Low-Profile Automotive Antenna Systems for MIMO 5G and L1/L5 GNSS Communications." 2022 16th European Conference on Antennas and Propagation (EuCAP). European Association for Antennas and Propagation, 2022. 1–4.

[24] Wang, Yaning, Ying Li, and Qi Zhu. "A Compact Tri-Band Antenna for GPS and GSM Applications." 2017 Sixth Asia-Pacific Conference on Antennas and Propagation (APCAP). IEEE, 2017. 1–3.

[25] J. D. Doherty, I. Shoaib, X. Chen, and C. Parini, "Study and design of an integrated GPS and cellular antenna," 2013 Loughborough Antennas & Propagation Conference (LAPC), 2013, pp. 587-590.

[26] Abdul-Rahman, E., Aloi, D.N.: Design a multi-function global navigation satellite system and 5G cellular antenna structure for automotive applications using characteristic mode analysis. IET Microwave and Antennas Propagation. 17(11), 863–871 (2023).

[27] Characteristic modes: Theory and applications in antenna engineering (2015). Beaverton: Ringgold Inc. Retrieved from "https://www.proquest.com-/other-sources/characteristic-modes-theory-applicationsantenna/docview-/1701631274/se-2

[28] R. J. Garbacz, "Modal expansions for resonance scattering phenomena," Proc. IEEE, vol. 53, no. 8, pp. 856–864, Aug. 1965.

[29] Garbacz, R, and R Turpin. "A Generalized Expansion for Radiated and Scattered Fields." IEEE Transactions on antennas and propagation 19.3 (1971): 348–358. Web.

[30] Harrington, Roger F, and Joseph R Mautz. Theory and Computation of Characteristic Modes for Conducting Bodies. N.p., 1970. Print.

[31] R. Harrington and J. Mautz, "Computation of characteristic modes for conducting bodies," in IEEE Transactions on Antenna and Propagation, vol. 19, no. 5, pp. 629-639, September 1971.

[32] Y. Chang and R. F. Harrington, "A surface formulation for characteristic modes of material bodies," IEEE Trans. Antennas Propag., vol. AP-25, no. 6, pp. 789–795,Nov. 1977.

[33] R. F. Harrington, J. R. Mautz, and Y. Chang, "Characteristic modes for dielectric and magnetic bodies," IEEE Trans. Antennas Propag., vol. AP-20, no. 2, pp. 194–198, Mar. 1972.

[34] E. H. Newman, "Small antenna location synthesis using characteristic modes," IEEE Trans. Antennas Propag., vol. AP-25, no. 4, pp. 530–795,1977.

[35] K. P. Murray and B. A. Austin, "Synthesis of Vehicular NVIS Radiation Patterns Using the Method of Characteristic Modes," Microwave Antennas and Propagation, IEEE Proceedings, Volume 141, Issue 3, pp. 151-154, June 1994

[36] Y. Chen and C. Wang, "HF band shipboard antenna design using characteristic modes," IEEE Trans. Antennas Propag., vol. 63, no. 3, pp. 1004–1013, Mar. 2015, doi: 10.1109/TAP.2015.2391288.

[37] Y. Chen and C. Wang, "Electrically small UAV antenna design using characteristic modes," IEEE Trans. Antennas Propag., vol. 62, no. 2, pp. 535–545, Feb. 2014, doi: 10.1109/TAP.2013.2289999.

[38] Pandiya, Abhishek, and Yogesh Kumar Choukiker. "Characteristic Mode Analysis of Mobile Hand Held Device for MIMO Applications." 2017 IEEE International Conference on Electrical, Instrumentation and Communication Engineering (ICEICE). IEEE, 2017.

[39] Babu, K. Vasu, et al. "Broadband Sub-6 GHz Flower-shaped MIMO Antenna with High Isolation Using Theory of Characteristic Mode Analysis (TCMA) for 5G NR Bands and WLAN Applications." International journal of communication systems (2023).

[40] Futter, P. W., and U. Jakobus. "LTE Antenna Design for Tablet Computers Using Characteristic Mode Analysis." 2019 13th European Conference on Antennas and Propagation (EuCAP). European Association on Antennas and Propagation, 2019.
[41] Luomaniemi, Rasmus, et al. "Designing Hand-Immune Handset Antennas With Adaptive Excitation and Characteristic Modes." IEEE transactions on antennas and propagation 69.7 (2021)
[42] Hui Li, Zachary Thomas Miers, and Buon Kiong Lau. "Design of Orthogonal MIMO Handset Antennas Based on Characteristic Mode Manipulation at Frequency Bands Below 1 GHz." IEEE Transactions on antennas and propagation 62.5 (2014).
[43] He, Danting, Yantao Yu, and Shenshen Mao. "Characteristic Mode Analysis of a MIMO Antenna with DGS." 2021 IEEE International Symposium on Antennas and Propagation and USNC-URSI Radio Science Meeting (APS/URSI). IEEE, 2021. 1143–1144.
[44] Ethier, Jonathan, Eric Lanoue, and Derek McNamara. "MIMO Handheld Antenna Design Approach Using Characteristic Mode Concepts." Microwave and optical technology letters 50.7 (2008): 1724–1727.
[45] Yang, Xu, Ying Liu, and Shu-Xi Gong. "Design of a Wideband Omnidirectional Antenna With Characteristic Mode Analysis." IEEE antennas and wireless propagation letters 17.6 (2018).
[46] Sheng, Huiwen, and Zhi Ning Chen. "Radiation Pattern Improvement of Cross-Band Dipoles Using Inductive-Loading Mode-Suppression Method." IEEE Transactions on antennas and propagation 67.5 (2019): 3467–3471. Web.

[47] Sheng, Huiwen, and Zhi Ning Chen. "Improving Radiation Pattern Roundness of a Monopole Antenna Placed Off-Center Above a Circular Ground Plane Using Characteristic Mode Analysis." IEEE Transactions on antennas and propagation 69.2 (2021): 1135–1139. Web.

[48] Lin, Feng Han, and Zhi Ning Chen. "A Method of Suppressing Higher Order Modes for Improving Radiation Performance of Metasurface Multiport Antennas Using Characteristic Mode Analysis." IEEE Transactions on antennas and propagation 66.4 (2018): 1894–1902. Web.

[49] Wen, Dingliang, et al. "Design of a Wideband Antenna With Stable Omnidirectional Radiation Pattern Using the Theory of Characteristic Modes." IEEE Transactions on antennas and propagation 65.5 (2017): 2671–2676. Web.

[50] Antonino-Daviu, Eva, et al. "Modal Analysis and Design of Band-Notched UWB Planar Monopole Antennas." IEEE transactions on antennas and propagation 58.5 (2010): 1457–1467

[51] Dicandia, Francesco Alessio, Simone Genovesi, and Agostino Monorchio. "Efficient Excitation of Characteristic Modes for Radiation Pattern Control by Using a Novel Balanced Inductive Coupling Element." IEEE Transactions on antennas and propagation 66.3 (2018).

[52] Dicandia, Francesco Alessio, Simone Genovesi, and Agostino Monorchio. "Null-Steering Antenna Design Using Phase-Shifted Characteristic Modes." IEEE Transactions on antennas and propagation 64.7 (2016): 2698–2706.

[53] Dicandia, Francesco Alessio, Simone Genovesi, and Agostino Monorchio. "Advantageous Exploitation of Characteristic Modes Analysis for the Design of 3-D Null-Scanning Antennas." IEEE Transactions on antennas and propagation 65.8 (2017).

[55] Agrawall, N.P, G Kumar, and K.P Ray. "Wide-Band Planar Monopole Antennas." IEEE Transactions on antennas and propagation 46.2 (1998): 294–295. Web.

[56] CST Microwave Studio, 2022. http:// www.cst.com

[57] Lau, B. K., Capek, M., Hassan, "A. M.: Characteristic Modes - Progress, Overview, and Emerging Topics." IEEE Antennas and Propagation Magazine, vol. 64, no. 2, 2022.

[58] Elias, Bashar Bahaa Qas, et al. "A Review of Antenna Analysis Using Characteristic Modes." IEEE Access 9 (2021): 98833–98862. Web.

[59] Mahrukh Khan, and Deb Chatterjee. "Characteristic Mode Analysis of a Class of Empirical Design Techniques for Probe-Fed, U-Slot Microstrip Patch Antennas." IEEE Transactions on antennas and propagation 64.7 (2016): 2758–2770.

[60] Borchardt, John J, and Tyler C Lapointe. "U-Slot Patch Antenna Principle and Design Methodology Using Characteristic Mode Analysis and Coupled Mode Theory." IEEE Access 7 (2019): 109375–109385.

[61] TONG, Kin-Fai, and Ting-Pong WONG. "Circularly Polarized U-Slot Antenna." IEEE Transactions on antennas and propagation 55.8 (2007): 2382–2385.

[62] Yikai Chen, and Chao-Fu Wang. "Characteristic-Mode-Based Improvement of Circularly Polarized U-Slot and E-Shaped Patch Antennas." IEEE antennas and wireless propagation letters 11 (2012): 1474–1477.

[63] Zeng, Jianping, et al. "Single-Fed Triple-Mode Wideband Circularly Polarized Microstrip Antennas Using Characteristic Mode Analysis." IEEE Transactions on antennas and propagation 70.2 (2022): 846–855.

[64] Anob, P.V, K.P Ray, and G Kumar. “Wideband Orthogonal Square Monopole Antennas with Semi-Circular Base.” IEEE Antennas and Propagation Society International Symposium. 2001 Digest. Held in Conjunction with the USNC/URSI National Radio Science Meeting (Cat. No.01CH37229). Vol. 3. IEEE, 2001. 294–297 vol.3.